Iodine Waste Form Corrosion: PNNL Summary Testing Report

Nuclear Technology Research and Development

Prepared for
U.S. Department of Energy
Material Recovery and Waste Form Development Campaign

A.R. Lawter, N.M. Avalos, J.F. Bonnett, N. Canfield, M.E. Bowden, L.M. Seymour, S.A. Saslow, A.L. Bourchy and R.M. Asmussen
Pacific Northwest National Laboratory

July 31, 2020
PNNL-30127

DISCLAIMER

This information was prepared as an account of work sponsored by an agency of the U.S. Government. Neither the U.S. Government nor any agency thereof, nor any of their employees, makes any warranty, expressed or implied, or assumes any legal liability or responsibility for the accuracy, completeness, or usefulness, of any information, apparatus, product, or process disclosed, or represents that its use would not infringe privately owned rights. References herein to any specific commercial product, process, or service by trade name, trade mark, manufacturer, or otherwise, does not necessarily constitute or imply its endorsement, recommendation, or favoring by the U.S. Government or any agency thereof. The views and opinions of authors expressed herein do not necessarily state or reflect those of the U.S. Government or any agency thereof.

SUMMARY

A test method to correlate the laboratory corrosion behavior of iodine-containing waste forms (IWFs) to a conceptual long-term corrosion model is required. Several candidate methods have been evaluated previously, and each method presents unique challenges and limitations. Dynamic leach tests have emerged as the preferred candidate test method to evaluate IWFs and parameterize an eventual long-term corrosion model. This report was prepared in support of this effort to define the test suite to evaluate the corrosion of IWFs, with the goal of defining and parameterizing a conceptual long-term corrosion model. A review was presented highlighting the high degree of variability between the IWF corrosion data that is available in the literature and the need for a standardized test suite. The targeted test suite is composed of a single interval screening test, a dynamic leach test, and post-test solid characterization of the monolithic IWF samples. The data presented serves two purposes: to expand the range of IWFs evaluated with the test suite to assess method variability and to further understand the corrosion of IWFs to best inform conceptual long-term corrosion model development. A series of IWF types were included in the testing, including hot isostatically pressed Ag-mordenite, silver functionalized silica-based aerogels, iodosodalites (hot isostatic pressing, sintered, glass bonded ceramic), iodoapatite, tellurite glass and glass composite materials.

CONTENTS

SUMMARY iii

ACRONYMS ix

1. INTRODUCTION 1
   1.1 Summary of Prior IWF Test Efforts 1
   1.2 Review of IWF Literature Data 4

2. Materials and Methods 10
   2.1 Sample Preparation 10
   2.2 Test Suite 13
      2.2.1 Screening and Dynamic Leach Test 13
   2.3 Solid Phase Characterization 14
      2.3.1 Spectroscopy 14
      2.3.2 Micro-X-ray Diffraction (µXRD) 14
      2.3.3 Optical Profilometry 14

3. RESULTS AND DISCUSSION 15
   3.1 Sample Characterization 15
      3.1.1 Optical Imaging 15
      3.1.2 Scanning Electron Microscopy SEM 15
      3.1.3 µXRD of HIP Ag-Mordenite Large Form 16
   3.2 Corrosion Testing 18
      3.2.1 Iodine Waste Form Screening Test 18
      3.2.2 Dynamic Leach Testing 21
   3.3 Conceptual Model Variable Testing 30
      3.3.1 Common Ion Effect 30
      3.3.2 Temperature 32
      3.3.3 Comparison of Sample Surface Area : Solution (SA/V) Ratio 33
   3.4 Microstructure Analysis 34
      3.4.1 SEM of “After” Samples 34
      3.4.2 Optical Profilometry 38

4. SUMMARY AND CONCLUSIONS 40

5. References 42

Appendix A Sample Characterization 46

Appendix B Aqueous Analysis- Raw data 61

FIGURES

Figure 3-1. Photographs of the samples evaluated in this study. 15

Figure 3-2. SEM micrographs of the various sample types used in this study prior to corrosion testing. All images were collected at 250×; the scale bar in the top left corner applies to all of the SEM micrographs. 16

Figure 3-3. µXRD spectra for HIP18-3 (100% iodine capacity) 17

Figure 3-4. Pre- and post-leach test µXRD spectra for HIP 18-3, represented by 2019 and 2020, respectively. 17

Figure 3-5. µXRD pattern for HIP18-2 (30% iodine capacity). 18

Figure 3-6. Pre- and post- leach test µXRD patterns for HIP 18-2, represented by 2019 and 2020, respectively. 18

Figure 3-7. The normalized silicon dissolution rate (left) and normalized iodine dissolution rate (IDR) measured through dynamic leach tests of the HIP Ag-mordenite samples. 22

Figure 3-8. The normalized silicon dissolution rate (left) and normalized iodine dissolution rate (IDR) measured through dynamic leach tests of the SFA samples. 22

Figure 3-9. The normalized silicon dissolution rate (left) and normalized iodine dissolution rate (IDR) measured through dynamic leach tests of the HIP Iodosodalite samples produced at University of Birmingham. 23

Figure 3-10. The normalized silicon dissolution rate (left) and normalized iodine dissolution rate (IDR) measured through dynamic leach tests of the HIP iodosodalite samples produced at WSU. 24

Figure 3-11. The normalized silicon dissolution rate (left) and normalized iodine dissolution rate (IDR) measured through dynamic leach tests of the sintered iodosodalite samples. 24

Figure 3-12. The normalized silicon dissolution rate (left) and normalized iodine dissolution rate (IDR) measured through dynamic leach tests of the glass-bonded sodalite ceramics. 25

Figure 3-13. The normalized silicon dissolution rate (left) and normalized iodine dissolution rate (IDR) measured through dynamic leach tests of the Glass Composite material samples 26

Figure 3-14. The normalized iodine dissolution rate (IDR) measured through dynamic leach tests of the two IWF that were not silicon based. 26

Figure 3-15. Comparison of the normalized silicon dissolution rates over time from the extended C1220 tests. The tellurite glass is represented by silver dissolution and the iodoapatite as iodine as no silicon was present in either sample. 27

Figure 3-16. The IDR measured for the HIP 18-3 samples in a dynamic leach test where the leachate was not replaced at each interval and a subsample was collected from the leachate at each interval instead. The corresponding Si concentration within the leachate is also displayed. 30

Figure 3-17. The IDR (white) and resulting Si concentration from sample dissolution (red, calculated as the difference between the nominal Si concentration added to the leachant the measure Si in the leachate) measured during static tests with added Si to the leachant using the large-form Ag-mordenite samples HIP 18-2-1 (triangle) and HIP 18-2-2 (circle). 31

Figure 3-18. The IDR (white) and Si concentration from sample dissolution (red, calculated as the difference between the nominal Si concentration added to the leachant the measure Si in the leachate) measured during static tests with added Si to the leachant using the large-form Ag-mordenite samples HIP 18-3-1 (triangle) and HIP 18-3-2 (circle). 31

Figure 3-19. The IDR (white) and Si concentration from sample dissolution (red, calculated as the difference between the nominal Si concentration added to the leachant the measure Si in the leachate) measured during static tests with added Si to the leachant using the Silver Functionalized Silica Aerogels SPS-3 (triangle) and SPS-4 (circle). 32

Figure 3-20. Plot showing the normalized silicon dissolution rate from a single 1-day interval vs. the inverse test temperature. The R^2 values correspond to the specific samples analyzed. 33

Figure 3-21. Before and after SEM images of the HIP18-3 large-form Ag-mordenite (left: pre-leach SEM; right: post-leach SEM). The scale bar in the top right applies to both images. 35

Figure 3-22. Before and after SEM images of the HIP18-2 large-form Ag-mordenite (left: pre-leach SEM; right: post-leach SEM). The scale bar in the top right applies to both images. 35

Figure 3-23. Before and after SEM images of iodosodalite H1C5 (left: pre-leach SEM; right: post-leach SEM). The scale bar in the top right applies to both images. 36

Figure 3-24. Before and after SEM images of the tellurite glass (left: pre-leach SEM; right: post-leach SEM). The scale bar in the top right applies to both images. 36

Figure 3-25. Before and after SEM images of the sintered sodalite WSU52 (left: pre-leach SEM; right: post-leach SEM). The scale bar in the top right applies to both images. 36

Figure 3-26. Before and after SEM images of the sintered sodalite WSU8 (left: pre-leach SEM; right: post-leach SEM). The scale bar in the top right applies to both images. 37

Figure 3-27. Before and after SEM images of the glass-bonded ceramic NaIBR (left: pre-leach SEM; right: post-leach SEM). The scale bar in the top right applies to both images. 37

Figure 3-28. Before and after SEM images of the Ag-mordenite GCM (left: pre-leach SEM; right: post-leach SEM). The scale bar in the top right applies to both images. 37

Figure 3-29. Post-leach optical profilometry images for a) Te glass, b) NaI, c) Aero HIP 2, d) SPS-2, e) HIP 17-17, f) HIP 17-22. g) H1C5, and h) H1C8. 39

Figure A.1. SEM micrograph and the corresponding EDS maps of the HIPed Iodosodalite samples. 47

Figure A.2. SEM micrograph and the corresponding EDS maps of an example HIPed SFA samples. 48

Figure A.3. SEM micrograph and the corresponding EDS maps of the HIPed Ag-mordenite large-form samples. 50

Figure A.4. SEM micrograph and the corresponding EDS maps of the iodoapatite ceramic 50

Figure A.5. SEM micrograph and the corresponding EDS maps of the tellurite glass 50

Figure A.6. SEM micrograph and the corresponding EDS maps of the glass bonded sodalite samples. 51

Figure A.7. SEM micrograph and the corresponding EDS maps of the WSU sodalite samples. 52

Figure A.8. SEM micrographs and the corresponding EDS maps of the DS 60 Ag mordenite and the Tin Pellet samples. 53

Figure A.9. SEM micrographs and the corresponding EDS maps of the 71D and 55B Ag mordenite in GCM samples. 53

Figure A.10. SEM micrographs and the corresponding EDS maps of the sodalite WSU3 and WSU8 samples. 54

Figure A.11. Post-leach SEM micrograph and the corresponding EDS maps of HIPed iodosodalite sample H1C5. 54

Figure A.12. Post-leach SEM micrograph and the corresponding EDS maps of large-form Ag-mordenite sample HIP182-2. 55

Figure A.13. Post-leach SEM micrograph and the corresponding EDS maps of large-form Ag-mordenite sample HIP18 3-2. 55

Figure A.14. Post-leach SEM micrograph and the corresponding EDS maps of glass-bonded sodalite sample NaIBR. 55

Figure A.15. Post-leach SEM micrograph and the corresponding EDS maps of glass-bonded sodalite sample NaIBR. 56

Figure A.16. Post-leach SEM micrograph and the corresponding EDS maps of sodalite sample WSU 52.1. 56

Figure A.17. Post-leach SEM micrograph and the corresponding EDS maps of sodalite sample WSU 8. 56

Figure A.18. Post-leach SEM micrograph and the corresponding EDS maps of Ag-mordenite and GCM sample TMN 2009 1-71D. 57

TABLES

Table 1-1. Summary of the IWF test efforts performed and the major findings of the work. 2

Table 1-2. Comparison between the corrosion data of various IWF types available in the literature. Italicized values represent those which were not converted to $g/m^2/d$. 5

Table 2-1. IWF sample information showing the sample name, place of fabrication, prior testing reports, iodine content and tests the samples were included in for this report. 11

Table 3-1. Normalized dissolution rate, with respect to iodine, for the various samples evaluated in the 3-day screening test. Measurements with an associated error were performed with replicates. 21

Table 3-2. Summary of the average IDRs and SDRs measured in the dynamic leach tests. Samples without an associated error only had a single viable measurement at that interval. 28

Table 3-3. Comparison of the normalized dissolution rates with respect to I, Al, Si, and Ag for samples tested at multiple temperatures in a 1-day interval. 33

Table 3-4. Normalized dissolution rates for I and Si at the 3-day sampling interval with variable SA/V volume ratios. 34

Table A-1. Composition of the glass bonded sodalite samples measured by EDS. 57

Table A.2. Composition of the small-form Ag-mordenite samples measured by EDS 58
Table A.3. Composition of the large-form Ag-mordenite samples measured by EDS 58
Table A.4. Composition of the Ag-functionalized silica-based aerogels from EDS. 59
Table A.5. Composition of the iodoapatite ceramic, HIPed sodalites and tellurite glass measured by EDS 59
Table A.6. Composition of the Sintered iodosodalite from WSU measured with EDS 60

ACRONYMS

ADR	normalized silver (Ag) dissolution rate
ANS	American Nuclear Society
ANSI	American National Standards Institute
ASTM	ASTM International
DDI	double deionized water
DI	deionized
EDS	energy-dispersive X-ray spectroscopy
EPA	U.S. Environmental Protection Agency
FBSR	fluidized bed steam reforming
FY	fiscal year
GCM	glass composite material
HIP	hot-isostatic pressing
HIPed	hot isostatically pressed
IDR	normalized iodine dissolution rate
IWF	iodine-containing waste form
LSU	Louisiana State University
ORNL	Oak Ridge National Laboratory
MCC	Materials Characterization Centre
MOF	metal organic framework
PCT	product consistency test
PNNL	Pacific Northwest National Laboratory
SA	surface area
SDR	normalized silicon dissolution rate
SEM	scanning electron microscopy
SFA	silver-functionalized silica aerogels
SNL	Sandia National Laboratories
SPFT	single-pass flow-through test
SPS	spark plasma sintering
WSU	Washington State University
µXRD	micro-X-ray diffraction

Acknowledgements

The authors would like to make the following acknowledgements to colleagues and collaborators who contributed to this work. We thank the following people for supplying the test materials in this report, specifically: the Ag-mordenite samples were provided by Robert Jubin and Stephanie Bruffey of Oak Ridge National Laboratory, the silver-functionalized silica-based aerogel samples were provided by Josef Matyáš of Pacific Northwest National Laboratory (PNNL), the glass bonded sodalite ceramics were provided by Brian Riley of PNNL, the iodosodalite samples were provided by John McCloy of Washington State University and Saehwa Chong of PNNL, the hot-isostatically pressed iodosodalite samples were provided by Joseph Hriljac of the University of Birmingham, the tellurite glass was provided by Cheong Won Lee, John Heo, and Wooyong Um of Pohang Institute of Science and Technology, the tin pellet and glass composite material was provided by Tina Nenoff of Sandia National Laboratories, and the iodoapatite ceramic was provided by Jianwei Wang of Louisiana State University. The authors also wish to thank William Ebert and Jeff Fortner of Argonne National Laboratory for continued collaboration. Technical reviews of the document and data were provided by Brian Riley and Jim Neeway, and the authors appreciate their thorough review. Analytical work was performed by Steven Baum, Ian Leavy and Megan Nims of PNNL and sample polishing by Joelle Reiser, Viviana Gervasio and Anthony Guzman. The authors also thank Kimberly Gray, Terry Todd, and John Vienna for programmatic support.

1. INTRODUCTION

Within geologic repositories, the prediction of iodine release is required due to its long half-life (15.7 million years) and mobility in its anionic state as both oxidized (iodate, IO_3^-) and reduced (iodide, I^-) forms. Iodine is released during the dissolution step of used nuclear fuel reprocessing and must be captured to prevent its release to the air (40 CFR 61). The captured iodine must then be immobilized as a stable waste form for long-term disposal. A multitude of materials have been produced for iodine capture and resulting waste forms, including zeolites (mordenite and faujasite; Bruffey and Jubin 2018; Bruffey et al. 2017; Sheppard et al. 2006), sodalites (Chong et al. 2018, 2020; Nam et al. 2018), apatite (Yao et al. 2014; Zhang et al. 2018), and aerogels (Asmussen et al. 2018b; Matyáš et al. 2018; Riley et al. 2016. Ag mordenite, for example, can be used to capture and convert the iodine to a densified iodine-containing waste form (IWF) through hot-isostatic pressing (HIP). Other options for the conversion of the iodine-loaded material to a waste form include hot uniaxial pressing, spark plasma sintering (SPS), vitrification, or grouting to generate a durable IWF.

A predictive conceptual corrosion model for IWFs is required to facilitate long-term evaluations of iodine waste forms in a repository. The conceptual model must be supported with a test suite that can provide relevant corrosion data to parameterize the model and rapidly evaluate new iodine waste form types. Previous test methods have included ASTM International (ASTM) Method C1662-10 single-pass flow-through test (SPFT) (Asmussen et al. 2019), ASTM Method C1285-14 product consistency test (PCT) (Bruffey et al. 2015), and modified American National Standards Institute (ANSI)/American Nuclear Society (ANS) 16.1 testing (Asmussen et al. 2018a; Lawter et al. 2019). Each of these tests has its own associated challenges: SPFT is labor intensive, PCT requires destruction of the sample, and the ANSI/ANS 16.1 testing has irregular samplings which causes variable dissolution rates, although the sampling schedule was recently adjusted to be a shorter 7-day test.

This report is being provided as a summary to the evaluation of the corrosion behavior of several classes of IWFs, specifically the response of dynamic leach tests to a range of test variables and sample types. This report will support the upcoming development of a conceptual long-term corrosion model for IWFs. Ebert (2019) recently suggested using a modified C1220 testing procedure as a screening test for IWF durability using Ag-mordenite samples as a test case from a single 3-day interval. As a complement to this work, a series of modified C1220 tests was performed and demonstrated that the response of the waste form types was, for the most part, consistent beyond the 3-day time period (Lawter et al. 2019). As well, varying polishing finishes, silicone masking, and variable sample intervals were evaluated.

The data presented in this report serves two purposes: 1) expand the range of IWFs evaluated with the test suite to assess method variability and 2) further understand the corrosion of IWFs to best inform conceptual long-term corrosion model development. This report presents the dissolution data of a variety of IWF types, a review of available literature data on IWF, and microstructural information on the IWF following corrosion testing. Included in the testing matrix were multiple classes of IWFs, including hot isostatically pressed (HIPed) Ag-mordenite (Jubin et al. 2014), Ag-functionalized silica aerogels (SFA) processed by both HIP and SPS (Matyáš and Engler, 2013), HIPed sodalites, pressed iodosodalites, tellurite glass, glass composite materials and glass-bonded sodalite ceramics.

1.1 Summary of Prior IWF Test Efforts

Multiple efforts have been carried out by the Off-gas Sigma team to assess the durability of iodine waste forms. HIP Ag-mordenite and SFA have been the two IWF types most thoroughly studied. To achieve the programmatic goal of a conceptual long-term corrosion model for IWFs, some testing is still required to fill knowledge gaps (e.g., pH effects, resolving the possibility of AgI reprecipitation on the waste form surface), but initial development of the conceptual model should commence. Table 1-1 highlights the work done to date by the program, the information gained, and the primary findings of the work.

Table 1-1. Summary of the IWF test efforts performed and the major findings of the work.

Test Effort and Samples Included	**Findings**	**References**
PCT (ASTM Method C1285) HIPed Ag-exchanged mordenite (small form)	Cores were taken from HIP Ag-mordenite samples and crushed to a powder. Based on the PCT results, increasing the HIP temperature from 525°C to 900°C resulted in a substantial decrease in iodine released during the PCT test. Further increasing the pressing temperature to 1100°C did not improve durability.	Bruffey and Jubin. (2015)
Electrochemical Tests	The report studied AgI dissolution rates over various pH and E_h conditions using potentiostatic methods. The results show there is reductive dissolution of AgI within the cathodic region and the observations are in good agreement with predicted thermodynamic stabilities.	Ebert et al. (2017)
SPFT (ASTM Method C1662) HIPed Ag-exchanged mordenite (small form. ORNL HIP 17-3, 17-7, and 17-8); SPSed SFA (Fiscal Year (FY)18 SPS-1 and SPS-2)	The SPFT method studied IWF dissolution using monolithic samples. For the Ag-exchanged mordenite, preferential corrosion was observed on secondary phases that contained higher amounts of Al and alkali species but were lower in I content. At higher temperatures and lower pH (pH = 7 or 9), the normalized Ag dissolution rate (ADR) was higher than the normalized silicon dissolution rate (SDR), but at pH 11, SDR was higher than ADR. For the SPSed SFA samples, preferential corrosion occurred at Si-rich particles, making small AgI isolations near these particle boundaries susceptible to dissolution. Addition of Si to the SFA waste forms increased the durability. The SDR of both IWF types was comparable to other Si-based IWFs.	Asmussen et al. (2019)
Suggestion of test method N/A	This letter report provided the first guidance on use of a dynamic leach test to alleviate the challenges with PCT and SPFT for IWF evaluation. *"The test method used to assess the effect of production parameters on the quality of IWF materials must focus on degradation of the encapsulating matrix, which is not sensitive to the solution redox conditions (Eh) and eliminates the need to maintain low O_2 levels during the test. The primary measures of waste form quality are chemical durability and porosity (or bulk density) of the encapsulating matrix, and those will be affected by the phase composition and microstructure of the matrix material."* The report suggests the use of test results to assess processing effects and benefits of using a test method similar to consensus standard methods ASTM C1308 and ANS 16.1.	Ebert (2018)

Test Effort and Samples Included	Findings	References
Dynamic leach test based on ANS/ANSI Method 16.1 (Method sensitivity testing) Large- and small-form Ag-mordenite HIP samples; Ag-functionalized silica aerogels, sodalites, glass-bonded sodalite ceramics, iodoapatite ceramics, tellurite glass	The degree of surface polishing had little to no impact on the IWF dissolution rate. 600 grit was recommended for future tests. Silicone masking on the bottom of the sample coupons was used in previous tests to limit dissolution to only the polished surface. Tests were conducted with and without silicone masking to determine if the mask is required for accurate results. Most samples with and without silicone masking had similar results, while some masked samples had increased silicone concentrations, which may have come from the silicone mask. It is recommended that silicone masking not be used in future tests, and if it is used, the silicone mask should be allowed to cure for several days prior to testing. Skipping the multiple, short initial sampling intervals resulted in lower dissolution rate, likely due to solution feedback in the longer intervals. The common ion effect was observed in tests where solution was not refreshed, and the dissolution rate slowed with time.	Lawter et al. (2019)
Screening test assessment Ag-mordenite (small form)	Using prior test data, the report evaluated the ASTM C1308 test method. Suggested a single 3-day interval test can be used to screen IWF quality.	Ebert (2019)
Screening test and dynamic leach test (based on ASTM Method C1220) Large- and small-form Ag-mordenite HIP samples; Ag-functionalized silica aerogels, sodalites, glass-bonded sodalite ceramics, iodoapatite ceramics, tellurite glass	The 3-day screening test was sufficient to screen waste form durability for most of the IWFs tested and allowed accurate comparisons between samples with similar composition but different processing conditions. Extending the 3-day tests with consistent intervals showed mostly consistent normalized dissolution rates. However, some sodalites and one small-form Ag-mordenite HIP sample showed increased variability beyond the initial 3-day sample.	Lawter et al. (2019)
Electrochemical methods Large-form HIP Ag-mordenite	Electrochemical analysis of the galvanic coupling between the HIP Ag-mordenite matrix and the steel canister wall was evaluated at pH 4-10. It was found that the AgI inhibited the steel passivation and may cause a loss of integrity once a canister has failed. This galvanic coupling observed should be included in a long-term dissolution model.	Ebert et al. (2019)

1.2 Review of IWF Literature Data

The programmatic goal of having a conceptual long-term corrosion model for IWF requires datasets collected uniformly that can be used to parameterize the model. With the long-term immobilization of iodine being a challenge throughout the global nuclear community, many IWF types have been developed. As part of their development, durability is commonly assessed. However, the methods through which the release of iodine from the waste form is studied are highly varied.

A review of the available IWF durability data in the literature is provided in Table 1-2 to highlight the variability of test methods and the IWF data that exists to date. Materials that have durability data include hydroxyapatites, iodosodalites, cementitious materials, sodalites, metal organic frameworks (MOFs), bismuth glass, glass bonded iodosodalites, Bi-embedded mesoporous silica, alumina sorbents, zeolites, glass composite materials, lead vanadates, fluidized bed steam reforming (FBSR) granules, calcium phosphates, alumina silver phosphate glass, lead borate glasses, magnesium phosphate ceramics, cesium bismuth composites, and natural materials. The range of tests performed covers nearly all waste form evaluation methods and includes Material Characterization Center (MCC) methods MCC-1 and MCC-5, PCT (ASTM Method C1285), SPFT (ASTM Method C1662), dynamic leach (ASTM Method C1308), dynamic flow through, U.S. Environmental Protection Agency (EPA) methods, and ANS/ANSI Method 16.1. A variety of leachants have been used, including deionized (DI) water, simulated groundwater, and buffered solutions. Test temperatures have ranged from room temperature up to 100°C and test durations from hours to upward of 75 days.

The rates presented have been converted, where possible, to a consistent unit of $g/m^2/d$ that is used within this report. If different units are presented where the conversion was not possible, the units are listed beside the value. The most durable IWFs have dissolution rates on the order of 10^{-7} $g/m^2/d$ in the conditions used and 10^{-5} $g/m^2/d$ in test conditions similar to those described in this report.

Defining a consistent, consensus corrosion testing protocol is crucial to mature a conceptual model for IWF corrosion. The summary of IWF data presented in Table 1-2 highlights this need. It is challenging to extract data from various tests to use in the same model due to the nuances associated with each method. The test suite defined through this program – a short screening test and a dynamic leach test – can meet these needs and support material design efforts as well as provide useful data for the eventual conceptual long-term dissolution model.

Table 1-2. Comparison between the corrosion data of various IWF types available in the literature. Italicized values represent those which were not converted to $g/m^2/d$.

Material/ Reference	Sample Name	Iodine loading (wt%)	Durability Test Type	Leachant	Temp. (°C)	Duration/ Intervals	Rate ($g/m^2/d$)
Hydroxyapatite/Coulon et al. (2017)	Stochiometric HA-CaI at 90C; SPS (s-HA-CaI)	10±1	Modified MCC1 (unsaturated)	Deionized water (DI)	50	---	$2.00\times10^{-2} \pm 2.00\times10^{-3}$
					40		$1.50\times10^{-2} \pm 2.00\times10^{-3}$
					30		$1.00\times10^{-2} \pm 2.00\times10^{-3}$
	s-HA-CaI	10±1	Modified MCC1 (saturated)		50	60 d	$(7\pm1)\times10^{-5}$
	cd-HA-CaI	7±1					$(1\pm0.1)\times10^{-5}$
	s-HA-CaI	10±1		Clay-equilibrated groundwater			1.00×10^{-4}
	cd-HA-CaI	7±1					$(2\pm1)\times10^{-5}$
Ca Hydroxyapatite/ Hassan and Ryu (2019)	IO-HAp, cold sintered	~7	PCT	DI	90	7d	$(2.4\pm0.4)\times10^{-5}$
Iodosodalite/ Hassan et al. (2020)	Cold-sintered iodosodalite	13.8±0.6	PCT	DI	90	7d	$(7.9\pm0.04)\times10^{-4}$
AgIZ in Grout/ Kaplan et al. (2019)	Grout - slag + AgIZ	0.83	---	Grout-equilibrated solution	Room temp	1d, 4d, 7d, 14d, 30d, 60d	5.13×10^{-3}
	Grout + slag - AgIZ	1.99	---				1.23×10^{1}
Sodalite/ Neeway et al. (2016)	P1BG	0.06	SPFT	pH 9 solution	40	28d-74d	$(28\pm8)\times10^{-4}$
	BSRG	0.07					$(32\pm8)\times10^{-4}$
	LAW1 (SX-105)	0.00087					ND
MOFs in GCM/ Sava et al. (2012)	GCM-1 (EG2998 glass + I in ZIF-8 MOF)	12	PCT	DI	90	7d	2.12×10^{2}
	GCM-2 (EG2922 glass + I in ZIF-8 MOF)						4.43×10^{-1}
	GCM-3 (EG2998 glass + I in HKUST-1 MOF)	15					ND
	GCM-4 (EG2922 glass + I in HKUST-1 MOF)						ND
	LGC106 (glass eq. to EG2998)	2.50	PCT	DI	90	7 d	7.80×10^{-3}

Material/ Reference	Sample Name	Iodine loading (wt%)	Durability Test Type	Leachant	Temp. (ºC)	Duration/ Intervals	Rate ($g/m^2/d$)
Bismuth based capture with glass/ Yang et. al (2016)	LGC206 (glass eq. to EG2922)	1.60					1.70×10^{-2}
Iodoapatite/ Zhang et al. (2018)	Iodoapatite (prepared with high-energy ball milling and SPS)	---	ASTM C1308	DI	90	2h, 5h, 17h, then every 24 h	2.30×10^{-3}
Glass-bonded iodosodalite/ Chong et al. (2018)	10N-750 (using 10% NBS-4 for GB); S/V of 8 m^{-1}	8-9	ASTM C1308	DI	90	Every 7d between 10d-24d	1.29×10^{0}
	10N-750 (using 10% NBS-4 for GB); S/V of 80 m^{-1}						1.70×10^{-1}
	10N-750 (using 10% NBS-4 for GB); S/V of 1000 m^{-1}		PCT			14-28d interval used	0.20×10^{-4}
Copper iodide/ Vance et al. (2018)	HIPed CuI (no metal added)	60	PCT	DI	90	7d	1.61×10^{2}
Bi-embedded SBA-15/ Yang et al. (2016)	CD-IP (heat treated and mixed with Bi_2O_3)	13	PCT	DI	90	7d	1.10×10^{2}
	Bir-SBA-15-2A-I (not mixed with Bi2O3)	54	MCC-1	DI	90	0d-21d	7.90×10^{0}
AgI in alumina sorbents/ Vance et al. (2005)	AgI in Al, HIPed in Sn/Cu HIP can	10 (prior to HIP)	---	---	---	---	$<6.00\times10^{-5}$
Ag I Sodalite/ Maddrell et al. (2019)	Ag exchanged zeolite	---	MCC-1	DI	90	7d	$<4.00\times10^{-4}$
Bi-Si-Zn GCM/ Mowry et al. (2015)	5-33 (A&B)	0.5	PCT	DI	90	7d	3.26×10^{-1}
	5-33 (C&D)		MCC-1				1.40×10^{1}
	5-33 (I&J)	7.8	PCT				5.08×10^{-2}
	5-33 (K&L)		MCC-1				1.61×10^{0}
FBSR/Neeway et al. (2016)	Iodine-containing FBSR	---	ASTM C1662	HNO_3	40	---	1.00×10^{-4}

Material/ Reference	Sample Name	Iodine loading (wt%)	Durability Test Type	Leachant	Temp. (ºC)	Duration/ Intervals	Rate (g/m^2/d)
GCM with AgZ/Mowry et al. (2015)	Bi-Si-Zn oxide glass composite material contained AgZ	---	ASTM C1662	NaCl/HCl	---	---	1.00×10^{-3}
Apatite/Guy et al. (2002)	$Pb_{10}(VO_4)_{4,8}(PO4)_{1,2}I_2$	---	---	DI	90	---	2.40×10^{-3}
Lead iodovandadate/Maddrell and Abraitis, (2003)	$Pb_5(VO_4)_3I$	---	---	0.025 M $KHCO_3$ + 0.015 M KOH	90	14d	1.50×10^{0}
Apatite/Adubert and Lartigue, (2000)	$Pb_{10}(VO_4)_{4,8}(PO_4)_{1,2}I_2$	---	Dynamic flow through	DI	90	20d	2.50×10^{-3}
Lead iodovanadate/Suertsugu (2014)	$Pb_{10}(VO_4)_6I_2$	---	---	DI	90	56d	8.80×10^{-3}
Lead iodovanadate/Zhang et al. (2018)	$Pb_{9.85}(VO_4)_6I_{1.7}$	---	ASTM C1308	DI	90	25d	2.00×10^{-3}
NaI Iodosodalite/Chong et al. (2018)	$Na_8(AlSiO_4)_6I_2$	---	ASTM C1308	DI	90	14d	7.50×10^{-5}
Iodoapatite/Coulon et al. (2017)	$Ca_{10}(PO_4)_6(IO_3)_{0.92}(OH)_{1.08}$	---	----	DI	50	7d	1.00×10^{-3}
Lead iodovanadate/Zhang et al. (2019)	$Pb_{9.85}(VO_4)_6I_{1.7}$	---	ASTM C1308	NaCl, Na_2CO_3, Na_3PO_4, Na_2SO_4 and DI	90	14d. 7d for tests using DI	5.76×10^{-6}; 1.11×10^{-6}; 3.66×10^{-6}; 5.56×10^{-6}; 2.91×10^{-7}
HIP Sodalite/Maddrell et al. (2014)	HIP iodosodalite at 900 ºC or 1100 ºC	---	---	$HKCO_3$, KOH	90	3d, 7d, 14d	5×10^{-3} - 1×10^{-2}
Ag sodalite/Maddrell et al. (2019)	Silver sodalite $Ag_{84}Na_2Al_{86}Si_{106}O_{384}$	----	ASTM C1285-02	DI	90	7d	1.57×10^{-2}
Ag phosphate glass/Yang et al. (2017)	Al_2O_3 silver phosphate glass	---	ASTM C1285-02	DI	90	7d	1.00×10^{-4}
Caststone/Serne et al. (2016)	Caststone	---	EPA 1315	DI	20	63d	8.41×10^{-10} cm^2/s
Caststone/Asmussen et al. (2016)	Caststone Ag-mordenite	---	EPA 1315	DI	20	63 days	3.54×10^{-9} cm^2/s
	Caststone Argentite						2.59×10^{-9} cm^2/s
Caststone/Saslow et al. (2017)	Caststone with hydrated lime	---	EPA 1315	DI	20	28d-63d	7.53×10^{-8} cm^2/s

Material/ Reference	Sample Name	Iodine loading (wt%)	Durability Test Type	Leachant	Temp. (ºC)	Duration/ Intervals	Rate ($g/m^2/d$)
Caststone/Saslow et al. (2019)	AP-105 Off Gas Cast Stone	---	EPA 1315	DI	20	63d	1.52×10^{-8} cm^2/s
Caststone/Saslow et al. (2018)	Caststone Ag-mordenite	---	EPA 1315	DI	20	28d-63d	2.19×10^{-7} cm^2/s
Caststone/Saslow et al. (2017)	Caststone Ag-mordenite	---	EPA 1315	DI	20	63d	2.19×10^{-7} cm^2/s
Hydroxyapatite/Campayo et al. (2011)	Iodate-incorporated hydroxyapatite	---	MCC-1	DI	90	---	1.43×10^{-7}
Lead vanadate/Guy et al. (2002)	Apatite: lead vanadate (PbV) (I)	---	MCC-1	DI	90	---	2.79×10^{-6}
Ag phosphate glass/Yang et al. (2017)	Silver phosphate glass (I)	---	ASTM C1285	DI	90	---	1.70×10^{-8}
Sodalite/Maddrell et al. (2019)	Silver iodate sodalite (I)	---	MCC-1	DI	90	---	1.60×10^{-6}
Lead iodoapatite/Uno et al. (2001)	Lead iodoapatite (I)	---	MCC-5	DI	90	---	5.53×10^{-4}
Sodalite/Babad et al. (1980)	$(3M_2O)(3Al_2O_3)(6SiO_2)(2MX)$ (I)	---	MCC-5	DI	100	---	7.00×10^{-3}
Glass/Tanabe et al. (2010)	$PbO\text{-}B_2O_3$-based glass (I)	---	---	0.55M NaCl	20	---	5.00×10^{-5}
Mg/K phosphate/Vinokurov et al. (2009)	Magnesium potassium phosphate matrices (I)	---	ANS 16-1	DI	90	---	1.12×10^{-4}
Ag mordenite/Lawter et al. (2019)	Ag-exchanged mordenite (HIP 17-8) (I)	---	ASTM C1220-10	DI	90	---	1.80×10^{-6}
Si aerogels/Asmussen et al. (2019)	Ag-functionalized silica aerogels (I)	---	ASTM C1662-17	DI	90	---	2.30×10^{-6}
$Cs_3Bi_2I_9$-silica /Yang et al. (2020)	$Cs_3Bi_2I_9$-silica composite (70wt.%)	---	ASTM C1308	DI	90	---	5.95×10^{-6}
	$Cs_3Bi_2I_9$-silica core–shell (20wt.%)						8.00×10^{-10}
Granite, concrete, bentonite/Szántó et al. (2002)	Iodine in granite, concrete, and bentonite	---	---	Synthetic groundwater	23	---	$6.0 – 26.0\times10^{-12}$ cm^2/s

Abbreviations (order of appearance)
HA = hydroxyapatite
MOF = metal organic framework
GCM = glassy composite material

Material/ Reference	Sample Name	Iodine loading (wt%)	Durability Test Type	Leachant	Temp. (ºC)	Duration/ Intervals	Rate ($g/m^2/d$)

SPS = spark plasma sintered
PCT = product consistency test (ASTM C1285)
MCC = Materials Characterization Centre
DI = deioinized water
AgIZ = silver iodide zeolite
SPFT = single pass flow through (ASTM C1662)
ND = non-detect
GB = glass bonded
HIP = hot isostatically pressed
FBSR = fluidized bed steam reforming
EPA = U.S. Environmental Protection Agency
M = metal cation species
X = anion species

2. MATERIALS AND METHODS

2.1 Sample Preparation

A variety of IWF samples were collected from multiple sources and are listed in Table 2-1. The exposed faces of the samples were polished to 600 grit (30 µm). Previous studies have shown that the degradation of IWF is not affected by polish finish beyond 600 grit (Lawter et al. 2019). Due to the small sample size and physical structure, the sintered iodosodalites [Washington State University (WSU) sample labels] and glass-bonded sodalite ceramics samples could not be polished. Photographs of select sample coupons are shown in Figure 3-1.

The exposed surface area of each coupon in the test was measured using ImageJ (Schneider et al. 2012). As needed, waste forms were cut using a diamond saw to produce a testable monolith. For example, the large-format HIP cans were received in sealed canisters; these were cut into 2- to 4-mm horizontal slices to use in testing.

The large- and small-form HIP Ag-mordenite samples were produced at Oak Ridge National Laboratory (ORNL). The small-form HIP samples were produced using by HIP pressures and temperatures of 900 °C and 175 MPa, but the samples were HIPed for different durations: 3 h (HIP 17-8) and 12 h (HIP 17-17 and HIP 17-22). The HIP 17-22 sample was dried at 450 °C prior to the HIP process (Jubin et al. 2014, Bruffey et al. 2017).The large-form samples have either high iodine loading (HIP 18-3 and HIP 18-4; 100% iodine capacity) or low iodine loading (HIP 18-1 and HIP 18-2; ~30% iodine capacity); all large-form samples were dried at 150 °C and then HIPed at 900 °C and 300 MPa for 3 h (Bruffey and Jubin 2018).

The iodoapatite Pb-V ceramic (LSU) was prepared by synthesizing iodoapatite using high energy ball milling, followed by an annealing step at 200°C. The iodoapatite was then densified using SPS.

Five HIPed iodosodalite samples were received from the University of Birmingham and were produced in 2008. The samples were prepared using AgI added to zeolites, and upon HIPing would generate an Ag-iodosodalite (Sheppard 2009). Samples H1C5 and H1C6 were prepared using a silver zeolite from Ionex™ with 100% iodide loading and 50% iodine loading, respectively. The AgI was occluded in the samples. Samples H1C8 and H1C9 used an Ag A-type zeolite loaded at 100% and 50% occluded iodine loading, respectively. Sample H1C11 was a hydrothermally prepared AgI sodalite that served as a control in the original study. All samples were HIPed at 900 °C and 190 MPa for 2 h.

Iodosodalites from WSU were hydrothermally synthesized, then mixed with either 10% NBS4 (WSU10 and WSU40) or 10% SA800 (WSU 22 and WSU 52). All the samples were then sintered at 750 °C (Chong et al. 2018). WSU 3 and WSU 8 contained 20% NBS4 glass binder and were sintered at 900 °C, but WSU 3 was hydrothermally synthesized and WSU8 was produced using aqueous synthesis (Chong et al. 2020).

Silver-functionalized silica-based aerogels (SFA) were tested with two processing methods: SPS and HIP (as designated in the sample names). The SPSed SFA samples were heated to 1200°C and held for 30 minutes at 70 MPa. The HIP SFA samples were heated at 1200°C for 30 min at 207 MPa.

Te glass was produced by heating a mixture of TeO_2, Ag_2O, Bi_2O_3, and AgI in crucibles at 700°C for 30 min (Lee at al. 2016).

NaI and AgI are glass-bonded ceramic samples with the main difference being the iodine source in the materials being one of NaI or AgI. These samples are highly porous.

IWFs received from Sandia National Laboratories (SNL) were produced by adding AgI-mordenite and silver flake to EG2922 glass. The mixtures were uniaxially dry pressed (550 °C and 70 MPa for 1 h) (Mowry et al. 2015). TMN2019-1-71D has a shell made of EG2922 and SiO_2 with one open face, TJG2010B 55B has a thin casing around the sample with one open face, and DS-60 has no shell or casing.

Table 2-1. IWF sample information showing the sample name, place of fabrication, prior testing reports, iodine content and tests the samples were included in for this report.

IWF Name	IWF type	Individual Samples	Previous Testing or Preparation	Supplied By	Polish (Y/N)	Iodine Content (mass%)	Tests
ORNL HIP17	HIPed Ag-exchanged mordenite	HIP17-8, HIP17-17, HIP17-22	Asmussen et al. (2019); Bruffey et al. (2017)	ORNL	Yes	3-6%*	Interval tests, variable temperature, variable surface area (SA):solution volume (V) ratio
ORNL HIP18	HIPed Ag-exchanged mordenite, large form	HIP18-1 and HIP18-2 (100% I capacity) and HIP-18-3 and HIP18-4 (30% I capacity). Two replicates of each.	Bruffey and Jubin (2018)	ORNL	Yes	6.5% or 13.5%	Interval tests, No refresh, polishing, variable SA/V ratio
LSU	Iodoapatite Pb-V ceramic	LSU	Yao et al. (2014); Zhang et al. (2018)	LSU	Yes	7%*	Interval tests, variable SA/V ratio
WSU	Glass-bonded iodoodalite	WSU40, WSU52, WSU10, WSU22	Chong et al. (2018); Nam et al. (2018)	WSU	No	18-22%	Interval tests, variable SA/V ratio
WSU	Iodosodalite, HIPed with 20 wt% glass binder	WSU3 (hydrothermal synthesis), WSU8 (aqueous synthesis)	Chong et al. (2020)	WSU	Yes	20-22%	Interval tests
Aero-SPS	SPSed SFA	Aero SPS 1, Aero SPS, Aero SPS-3 and Aero SPS-4 (four replicates)	Asmussen et al. (2019); Matyáš et al. (2018)[1]	PNNL	Yes	30%	Interval tests, SPFT, Si masking, variable temperature, variable SA/V ratio
Aero-HIP	HIPed SFA	Aero HIP 2	Matyáš et al. (2018)	PNNL	Yes	30%	Interval tests, Si masking, variable SA/V ratio
Iodosodalite	HIPed iodosodalites	H1C5, H1C6, H1C8, H1C9, H1C11	Sheppard et al. (2006)	U. of Birmingham	Yes	3-9%*	Interval tests, variable SA/V ratio
Te glass	Tellurite glass	Te glass	Lee et al. (2016)	POSTECH	Yes	12%*	Interval tests

IWF Name	IWF type	Individual Samples	Previous Testing or Preparation	Supplied By	Polish (Y/N)	Iodine Content (mass%)	Tests
Glass-bonded sodalite ceramics	NaI and AgI forms	NaIBR, AgIBR	Riley et al. (2019)	PNNL	No	15%*	Interval tests, variable SA/V ratio
Glass composite material (GCM)	AgI-mordenite encapsulated in a Bi-Si-Zn oxide glass (10% silver, 20% MOF, 70% EG2922 glass),	DS-1-3-912-60	Mowry et al. (2015), Nenoff et al. (2015)	SNL	Yes	1-2%	Interval tests
	76% glass, 19% AgI-Mordenite zeolite with 5% Ag flake core; shell contains EG2922 glass and SiO_2	TMN2019-1-71D		SNL	Yes	5.2%*	Interval tests
	Ag-mordenite core with a thin casing and exposed top	TJG2010B 55B		SNL	Yes	4.2%*	Interval tests
AgI-mordenite tin pellet	AgI-mordenite mixed with Sn	TJG-Tin pellet	Unpublished	SNL	Yes	2%	Interval tests

*Iodine content determined using SEM/EDS quantification.
LSU = Louisiana State University; ORNL = Oak Ridge National Laboratory; PNNL = Pacific Northwest National Laboratory; SNL = Sandia National Laboratories SEM/EDS = scanning electron microscopy / energy dispersive X-ray spectroscopy; WSU = Washington State University.
[1] This reference describes the general preparation of the SPSed aerogels, but does not describe the specific aerogels used in this testing.

2.2 Test Suite

In the continuing effort to define a standard test method to evaluate IWFs and generate data for a predictive model, dynamic leach testing was performed. The dynamic leach test uses near-constant leach intervals (weekend samplings avoided). The dynamic leach test uses a test temperature of 90 °C, a leachant volume to surface area ratio of 10 mL:cm^2, sample placed on the bottom of the vessel, and a complete leachant refresh at each sampling interval. In some cases, the sample geometry and leach vessel used created a scenario in which the target leachant volume did not fully cover the sample. In these cases, a measured amount of extra leachate was added. Errors were reported when replicate tests were available; however, the unique nature of the samples prevented repeat runs or some coupons were too fragile to run multiple tests and therefore only one test is reported.

2.2.1 Screening and Dynamic Leach Test

For the purpose of this report, the dynamic leach test used was based on the ASTM C1220-17 test method. In this test, a consistent 3-day sampling interval schedule was used. Based on prior testing, a regular sampling schedule is preferred for IWF evaluation (Ebert 2019; Lawter et al. 2019).

The volume of leachate for each test, per the standard, was determined by multiplying the surface area of the sample (cm^2) by 10 ± 0.2 cm (assuming 1 cm^3 of DI water = 1 mL). The HIP 18 (large-form Ag-mordenite) samples used a ratio of 100 mL:m^2 for "no refresh" tests (Sections 3.3.2 and 3.3.3, respectively). For coupons that had a small surface area and therefore had a low volume of leachant, the leachant was increased to 7 to 10 mL minimum to provide enough sample volume for analysis. For some coupons, the volume calculated based on the surface area was not enough to fully submerge the coupon; in these cases, the volume was increased to cover the coupon (including LSU apatite, DS-60, WSU52, WSU40, WSU22, NaIBR, and AgIBR). The influence of the SA/V ratio is discussed in Section 3.3.3. All tests were performed at 90 °C except for the temperature tests described in Section 3.3.2.

2.2.1.1 Alternate Test Variables

In addition to following the procedure above, variable testing conditions were implemented to assess sensitivity of the test and gain valuable information to inform the conceptual IWF corrosion model. The following variables were implemented for select samples:

1. Temperature: Waste form dissolution measurements are commonly performed at higher temperatures to accelerate dissolution. This is done with an expected linear response to temperature increases without altering the dissolution mechanism. This behavior was evaluated for the IWF by performing tests at 23 °C, 40 °C, 70 °C, and 90 °C using the small-form HIP Ag-mordenite samples (HIP17-2, HIP17-6, HIP17-8, HIP17-17, HIP17-18, and HIP17-22) and SON68 glass. This temperature test set will help to determine if a temperature dependence, or corresponding activation energy term, is required in the conceptual long-term corrosion model.
2. Sample Surface Area (SA)/solution volume(V) ratio: Within a repository, the disposed waste forms will experience an evolving near-field environment. Depending on water migration rates and the repository type the near field will most likely become increasingly saturated with dissolved components from the waste forms. For silicon-based materials, a common ion effect would result from this behavior and the corrosion rate of the material would slow with increased dissolved component concentration in the near field (Pierce et al. 2008). This scenario can be replicated in the dynamic leach tests by changing the waste form SA/V ratio. Smaller ratios will generate test conditions that are more dilute, and the waste form may corrode faster. These tests will help direct if the model should account for the influence of dissolved components and degree of saturation in the near field.
3. Silicon addition: Many of the IWFs evaluated are silicon-based. In the corrosion testing of borosilicate glasses, near-field concentration effects are commonly evaluated using a simplified

case of only the major component, Si, contributing to a slowed corrosion rate through the common ion effect. This effect is achieved by artificially adding Si to the leachant and observing the corresponding corrosion rate. Dynamic leach tests were performed on the IWF with added Si (15 and 45 ppm) to the leachant. These tests will assist in determining if the simplified case of the primary matrix component being used to represent solution feed-back should be applied in the conceptual long-term IWF corrosion model.

2.3 Solid Phase Characterization

2.3.1 Spectroscopy

The sample surfaces were imaged using SEM and elemental distribution in the images was determined using EDS. Element concentrations determined by EDS were used to normalize the dissolution data for each waste form. Images were collected at 70× and 250× magnification. SEM analyses were performed with a JSM-7001F microscope (JEOL USA, Inc.) with an XFlash 6|60 EDS Si-drift detector (Bruker) that was used to perform elemental mapping and spot analysis.

2.3.2 Micro-X-ray Diffraction (μXRD)

X-ray diffraction (XRD) patterns were collected from selected regions of the specimens using a Rigaku D-Max Rapid II microbeam diffractometer. X-rays were generated from a rotating Cr anode source (λ = 2.2910 Å) operated at 35 kV and 25 mA and focused to give a beam approximate 300 μm in diameter. The beam was positioned on areas of different appearance using a micrometer XY stage and optical camera integral to the diffractometer. The diffracted intensities were recorded on a large 2-dimensional image plate during a 10 min exposure and integrated to give a 1-dimensional powder diffraction profile. Crystalline compounds were identified through comparison with reference patterns (International Centre for Diffraction Data, PA) using JADE software (Materials Data Incorporated, CA).

2.3.3 Optical Profilometry

The topographical features of the sample surfaces following corrosion were observed for select coupons using optical profilometry on a Bruker GTK profilometer with a 5 × or 50 × lens.

3. RESULTS AND DISCUSSION

3.1 Sample Characterization

3.1.1 Optical Imaging

Example photographs of the samples used in this study are shown in Figure 3-1. Among the HIP Ag-mordenite samples, the main feature to note is the visual difference in surface morphology. The two large-form Ag-mordenite samples differed solely by the overall iodine loading, yet for the Ag-mordenite sample with lower iodine loading, the surface morphology was similar to that of the small form for Ag-mordenite with a "camouflage"-like pattern. However, the large-form samples with higher iodine loading have a green-ring composed of higher AgI levels surrounding a center with the camouflage pattern.

The porosity of the glass-bonded sodalite ceramics is evident from the photograph. The brittle nature of the sintered WSU iodosodalite sample prevented shaping or polishing of the sample. The glass composite material (GCM) shell surrounding the Ag-mordenite core is also evident.

Figure 3-1. Photographs of the samples evaluated in this study.

3.1.2 Scanning Electron Microscopy SEM

The individual samples were imaged prior to corrosion with SEM. EDS mapping was used to measure composition of the samples when the composition was not available from prior testing. The representative

micrographs are shown in Figure 3-2. The HIP Ag-mordenite showed similar microstructures in both the small form and the large form, despite the visual differences in Figure 3-1. For the SFA samples processed with either HIP or SPS, distinctly different microstructures were observed. The SPSed SFA sample appeared to have increased density in the microstructure when compared with the HIP SFA sample. The isolations in the micrograph of the iodoapatite ceramic sample were depleted in Pb/V. No distinct features were present in the tellurite glass. The sintered WSU iodosodalite samples were observed to have a degree of porosity, and iodine was observed to congregate near the outer rims of the void spaces. The HIP iodosodalites have a multiphase structure, with the bright regions visible in Figure 3-1 corresponding to locations of AgI. Samples from SNL include a tin pellet with uniformly distributed inclusions of Al/Si. A Ag-mordenite mixed with GCM sample created a low-porosity matrix, and the dark areas in the SEM represent the Ag-mordenite within the GCM. Finally, the glass-bonded sodalite ceramics had a highly porous structure. Full SEM and EDS images, along with sample compositions measured from EDS, are provided in Appendix A.

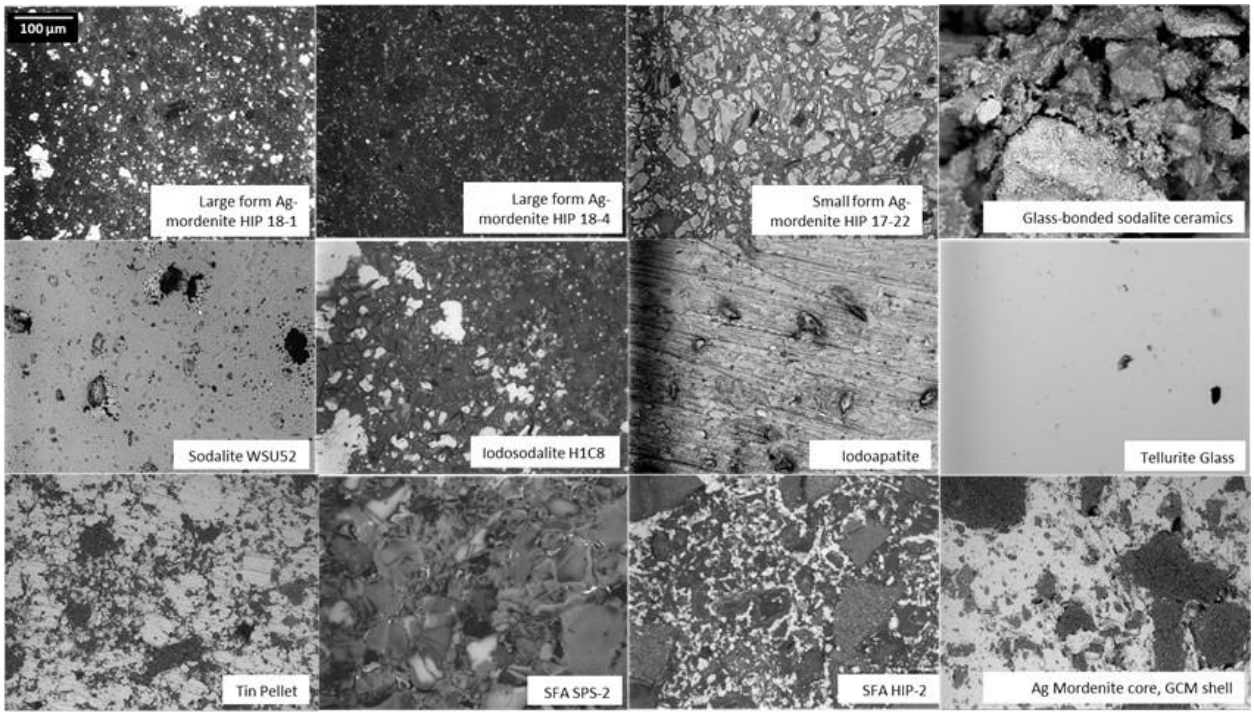

Figure 3-2. SEM micrographs of the various sample types used in this study prior to corrosion testing. All images were collected at 250×; the scale bar in the top left corner applies to all of the SEM micrographs.

3.1.3 µXRD of HIP Ag-Mordenite Large Form

To understand the evolution of the IWF surface during corrosion testing, µXRD was used to measure the crystallographic make-up of the large format Ag-mordenite samples before and after corrosion testing.

The HIP 18-3 sample (with loading of 100% iodine capacity) had a beige/green ring around the outer edge, shown in Figure 3-3 as the bottom black pattern. The inner brown colored area is shown on the top (blue) pattern. Peak matches are shown in the top right corner. The lighter outer area (tan colored) contains Ag metal (although a fairly minor amount) along with a smaller quantity of a cubic compound which could be (Na,K)Cl, quartz, and AgI, and a small amount of mullite from the zeolite material. The darker, inner regions in HIP18-3 had a distinct brown/red tint and were surrounded by a thin grey rim. The brown regions had much more Ag metal and there may be a tiny amount of hematite, which would help explain the color. There was no mullite, and less of the cubic compound, which perhaps is (Na,K)Cl.

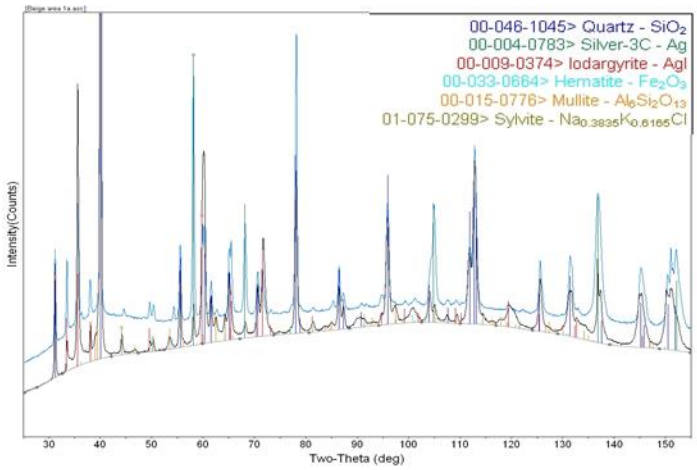

Figure 3-3. µXRD spectra for HIP18-3 (100% iodine capacity)

The HIP 18-3 sample was again characterized following the dynamic leach test and the resulting pattern is shown in Figure 3-4. Little to no changes were detected before and after leaching, although Ag metal in one region was reduced (although the brownish region did not show this and contained the most Ag metal).

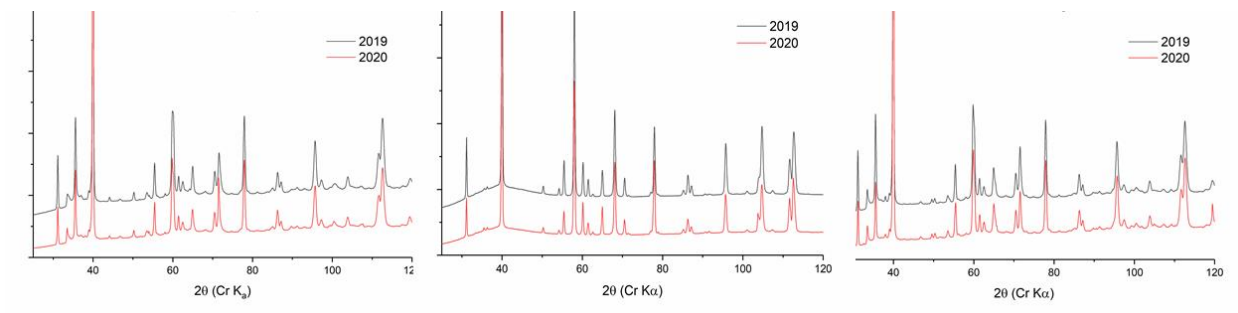

Figure 3-4. Pre- and post-leach test µXRD spectra for HIP 18-3, represented by 2019 and 2020, respectively. From left to right, the spectra represent the beige/green, brownish, and tan regions of HIP 18-3.

In HIP 18-2, Figure 3-5, the color was fairly uniform, but roughly rectangularly shaped regions that were a little darker than the surrounding, lighter matrix were discernable. This sample had dark and light regions, but they were less distinguishable and the spectra for both were very similar; only the darker region spectra is shown here. Peak matches are shown in the top right corner. The light area was quartz, AgI, and a little mullite ($Al_6Si_2O_{13}$). There were a few very weak unidentified peaks. The darker area contained a tiny amount of Ag metal, the only significant difference between the two regions.

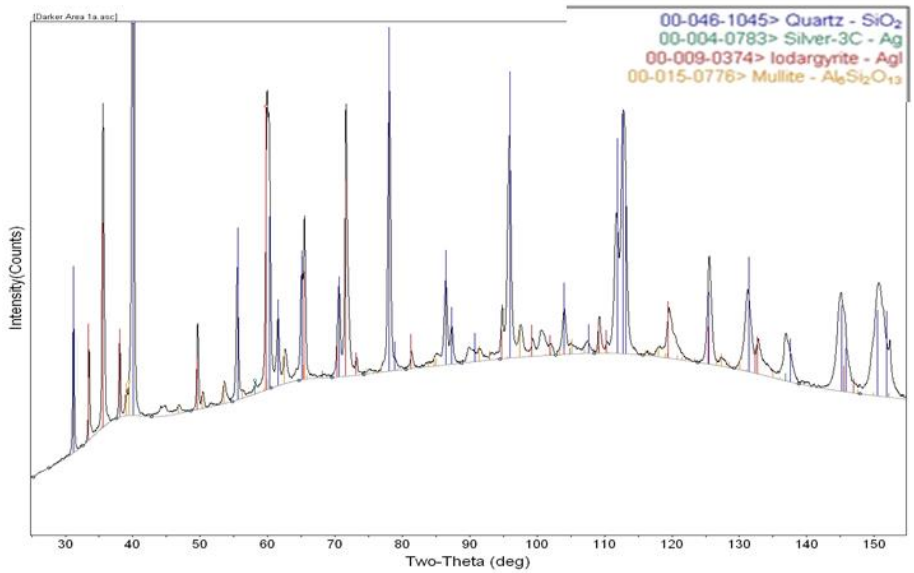

Figure 3-5. µXRD pattern for HIP18-2 (30% iodine capacity).

The HIP 18-2 sample was again characterized following the dynamic leach test and the resulting pattern is shown in Figure 3-6. No changes were detected before and after the leach testing in three different regions of the large-form HIP Ag-mordenite sample.

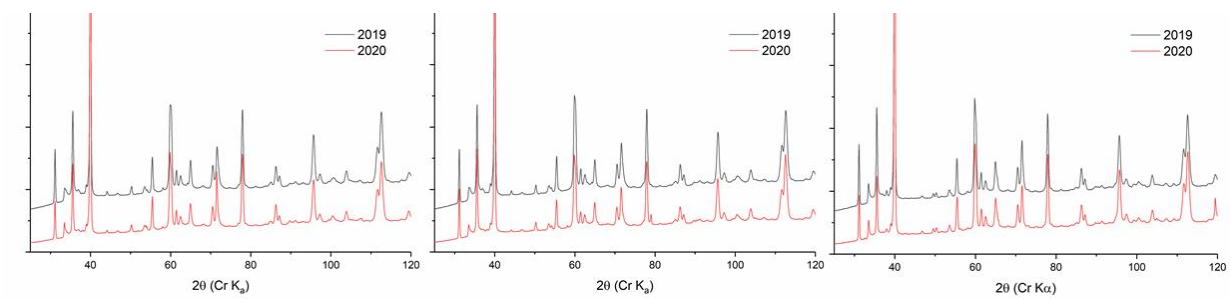

Figure 3-6. Pre- and post- leach test µXRD patterns for HIP 18-2, represented by 2019 and 2020, respectively.

3.2 Corrosion Testing

3.2.1 Iodine Waste Form Screening Test

It should be prefaced that none of the materials tested in this effort have been optimized for durability and the comparisons in this report are meant to be used for method development and to direct further material developments.

A 3-day-long, single-interval leach test has been proposed to rapidly compare the durability of iodine waste forms of the same material class (Ebert, 2018). From here on, the test will be referred to as a *screening test*. A benefit of the screening test is that after the initial interval the sample can be continued through the dynamic leach test protocol to assess long-term durability. The initial evaluation of the screening test was performed on HIP Ag-mordenite (Ebert, 2019). An expanded set of IWFs were placed in the screening test to assess the applicability of the test to a range of IWF and to assess consistency of the test in replicate run.

The resulting normalized iodine dissolution rates (IDRs) and normalized silicon dissolution rates (SDRs) are shown in Table 3-1. The error, when present, represents the deviation in duplicate tests.

Ag-mordenite – Between the two large-form samples, the HIP 18-2, which contained a higher iodine loading, measured a higher IDR ($4.70 \times 10^{-1} \pm 9.4 \times 10^{-2}$ g/m^2/d) and SDR ($6.33 \times 10^{-1} \pm 1.51 \times 10^{-1}$ g/m^2/d) compared with the lower iodine content HIP 18-4 sample (IDR = $1.27 \times 10^{-1} \pm 8.7 \times 10^{-2}$ g/m^2/d and SDR = $1.27 \times 10^{-1} \pm 8.7 \times 10^{-2}$ g/m^2/d). This result would suggest that the higher iodine loading and use of Ag may slightly decrease overall durability and iodine release. The original small-form samples were also evaluated. The HIP 17-17 sample, which was HIPed at 900 °C and 175 MPa for 12 h, had the lowest IDR ($8.90 \times 10^{-3} \pm 6.27 \times 10^{-3}$ g/m^2/d). The other two samples, HIP 17-22 and 17-8, which were HIPed for a shorter time (3 h), had higher IDR but similar SDR to HIP 17-17. Performing the screening test on all available HIP Ag-mordenite samples would provide valuable information on the influence of processing parameters on HIP Ag-mordenite durability listed in Table A-1 of Bruffey and Jubin (2018).

Ag-mordenite was also the basis for samples DS-60, TJG2010B-55B, and TMN-200-71-D. DS-60 had an IDR four orders of magnitude larger than the other two related samples, while the SDR of DS-60 was only one order of magnitude larger. TJG2010B-55B contained more Ag than DS-60, and TMN-200-71-D contained additional Ag flakes, which may have helped it outperform both DS-60 and TJG2010B-55B. The IDR was only slightly better in TMN-200-71-D compared to TJG2010B-55B (1.8×10^{-3} g/m^2/d vs. 2.49×10^{-3} g/m^2/d, respectively). The smaller difference in the SDR in TJG2010B-55B and TMN-200-71-D compared to DS-60 may have been caused by contributions to the Si concentration from the casing and shell of these two samples, which was not accounted for in the composition or SA measurements.

Silver functionalized silica-based aerogels – A clear difference in durability between SFA samples processed by different methods was evident from the screening test. The SPS samples measured nearly 100× lower IDR ($1.34 \times 10^{-3} \pm 9.4 \times 10^{-4}$ g/m^2/d and $1.39 \times 10^{-3} \pm 1.10 \times 10^{-3}$ g/m^2/d) compared with the HIP sample ($9.90 \times 10^{-2} \pm 6.11 \times 10^{-2}$ g/m^2/d). The SPS process results in a denser waste form, which clearly improved the overall iodine retention as suggested previously (Matyáš, 2016). The SDRs were similar for the HIP-2 sample and the SPS-2, but the SPS-1 sample measured several orders of magnitude lower. The reason for this SDR difference is unknown.

HIPed iodosodalite – The five HIPed sodalite samples, representing three different starting zeolite materials and differing iodine loadings, measured a range of IDRs and SDRs. The H1C8 ($1.51 \times 10^{-2} \pm 2.03 \times 10^{-2}$ g/m^2/d) and H1C9 ($8.27 \times 10^{-2} \pm 1.71 \times 10^{-1}$ g/m^2/d) samples measured the highest IDRs. The H1C8 and H1C9 samples were fabricated using an Ionex™ zeolite with AgI. The H1C11 sample measured the lowest IDR of $2.19 \times 10^{-4} \pm 1.98 \times 10^{-4}$ g/m^2/d. Interestingly, the H1C8 and H1C9 measured an SDR on the same order of magnitude as the H1C11 sample.

For the two additional HIP iodosodalite samples from WSU, WSU3 (composed of hydrothermally synthesized iodosodalite) had a slightly higher IDR and SDR compared to WSU8, which was synthesized aqueously. This may indicate that the method of synthesis could also influence the durability of iodosodalite IWFs; however, these samples were not run in duplicate and further testing is needed.

Sintered iodosodalite (WSU) – The WSU22.1 ($1.52 \times 10^{1} \pm 2.00 \times 10^{-1}$ g/m^2/d) and WSU52 ($1.35 \times 10^{1} \pm 4.4 \times 10^{0}$ g/m^2/d) samples had the lowest IDRs and the WSU10.4 sample had the highest IDR (1.76×10^{2} g/m^2/d; only a single measurement was possible as the sample lost integrity after the test). This trend in IDR did not match the SDR. The WSU 22 and 52 samples were fabricated with the addition of a SA800 glass binder and the less durable WSU10 and 40 samples contained a NBS4 glass binder. This observation indicates the glass binder used can influence durability.

Glass-bonded sodalite ceramics – The two glass-bonded sodalite ceramics, one with AgI and the other with NaI, had differing IDRs with the AgI form surprisingly having a higher IDR ($2.46 \times 10^{2} \pm 1.30 \times 10^{-2}$ g/m^2/d) compared with the NaI ($1.24 \times 10^{1} \pm 1.9 \times 10^{0}$ g/m^2/d). Both samples had similar SDRs, indicating similar overall matrix durability. This finding would suggest that the iodine form in the glass bonded

ceramics may influence iodine release. It should be noted these porous samples were not corrected for true surface area, only geometric surface area.

Non-Si based matrices – The Pd-V based iodoapatite ceramic measured an IDR of $3.78 \times 10^0 \pm 3.45 \times 10^0$ g/m^2/d while the tellurite glass measured the lowest IDR of all of the tested samples ($9.42 \times 10^{-5} \pm 1.79 \times 10^{-5}$ g/m^2/d). For the Tin Pellet, the IDR was 9.20×10^1 g/m^2/d while the primary matrix component, Sn, gave a normalized tin dissolution rate of 1.30×10^{-2} g/m^2/d. For the Ag-mordenite in GCM samples the DS-60 sample gave this highest IDR of 6.31×10^1 g/m^2/d. The DS-60 also had the highest Bi dissolution rate of 1.06×10^{-2} g/m^2/d. The TJG2010B-55B and TMN-299-71-D samples gave Bi dissolution rates of 8.87×10^{-3} g/m^2/d and 6.76×10^{-3} g/m^2/d, respectively. These Bi dissolution rate values, representing the majority of the sample, were close to the IDR.

In summary, the screening test is successful in comparing durability between IWF samples of the same material class. Indications of influence of the processing conditions on IWF durability are provided by the test. The results can guide which samples can be selected for long-term dynamic leach testing to provide data that can feed a long-term corrosion model. The error ranges between the duplicate tests were fairly consistent; however, some large errors were observed. With the unique nature of many IWF samples, in many cases only a single sample is available and would need to be tested multiple times. A user should be cognizant of sample integrity through multiple sample uses.

Table 3-1. Normalized dissolution rate, with respect to iodine, for the various samples evaluated in the 3-day screening test. Measurements with an associated error were performed with replicates.

IWF Type	Coupon ID	IDR ($g/m^2/d$)	SDR ($g/m^2/d$)
Ag-mordenite (large form)	HIP18-2	$4.70\times10^{-1} \pm 9.36\times10^{-2}$	$6.33\times10^{-1} \pm 1.51\times10^{-1}$
	HIP 18-4	$1.27\times10^{-1} \pm 8.67\times10^{-2}$	$1.27\times10^{-1} \pm 8.67\times10^{-2}$
Ag-mordenite (small form)	HIP17-17	$8.90\times10^{-3} \pm 6.27\times10^{-3}$	$2.13\times10^{-1} \pm 4.53\times10^{-2}$
	HIP 17-22	$5.36\times10^{-2} \pm 3.72\times10^{-2}$	$1.20\times10^{-1} \pm 8.91\times10^{-4}$
	HIP 17-8	1.80×10^{-2}	6.60×10^{-2}
Ag-functionalized silica aerogels	HIP-2	$9.90\times10^{-2} \pm 6.11\times10^{-2}$	$2.21\times10^{-1} \pm 7.44\times10^{-2}$
	SPS-1	$1.34\times10^{-3} \pm 9.44\times10^{-4}$	$3.34\times10^{-1} \pm 2.02\times10^{-1}$
	SPS-2	$1.39\times10^{-3} \pm 1.10\times10^{-3}$	$2.75\times10^{-1} \pm 1.90\times10^{-1}$
HIPed sodalite (U.K.)	H1C6	$1.36\times10^{-3} \pm 7.90\times10^{-5}$	$5.59\times10^{-2} \pm 1.66\times10^{-2}$
	H1C5	$4.49\times10^{-4} \pm 4.65\times10^{-4}$	$9.52\times10^{-2} \pm 3.71\times10^{-2}$
	H1C8	$1.51\times10^{-2} \pm 2.03\times10^{-2}$	$1.65\times10^{-1} \pm 6.06\times10^{-2}$
	H1C9	$8.27\times10^{-2} \pm 1.17\times10^{-1}$	$3.38\times10^{-1} \pm 2.77\times10^{-1}$
	H1C11	$2.19\times10^{-4} \pm 1.98\times10^{-4}$	$1.29\times10^{-1} \pm 8.67\times10^{-2}$
Sintered iodosodalite (WSU)	WSU10.4	1.76×10^{2}	6.79×10^{2}
	WSU22.1	$1.52\times10^{1} \pm 2.00\times10^{1}$	$2.01\times10^{2} \pm 1.60\times10^{2}$
	WSU40	$1.92\times10^{2} \pm 1.41\times10^{2}$	$3.03\times10^{3} \pm 2.24\times10^{3}$
	WSU52	$1.35\times10^{1} \pm 4.43\times10^{0}$	$7.05\times10^{3} \pm 1.59\times10^{3}$
	WSU3	2.95×10^{0}	3.19×10^{0}
	WSU8	2.05×10^{0}	1.86×10^{0}
Glass-bonded sodalite ceramics	AgI	$2.46\times10^{2} \pm 1.30\times10^{2}$	$4.92\times10^{1} \pm 1.07\times10^{1}$
	NaI	$1.24\times10^{1} \pm 1.94\times10^{0}$	$2.52\times10^{1} \pm 9.61\times10^{0}$
Non-Si Based Matrices			
Iodoapatite ceramic	LSU	$3.78\times10^{0} \pm 3.45\times10^{0}$	N/A
Tellurite glass	Te glass	$9.42\times10^{-5} \pm 1.79\times10^{-5}$	N/A
Tin pellet	TJG Tin	9.20×10^{1}	2.29×10^{1}
Ag-mordenite in GCM	DS-60	6.31×10^{1}	1.02×10^{0}
	TJG2010B-55B	2.49×10^{-3}	8.68×10^{-1}
	TMN-200-71-D	1.81×10^{-3}	7.81×10^{-1}

3.2.2 Dynamic Leach Testing

Dynamic leach tests were performed with regular 3-day-interval samplings for total durations between 16 to 22 days. The samplings included a 4-day interval to avoid weekend sampling. This interval selection allows for the screening test to be performed as the initial sampling interval and then consistent intervals to be pulled to assess the corrosion behavior. The consistent intervals align with the approach taken in the recent updates to the ANS Method 16.1 leach test and the ASTM C1308 that is currently under revision.

The resulting IDRs and SDRs from the dynamic leach tests are shown in Figure 3-7 through Figure 3-14 and the corresponding data is listed in Table 3-2. The error bars and minimally fluctuating IDRs and SDRs for the majority of the IWF samples indicate that the release of iodine and the dissolution of the IWF matrix are consistent. Many of the trends observed in the screening test were retained in the dynamic leach test.

Ag-mordenite – The large-form HIP 18-4 sample measured a lower IDR and SDR compared with the HIP 18-2 sample, Figure 3-7. Between the small-form samples, the HIP 17-17 sample had a higher SDR but lower IDR than its HIP 17-22 counterpart. The small-form Ag mordenite samples both measured lower IDR compared with the large-form samples. This trend should be investigated further to ensure the HIP Ag-mordenite durability is not compromised with scaling (or with any IWF type for that matter).

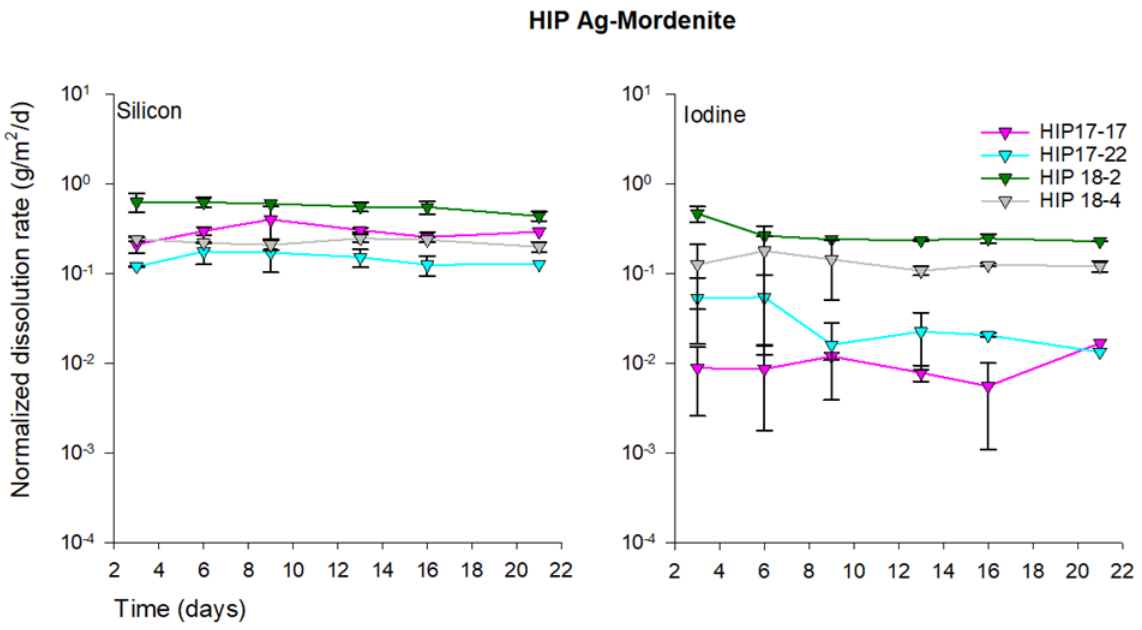

Figure 3-7. The normalized silicon dissolution rate (left) and normalized iodine dissolution rate (IDR) measured through dynamic leach tests of the HIP Ag-mordenite samples.

Silver functionalized silica aerogels – The improvement in iodine retention by SFAs that have been processed via SPS was again highlighted in the dynamic leach test as both the SPS-1 and SPS-2 samples measured far lower IDRs than the HIP-2 sample, Figure 3-8. However, the SDR was similar for the three samples. This would indicate that the matrix is equally susceptible to corrosion, but the higher density of the SPSed samples can protect the iodine that is not exposed at the surface.

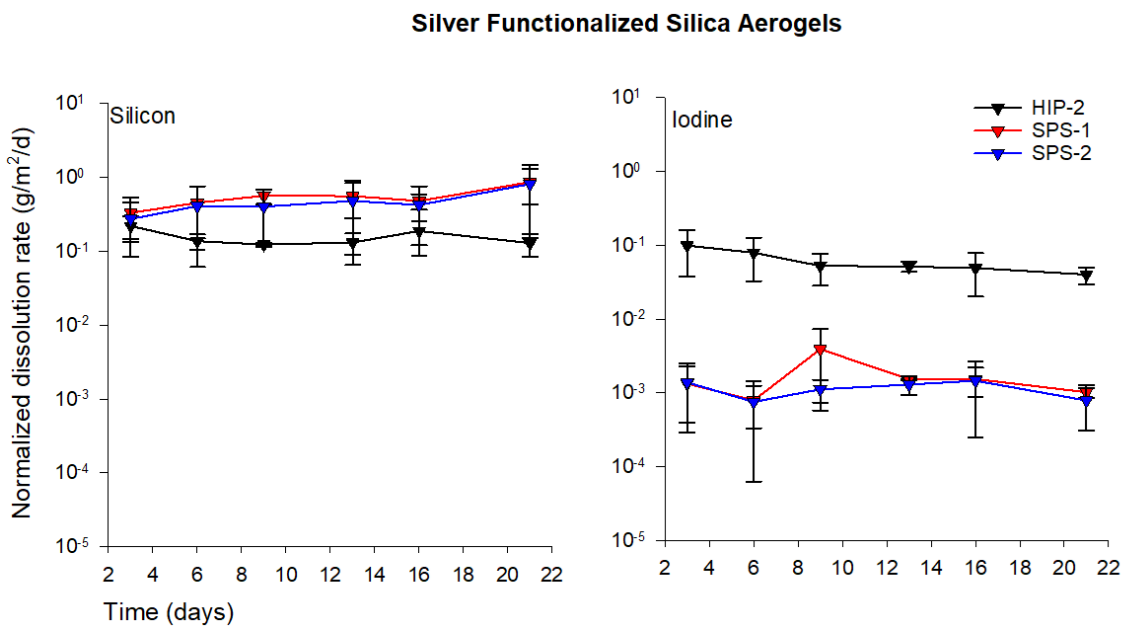

Figure 3-8. The normalized silicon dissolution rate (left) and normalized iodine dissolution rate (IDR) measured through dynamic leach tests of the SFA samples.

HIP iodosodalite – Between the HIP iodosodalite samples, the highest IDR and SDR beyond the first interval were measured for the H1C8 sample as seen in Figure 3-9. The H1C8 sample was fabricated using a zeolite-A starting material with the iodine being occluded into the structure. The most durable were the H1C5 sample, which was an iodine-occluded, commercially available Ionex™ zeolite, and the H1C11 sample, which was hydrothermally synthesized before HIPing. The comparison between the HIP iodosodalite samples suggests that the starting zeolite form may have minor influence over the final sample durability. Two HIP iodosodalite generated through hydrothermal methods (WSU3) and aqueous methods (WSU8) were also tested as seen in Figure 3-10. For both the SDR and the IDR, the aqueous WSU8 was slightly more durable.

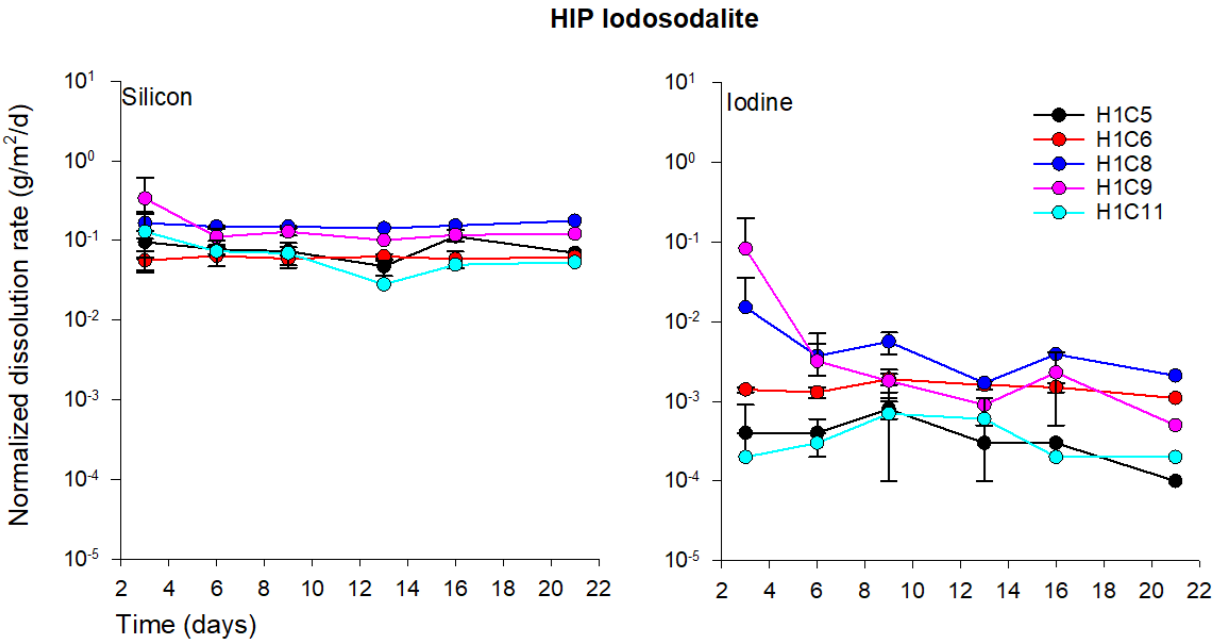

Figure 3-9. The normalized silicon dissolution rate (left) and normalized iodine dissolution rate (IDR) measured through dynamic leach tests of the HIP Iodosodalite samples produced at University of Birmingham.

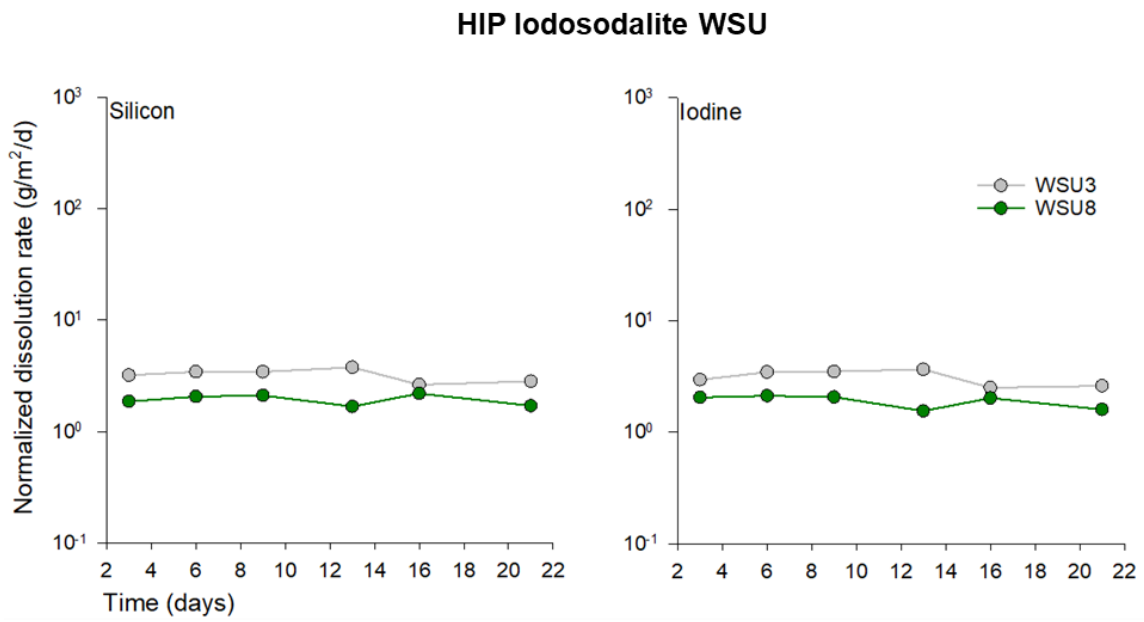

Figure 3-10. The normalized silicon dissolution rate (left) and normalized iodine dissolution rate (IDR) measured through dynamic leach tests of the HIP iodosodalite samples produced at WSU.

Sintered Iodosodalites – Out of the sintered iodosodalite samples, Figure 3-11, the WSU52 displayed the highest IDR and the WSU22 and WSU40 had the lowest IDR. The WSU22 sample also had the lowest SDR, while the other three samples had near-identical SDRs. The use of the SA800 binder and a hydrothermally generated iodosodalite appears to improve iodine retention and overall matrix durability.

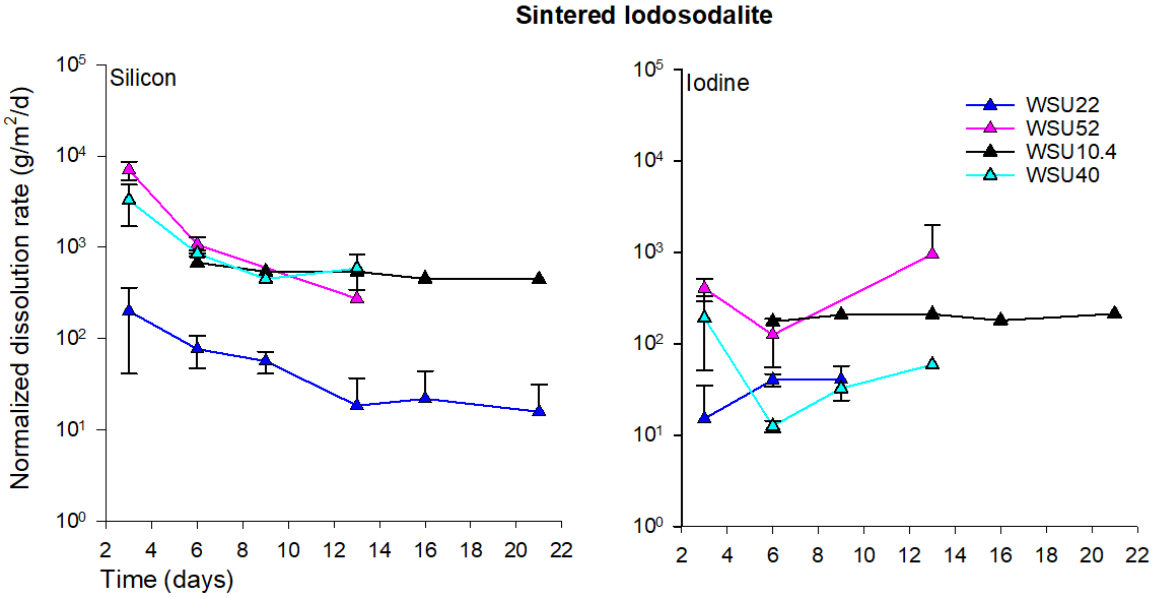

Figure 3-11. The normalized silicon dissolution rate (left) and normalized iodine dissolution rate (IDR) measured through dynamic leach tests of the sintered iodosodalite samples.

Glass-bonded sodalite ceramics – Between the two glass-bonded sodalite ceramics the NaI form again measured lower IDR and SDR as shown in Figure 3-12. This result is surprising as the solubility of AgI is much lower than NaI, yet the IDR is higher for the AgI form. The true surface area should be accounted for in future studies.

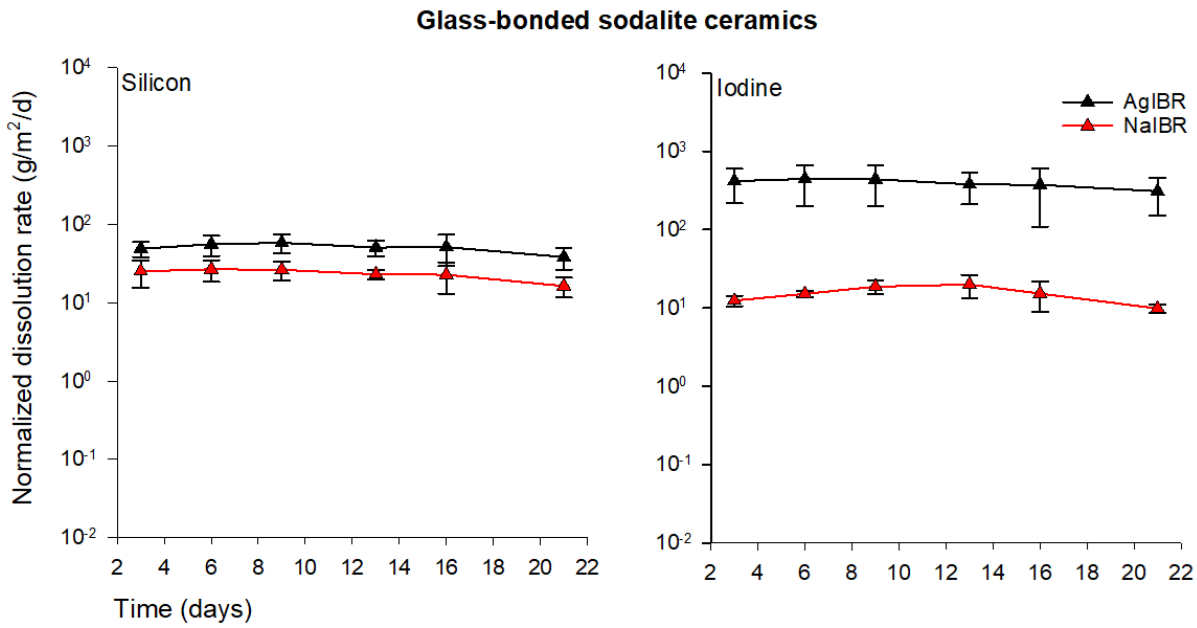

Figure 3-12. The normalized silicon dissolution rate (left) and normalized iodine dissolution rate (IDR) measured through dynamic leach tests of the glass-bonded sodalite ceramics.

Glass composite material – Out of the four glass composite materials, Figure 3-13, the lowest IDR was measured for the TJG2010B-55B sample with the TMN-299-71-D sample measuring a comparable IDR. All the samples had similar SDRs, which indicates an improved iodine retention mechanism in the TJG and TMN mordenite samples. The TJG tin sample had the highest SDR, however the majority of this samples was not Si and the TJG tin sample did not have measurable Sn in the leachate after the first interval. The Bi dissolution rates of DS-60, TJG2010B-55B and TMN-299-71-D were comparable to the IDR. The influence of the GCM shell on the corrosion of the core has yet to be determined.

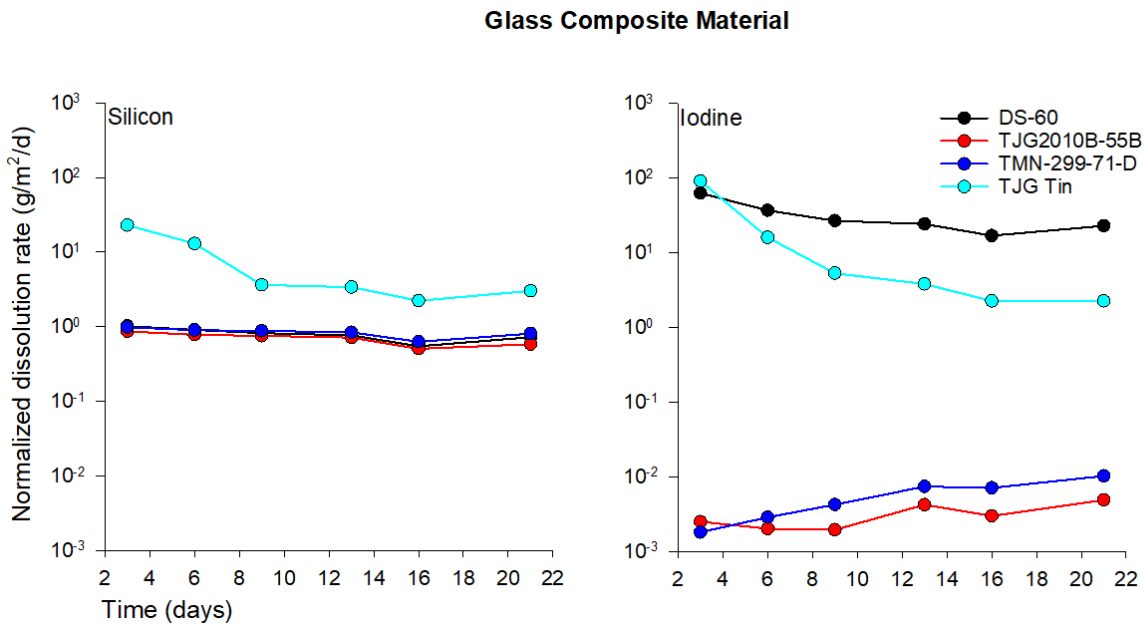

Figure 3-13. The normalized silicon dissolution rate (left) and normalized iodine dissolution rate (IDR) measured through dynamic leach tests of the Glass Composite material samples

Non-silicon-based materials – The Pb-V iodoapatite had a decreasing IDR with time, which could suggest that the iodine initially on the surface is available to leach but as time progresses the matrix protects exposing additional iodine. The tellurium glass again measured the lowest IDR by several orders of magnitude. The tellurium glasses should be investigated further due to this enhanced durability.

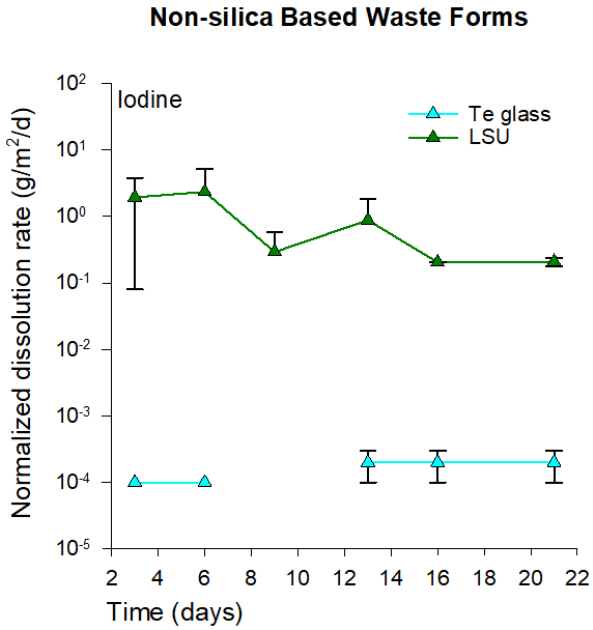

Figure 3-14. The normalized iodine dissolution rate (IDR) measured through dynamic leach tests of the two IWF that were not silicon based.

To summarize, the results of the dynamic leach tests corroborate, for the most part, the findings in the screening test. Many of the IWF types had consistent corrosion behavior and no clear trend was observed between the measured rate and the re-use of the sample (e.g., the iodoapatite sample increased in IDR on repeat runs while the Ag-mordenite was lower). Therefore, we believe it is suitable to re-use unique samples with re-polishing to gain replicate runs. When comparing the SDRs of the most durable of each IWF type, it is evident that the matrix of the silica-based waste forms is as stable as a representative nuclear waste glass SON68 and most fall between 10^{-1} and 10^{0} g/m^2/d as shown in Figure 3-15. However, the decreased IDRs of some IWF types (e.g., Te glass, SPS SFA) indicate that increased iodine retention is feasible. An assessment in a long-term dissolution model should be performed to explore the overall impact of the measured dissolution rates on radionuclide release upon disposal.

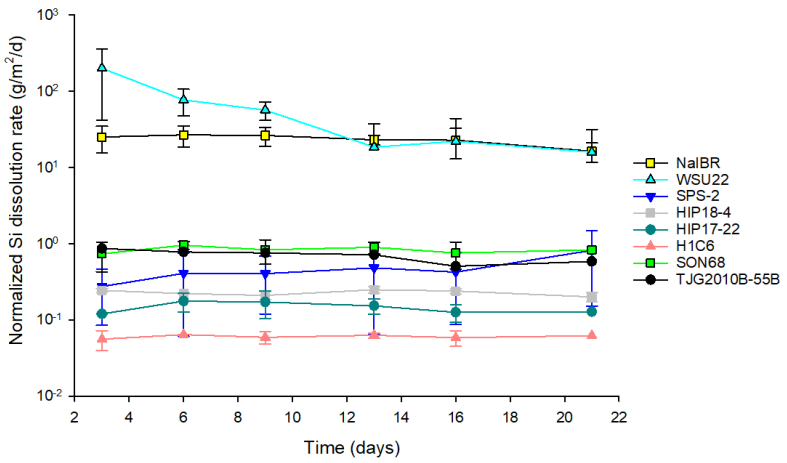

Figure 3-15. Comparison of the normalized silicon dissolution rates over time from the extended C1220 tests.

Table 3-2. Summary of the average IDRs and SDRs measured in the dynamic leach tests. Samples without an associated error only had a single viable measurement at that interval.

Coupon ID	Rate	Sampling Time (d)					
		3	6	9	12	15	21
		Normalized Dissolution Rate ($g/m^2/d$)					
HIP Ag-mordenite							
HIP18-2	IDR	$4.70\times10^{-1} \pm 9.36\times10^{-2}$	$2.67\times10^{-1} \pm 1.19\times10^{-4}$	2.43×10^{-1}	$2.38\times10^{-1} \pm 4.18\times10^{-3}$	$2.49\times10^{-1} \pm 2.84\times10^{-2}$	$2.32\times10^{-1} \pm 5.98\times10^{-4}$
	SDR	$6.33\times10^{-1} \pm 1.51\times10^{-1}$	$6.28\times10^{-1} \pm 7.76\times10^{-2}$	6.05×10^{-1}	$5.60\times10^{-1} \pm 6.76\times10^{-2}$	$5.55\times10^{-1} \pm 9.27\times10^{-2}$	$4.41\times10^{-1} \pm 5.17\times10^{-2}$
HIP 18-4	IDR	1.27×10-1± 8.67×10^{-2}	1.80×10-1± 1.64×10^{-1}	1.45×10-1± 9.36×10^{-2}	$1.08\times10^{-1} \pm 1.25\times10^{-2}$	$1.25\times10^{-1} \pm 5.07\times10^{-3}$	$1.22\times10^{-1} \pm 1.62\times10^{-2}$
	SDR	1.27×10-1± 8.67×10^{-2}	2.22×10-1± 1.43×10^{-3}	2.10×10-1± 2.72×10^{-2}	2.49×10-1±2.51×10^{-2}	$2.39\times10^{-1} \pm 1.69\times10^{-2}$	$2.00\times10^{-1} \pm 2.74\times10^{-2}$
HIP17-17	IDR	$8.90\times10^{-3} \pm 6.27\times10^{-3}$	$8.67\times10^{-3} \pm 6.86\times10^{-3}$	$1.20\times10^{-2} \pm 1.15\times10^{-3}$	$7.90\times10^{-3} \pm 1.61\times10^{-3}$	$5.59\times10^{-3} \pm 4.51\times10^{-3}$	1.68×10^{-2}
	SDR	$2.13\times10^{-1} \pm 4.53\times10^{-2}$	$3.00\times10^{-1} \pm 3.01\times10^{-2}$	$4.03\times10^{-1} \pm 1.59\times10^{-1}$	$3.07\times10^{-1} \pm 1.88\times10^{-2}$	$2.58\times10^{-1} \pm 3.03\times10^{-2}$	2.94×10^{-1}
HIP 17-22	IDR	$5.36\times10^{-2} \pm 3.72\times10^{-2}$	$5.47\times10^{-2} \pm 4.22\times10^{-2}$	$1.62\times10^{-2} \pm 1.23\times10^{-2}$	$2.27\times10^{-2} \pm 1.42\times10^{-2}$	$2.07\times10^{-2} \pm 1.10\times10^{-3}$	1.34×10^{-2}
	SDR	$1.20\times10^{-1} \pm 8.91\times10^{-4}$	$1.77\times10^{-1} \pm 5.02\times10^{-2}$	$1.72\times10^{-1} \pm 6.85\times10^{-2}$	$1.53\times10^{-1} \pm 3.39\times10^{-2}$	$1.25\times10^{-1} \pm 3.25\times10^{-2}$	1.28×10^{-1}
Silver functionalized silica aerogels							
HIP-2	IDR	$9.90\times10^{-2} \pm 6.11\times10^{-2}$	$7.92\times10^{-2} \pm 4.66\times10^{-2}$	$5.26\times10^{-2} \pm 2.45\times10^{-2}$	$5.13\times10^{-2} \pm 8.01\times10^{-3}$	$4.91\times10^{-2} \pm 2.90\times10^{-2}$	$4.00\times10^{-2} \pm 1.01\times10^{-2}$
	SDR	$2.21\times10^{-1} \pm 7.44\times10^{-2}$	$1.37\times10^{-1} \pm 3.20\times10^{-2}$	$1.23\times10^{-1} \pm 8.10\times10^{-3}$	$1.32\times10^{-1} \pm 4.21\times10^{-2}$	$1.89\times10^{-1} \pm 6.87\times10^{-2}$	$1.29\times10^{-1} \pm 4.36\times10^{-2}$
SPS-1	IDR	$1.34\times10^{-3} \pm 9.44\times10^{-4}$	$7.89\times10^{-4} \pm 4.55\times10^{-4}$	$3.92\times10^{-3} \pm 3.34\times10^{-3}$	$1.53\times10^{-3} \pm 2.66\times10^{-5}$	$1.54\times10^{-3} \pm 6.53\times10^{-4}$	$1.02\times10^{-3} \pm 1.56\times10^{-4}$
	SDR	$3.34\times10^{-1} \pm 2.02\times10^{-1}$	$4.57\times10^{-1} \pm 3.08\times10^{-1}$	$5.65\times10^{-1} \pm 1.29\times10^{-1}$	$5.61\times10^{-1} \pm 2.80\times10^{-1}$	$4.81\times10^{-1} \pm 1.16\times10^{-1}$	$8.67\times10^{-1} \pm 4.37\times10^{-1}$
SPS-2	IDR	$1.39\times10^{-3} \pm 1.10\times10^{-3}$	$7.54\times10^{-4} \pm 6.91\times10^{-4}$	$1.12\times10^{-3} \pm 3.82\times10^{-4}$	$1.30\times10^{-3} \pm 3.64\times10^{-4}$	$1.46\times10^{-3} \pm 1.21\times10^{-3}$	$7.88\times10^{-4} \pm 4.82\times10^{-4}$
	SDR	$2.75\times10^{-1} \pm 1.90\times10^{-1}$	$4.10\times10^{-1} \pm 3.49\times10^{-1}$	$4.05\times10^{-1} \pm 2.85\times10^{-1}$	$4.83\times10^{-1} \pm 4.18\times10^{-1}$	$4.25\times10^{-1} \pm 3.38\times10^{-1}$	$8.20\times10^{-1} \pm 6.68\times10^{-1}$
HIP iodosodalite							
H1C6	IDR	$1.36\times10^{-3} \pm 7.90\times10^{-5}$	$1.26\times10^{-3} \pm 1.56\times10^{-4}$	$1.93\times10^{-3} \pm 2.85\times10^{-4}$	$1.58\times10^{-3} \pm 2.47\times10^{-4}$	$1.48\times10^{-3} \pm 2.31\times10^{-4}$	1.11×10^{-3}
	SDR	$5.59\times10^{-2} \pm 1.66\times10^{-2}$	$6.42\times10^{-2} \pm 1.48\times10^{-4}$	$5.91\times10^{-2} \pm 1.06\times10^{-2}$	$6.29\times10^{-2} \pm 4.81\times10^{-3}$	$5.86\times10^{-2} \pm 1.36\times10^{-2}$	6.22×10^{-2}
H1C5	IDR	$4.49\times10^{-4} \pm 4.65\times10^{-4}$	$4.17\times10^{-4} \pm 1.66\times10^{-4}$	$7.80\times10^{-4} \pm 1.86\times10^{-4}$	$3.48\times10^{-4} \pm 2.19\times10^{-4}$	2.99×10^{-4}	1.50×10^{-4}
	SDR	$9.52\times10^{-2} \pm 3.71\times10^{-2}$	$7.74\times10^{-2} \pm 1.01\times10^{-2}$	$7.32\times10^{-2} \pm 8.86\times10^{-3}$	$4.73\times10^{-2} \pm 1.12\times10^{-2}$	1.13×10^{-1}	6.96×10^{-2}
H1C8	IDR	$1.51\times10^{-2} \pm 2.03\times10^{-2}$	$3.70\times10^{-3} \pm 1.56\times10^{-3}$	$5.62\times10^{-3} \pm 1.72\times10^{-3}$	1.68×10^{-3}	3.88×10^{-3}	2.06×10^{-3}
	SDR	$1.65\times10^{-1} \pm 6.06\times10^{-2}$	$1.49\times10^{-1} \pm 3.38\times10^{-3}$	$1.49\times10^{-1} \pm 4.60\times10^{-3}$	1.42×10^{-1}	1.54×10^{-1}	1.76×10^{-1}
H1C9	IDR	$8.27\times10^{-2} \pm 1.17\times10^{-1}$	$3.19\times10^{-3} \pm 3.92\times10^{-3}$	$1.76\times10^{-3} \pm 6.57\times10^{-4}$	8.74×10^{-4}	$2.26\times10^{-3} \pm 1.81\times10^{-3}$	5.20×10^{-4}
	SDR	$3.38\times10^{-1} \pm 2.77\times10^{-1}$	$1.11\times10^{-1} \pm 2.84\times10^{-2}$	$1.29\times10^{-1} \pm 1.29\times10^{-2}$	1.01×10^{-1}	$1.17\times10^{-1} \pm 1.91\times10^{-2}$	1.21×10^{-1}
H1C11	IDR	$2.19\times10^{-4} \pm 1.98\times10^{-4}$	$3.12\times10^{-4} \pm 6.95\times10^{-5}$	$7.33\times10^{-4} \pm 5.54\times10^{-4}$	$5.68\times10^{-4} \pm 5.31\times10^{-4}$	1.66×10^{-4}	1.63×10^{-4}
	SDR	$1.29\times10^{-1} \pm 8.67\times10^{-2}$	$7.31\times10^{-2} \pm 2.58\times10^{-2}$	$6.89\times10^{-2} \pm 2.40\times10^{-2}$	$2.81\times10^{-2} \pm 2.81\times10^{-2}$	4.95×10^{-2}	5.33×10^{-2}
Sintered iodosodalite							
WSU10	IDR	1.76×10^{2}	2.08×10^{2}	2.11×10^{2}	1.80×10^{2}	2.13×10^{2}	NM
	SDR	6.79×10^{2}	5.44×10^{2}	5.41×10^{2}	4.54×10^{2}	4.47×10^{2}	NM
WSU22.1	IDR	$1.52\times10^{1} \pm 2.00\times10^{1}$	$4.04\times10^{1} \pm 6.27\times10^{0}$	$4.07\times10^{1} \pm 1.67\times10^{1}$	ND	ND	ND
	SDR	$2.01\times10^{2} \pm 1.60\times10^{2}$	$7.71\times10^{1} \pm 2.96\times10^{1}$	$5.70\times10^{1} \pm 1.54\times10^{1}$	$1.86\times10^{1} \pm 1.86\times10^{1}$	$2.21\times10^{1} \pm 2.21\times10^{1}$	$1.59\times10^{1} \pm 1.59\times10^{1}$
WSU40	IDR	N/A	$1.26\times10^{1} \pm 1.83\times10^{0}$	3.25×10^{1}	5.93×10^{1}	N/A	N/A
	SDR	$3.29\times10^{3} \pm 1.59\times10^{3}$	$8.60\times10^{2} \pm 6.59\times10^{1}$	4.52×10^{2}	$5.91\times10^{2} \pm 2.45\times10^{2}$	N/A	N/A
WSU52	IDR	$1.35\times10^{1} \pm 4.43\times10^{0}$	$3.29\times10^{0} \pm 2.05\times10^{0}$	ND	$3.75\times10^{1} \pm 5.31\times10^{1}$	ND	ND
	SDR	$7.05\times10^{3} \pm 1.59\times10^{3}$	$1.07\times10^{3} \pm 2.21\times10^{2}$	ND	$2.74\times10^{2} \pm 2.74\times10^{2}$	ND	ND

Coupon ID	Rate	Sampling Time (d)					
		3	6	9	12	15	21
		Normalized Dissolution Rate ($g/m^2/d$)					
HIP iodosodalite							
WSU8	IDR	2.05×10^{0}	2.12×10^{0}	2.07×10^{0}	1.55×10^{0}	2.03×10^{0}	1.60×10^{0}
	SDR	1.86×10^{0}	2.05×10^{0}	2.11×10^{0}	1.67×10^{0}	2.19×10^{0}	1.70×10^{0}
WSU3	IDR	2.95×10^{0}	3.47×10^{0}	3.51×10^{0}	3.66×10^{0}	2.51×10^{0}	2.60×10^{0}
	SDR	3.19×10^{0}	3.43×10^{0}	3.43×10^{0}	3.76×10^{0}	$2.63\times10^{+00}$	2.82×10^{0}
Glass-bonded sodalite ceramics							
AgI	IDR	$2.46\times10^{2} \pm 1.30\times10^{2}$	$2.66\times10^{2} \pm 1.60\times10^{2}$	$2.62\times10^{2} \pm 1.59\times10^{2}$	$2.20\times10^{2} \pm 1.09\times10^{2}$	$2.16\times10^{2} \pm 1.65\times10^{2}$	$1.74\times10^{2} \pm 9.74\times10^{1}$
	SDR	$4.92\times10^{1} \pm 1.07\times10^{1}$	$5.60\times10^{1} \pm 1.63\times10^{1}$	$5.86\times10^{1} \pm 1.61\times10^{1}$	$5.09\times10^{1} \pm 1.22\times10^{1}$	$5.17\times10^{1} \pm 2.25\times10^{1}$	$3.85\times10^{+1} \pm 1.18\times10^{1}$
NaI	IDR	$1.24\times10^{1} \pm 1.94\times10^{0}$	$1.52\times10^{1} \pm 1.51\times10^{0}$	$1.87\times10^{1} \pm 3.58\times10^{0}$	$2.00\times10^{1} \pm 6.67\times10^{0}$	$1.53\times10^{1} \pm 6.46\times10^{0}$	$9.89\times10^{0} \pm 1.26\times10^{0}$
	SDR	$2.52\times10^{1} \pm 9.61\times10^{0}$	$2.68\times10^{1} \pm 8.18\times10^{0}$	$2.64\times10^{1} \pm 7.37\times10^{0}$	$2.32\times10^{1} \pm 3.14\times10^{0}$	$2.29\times10^{1} \pm 9.86\times10^{0}$	$1.64\times10^{1} \pm 4.73\times10^{0}$
Glass composite material							
DS-60	IDR	6.31×10^{1}	3.70×10^{1}	2.70×10^{1}	2.44×10^{1}	1.70×10^{1}	2.31×10^{1}
	SDR	1.02×10^{0}	9.08×10^{-1}	8.21×10^{-1}	7.68×10^{-1}	5.49×10^{-1}	7.26×10^{-1}
	Bismuth Dissolution Rate	$1.06\text{x}10^{-2}$	$1.95\text{x}10^{-2}$	$9.25\text{x}10^{-3}$	$9.28\text{x}10^{-3}$	$8.57\text{x}10^{-3}$	$1.17\text{x}10^{-2}$
TJG2010B-55B	IDR	2.49×10^{-3}	2.01×10^{-3}	1.95×10^{-3}	4.21×10^{-3}	2.99×10^{-3}	4.89×10^{-3}
	SDR	8.68×10^{-1}	7.81×10^{-1}	7.58×10^{-1}	7.16×10^{-1}	5.08×10^{-1}	5.85×10^{-1}
	Bismuth Dissolution Rate	$8.87\text{x}10^{-3}$	$1.26\text{x}10^{-2}$	$3.08\text{x}10^{-2}$	$4.46\text{x}10^{-2}$	$1.52\text{x}10^{-2}$	$1.34\text{x}10^{-2}$
TMN-299-71-D	IDR	1.81×10^{-3}	2.87×10^{-3}	4.24×10^{-3}	7.39×10^{-3}	7.11×10^{-3}	1.02×10^{-2}
	SDR	9.90×10^{-1}	9.02×10^{-1}	8.79×10^{-1}	8.42×10^{-1}	6.30×10^{-1}	8.10×10^{-1}
	Bismuth Dissolution Rate	$6.76\text{x}10^{-3}$	$9.89\text{x}10^{-3}$	$7.33\text{x}10^{-3}$	$1.08\text{x}10^{-2}$	$8.41\text{x}10^{-3}$	$1.10\text{x}10^{-2}$
TJG Tin	IDR	9.20×10^{1}	1.61×10^{1}	5.33×10^{0}	3.83×10^{0}	2.27×10^{0}	2.26×10^{0}
	SDR	2.29×10^{1}	1.30×10^{1}	3.64×10^{0}	3.40×10^{0}	2.23×10^{0}	3.03×10^{0}
Non-Si-based waste forms							
Te glass	IDR	$9.42\times10^{-5} \pm 1.79\times10^{-5}$	$8.76\times10^{-5} \pm 3.09\times10^{-5}$	3.98×10^{-5}	$2.04\times10^{-4} \pm 1.38\times10^{-4}$	$1.94\times10^{-4} \pm 9.52\times10^{-5}$	$2.05\times10^{-4} \pm 1.07\times10^{-4}$
	SDR	N/A	N/A	N/A	N/A	N/A	N/A
LSU	IDR	$1.94\times10^{0} \pm 1.86\times10^{0}$	$2.34\times10^{0} \pm 2.82\times10^{0}$	2.92×10^{-1}	$8.78\times10^{-1} \pm 9.45\times10^{-1}$	$2.05\times10^{-1} \pm 2.90\times10^{-3}$	$2.09\times10^{-1} \pm 3.18\times10^{-2}$
	SDR	N/A	N/A	N/A	N/A	N/A	N/A

NM = not measured; ND = non-detect (results were below instrument detection limits)

3.3 Conceptual Model Variable Testing

3.3.1 Common Ion Effect

The dissolution of the IWF matrix can result in two outcomes: 1) a larger amount of the iodine in the waste form being exposed to the environment and being subsequently released and/or 2) an increase in the concentration of the dissolved components from the matrix in solution. As the concentration of the dissolved matrix components increases, the dissolution rate of the matrix would slow due to a common ion effect as the difference in chemical potential between the matrix and dissolved components decreases (Pierce et al 2008). In a mechanistic model, the dissolution of the matrix may need to be represented in evolving near-field conditions in an approach similar to the application of the affinity term used in the transition state theory model for glass corrosion. In an initial attempt to assess this behavior, a modified leach test was performed in FY19 on the large-form Ag-mordenite HIP 18-3 sample in which the solution was not exchanged after each sampling. The normalized IDR for the HIP 18-3 sample was calculated by the change in iodine concentration between each interval. The concentration of silicon in solution was monitored as well and the results are presented in Figure 3-16. In the static test, the normalized iodine dissolution rate decreased with increasing time, corresponding to an accumulation of silicon in the reactor. The overall normalized dissolution rate at 15 days in the static test was 0.008 g/m^2/d, which was 50 × lower than the normalized iodine dissolution rate measured in the dynamic leach test, ~0.40 g/m^2/d.

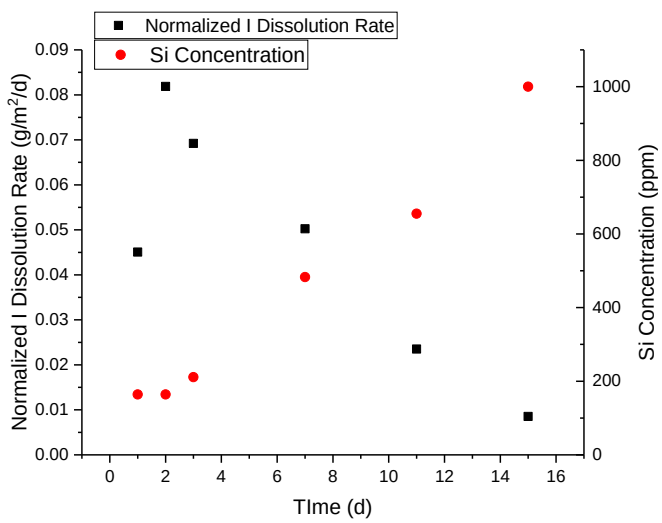

Figure 3-16. The IDR measured for the HIP 18-3 samples in a dynamic leach test where the leachate was not replaced at each interval and a subsample was collected from the leachate at each interval instead. The corresponding Si concentration within the leachate is also displayed.

Based on this result, tests were performed in FY20 where the leachant used had a nominal concentration of Si added (target: 15 ppm and 45 ppm) to assess the influence on the IDR (Figure 3-17 to Figure 3-19). For the standard dynamic leach tests Si concentration in the reactor at each interval is measured between 0.2 ppm and 1 ppm. Across the three samples, a trend of decreasing IDR with increasing Si difference (the difference between the nominal Si in the leachant and the measured Si in the leachate) was observed. The Si concentration in the fresh leachate added at each interval was constant from measuring blank samples. The initial sampling on the HIP 18-3 sample was the only outlier as shown in Figure 3-18. However, the overall IDR measured in the Si-addition tests was not significantly different than the IDR measured in the standard dynamic leach test in DI (~0.2 g/m^2/d). It is likely that the static tests reach Si concentrations above the common ion effect limit early in the 3-day leach intervals and are thus not dilute at the conditions used. Further investigation is required to assess the common ion effect on IWF and SPFT is proposed for such an evaluation as it can obtain consistent dilute conditions within the reaction vessel.

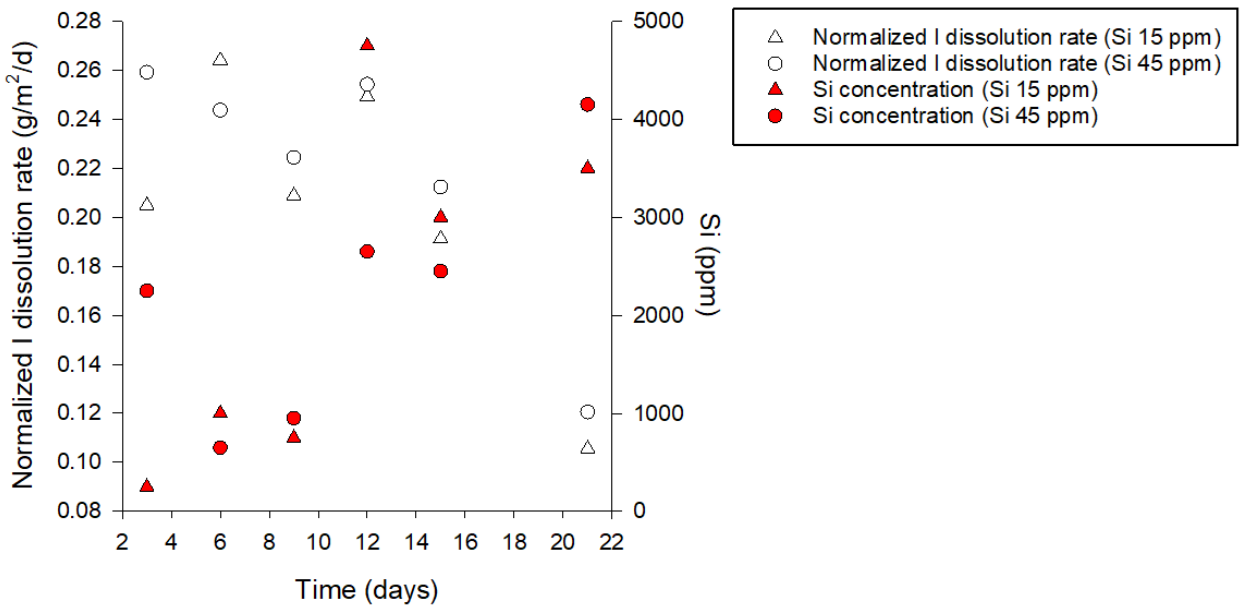

Figure 3-17. The IDR (white) and resulting Si concentration from sample dissolution (red, calculated as the difference between the nominal Si concentration added to the leachant the measure Si in the leachate) measured during static tests with added Si to the leachant using the large-form Ag-mordenite samples HIP 18-2-1 (triangle) and HIP 18-2-2 (circle).

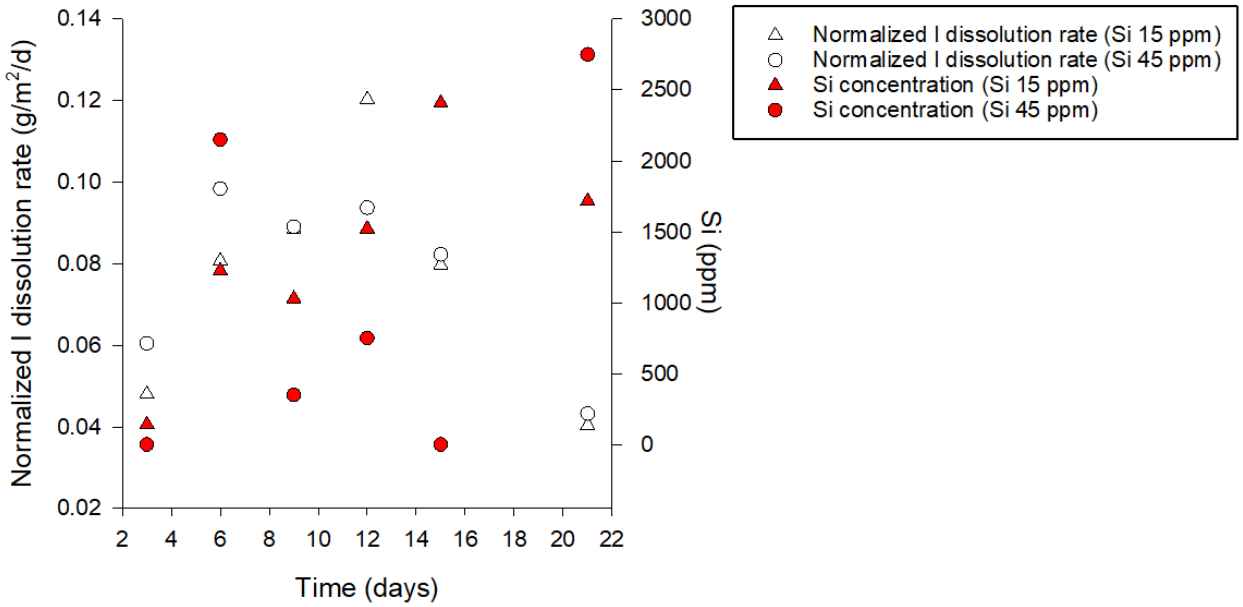

Figure 3-18. The IDR (white) and Si concentration from sample dissolution (red, calculated as the difference between the nominal Si concentration added to the leachant the measure Si in the leachate) measured during static tests with added Si to the leachant using the large-form Ag-mordenite samples HIP 18-3-1 (triangle) and HIP 18-3-2 (circle).

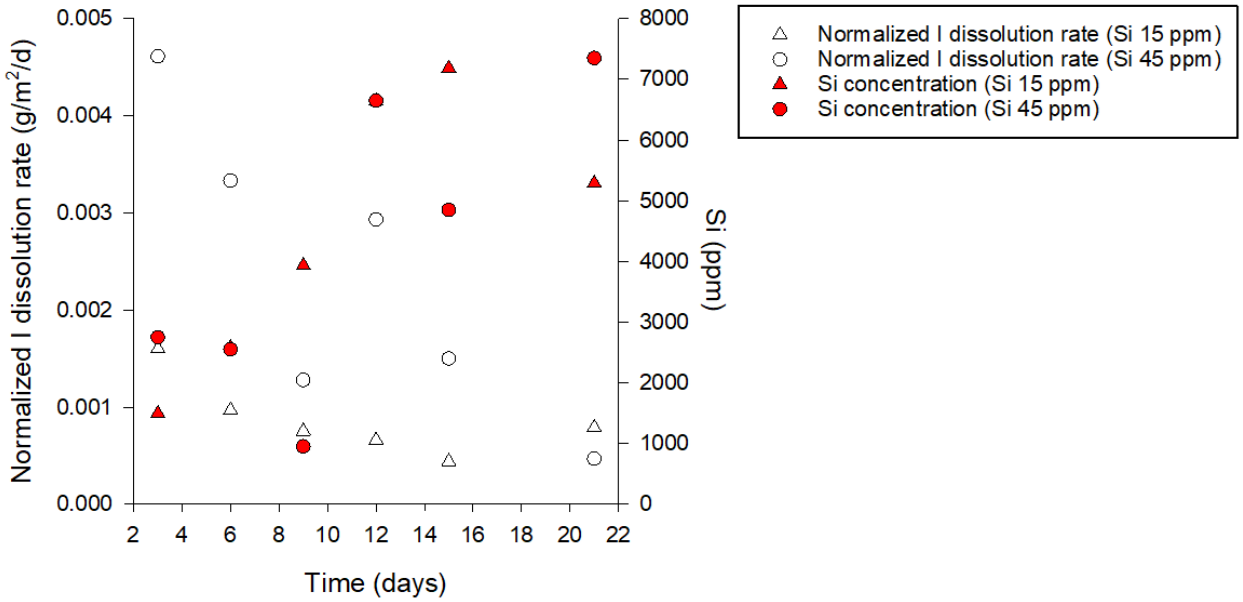

Figure 3-19. The IDR (white) and Si concentration from sample dissolution (red, calculated as the difference between the nominal Si concentration added to the leachant the measure Si in the leachate) measured during static tests with added Si to the leachant using the Silver Functionalized Silica Aerogels SPS-3 (triangle) and SPS-4 (circle).

3.3.2 Temperature

Understanding the influence of temperature on waste form dissolution is essential for long-term model development to ensure extrapolations can be made from the accelerated test temperatures commonly used to the evolving temperature within a repository over time. The screening and dynamic leach tests studied for IWF are performed at 90 °C to ensure measurements can be made in a timely fashion. Additional screening test data was collected at varying temperatures to evaluate both the ability of the static leach test to garner data at lower temperatures and an Arrhenius relationship between the rates and temperature. Table 3-3 shows the resulting IDRs and SDRs for samples tested at multiple temperatures. The expected behavior was observed, with lower rates being measured at lower temperatures. In the tests at room temperature, no measurable iodine was observed in solution; however, the silicon concentrations were measurable for all the room temperature tests for the small-form Ag-mordenite samples. Using this data, a plot of the SDR vs. inverse test temperature (in K) was generated, Figure 3-20. The plot suggests a strong Arrhenius relationship between the matrix dissolution rate and test temperature, the implication being that an activation energy term should be added to any long-term dissolution model.

Table 3-3. Comparison of the normalized dissolution rates with respect to I, Al, Si, and Ag for samples tested at multiple temperatures in a 1-day interval.

Coupon ID	Temperature (°C)	Normalized Dissolution Rate ($g/m^2/d$)			
		I	Al	Si	Ag
HIP 17-8	23	NM	ND	2.32×10^{-2}	ND
	40	3.14×10^{-1}	ND	1.72×10^{-1}	ND
	90	5.36×10^{-1}	5.71×10^{-2}	8.09×10^{-1}	ND
HIP 17-17	23	NM	ND	8.74×10^{-2}	ND
	40	5.39×10^{-2}	ND	2.35×10^{-1}	ND
	90	1.45×10^{1}	4.71×10^{-2}	1.27×10^{0}	ND
HIP 17-22	23	NM	ND	4.21×10^{-2}	ND
	40	1.03×10^{-1}	ND	3.14×10^{-1}	ND
	90	1.23×10^{0}	ND	5.84×10^{-1}	ND
SON68	23	NM	ND	ND	ND
	40	ND	ND	1.50×10^{-1}	ND
	90	ND	ND	3.22×10^{-1}	1.60×10^{-3}
HIP 17-6	40	2.32×10^{-1}	ND	2.35×10^{-1}	ND
	90	4.05×10^{1}	ND	3.78×10^{-1}	ND
HIP 17-2	70	5.80×10^{-3}	ND	5.95×10^{-1}	ND
	90	5.81×10^{-1}	8.49×10^{-2}	5.76×10^{-1}	ND
HIP 17-18	70	1.11×10^{-2}	ND	3.28×10^{0}	ND
	90	2.83×10^{-1}	2.93×10^{-1}	4.01×10^{0}	ND
NM = not measured; ND = non-detect (below instrument detection limits)					

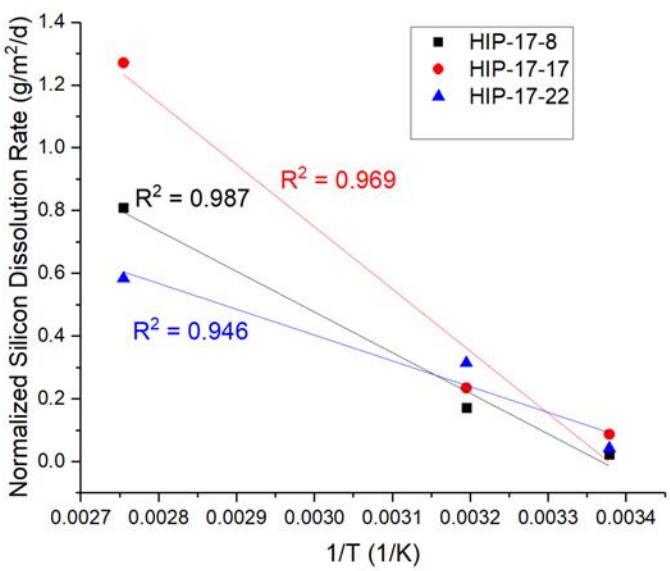

Figure 3-20. Plot showing the normalized silicon dissolution rate from a single 1-day interval vs. the inverse test temperature. The R^2 values correspond to the specific samples analyzed.

3.3.3 Comparison of Sample Surface Area : Solution (SA/V) Ratio

With the observation in Section 3.3.1 that the common ion effect influences the dissolution rate of the silica-based IWF through solution feedback and could lead to dissolution rates measured being underestimated. To assess whether the sample surface area : leachant volume (SA/V) ratios used in the initial leach tests would be influenced by changing the dilution within the reactor, a set of leach tests were carried out at

differing SA/V ratios. The measured IDRs and SDRs from the initial screening test interval of the two SA/V ratios used are presented in Table 3-4.

Table 3-4. Normalized dissolution rates for I and Si at the 3-day sampling interval with variable SA/V volume ratios.

Sample ID	SA/V (cm^{-1})	IDR ($g/m^2/d$)	SDR ($g/m^2/d$)
HIP 18 2	0.01 ± 0.00	$4.7\times10^{-1} \pm 9.4\times10^{-2}$	$6.3\times10^{-1} \pm 1.5\times10^{-1}$
	0.09	1.4×10^{-1}	2.3×10^{-1}
HIP 18 4	0.01 ± 0.00	$1.3\times10^{-1} \pm 8.7\times10^{-2}$	$2.4\times10^{-1} \pm 1.54\times10^{-2}$
	0.09	2.2×10^{-2}	1.0×10^{-1}
SPS-2	0.11 ± 0.01	$1.4\times10^{-3} \pm 1.1\times10^{-3}$	$2.7\times10^{-1} \pm 1.9\times10^{-1}$
	0.29	1.0×10^{-3}	2.2×10^{-1}
Aero HIP 2	0.12 ± 0.03	$9.9\times10^{-2} \pm 6.1\times10^{-2}$	$2.2\times10^{-1} \pm 7.4\times10^{-2}$
	0.80	1.8×10^{-3}	1.3×10^{-1}
H1C5	0.28 ± 0.06	$4.5\times10^{-4} \pm 4.7\times10^{-4}$	$9.5\times10^{-2} \pm 3.7\times10^{-2}$
	0.09	1.1×10^{-3}	9.8×10^{-2}
H1C8	0.21 ± 0.04	$1.5\times10^{-2} \pm 2.0\times10^{-2}$	$1.7\times10^{-1} \pm 6.1\times10^{-2}$
	0.09	1.7×10^{-2}	1.4×10^{-1}
H1C9	0.26 ± 0.04	$8.3\times10^{-2} \pm 1.2\times10^{-1}$	$3.4\times10^{-1} \pm 2.8\times10^{-1}$
	0.09	2.0×10^{-3}	1.0×10^{-1}

Very little change in the measured IDR and SDR was observed between the tests with varying SA/V ratios, in most cases < 3×. This observation indicates that the larger SA/V ratios used, and the more concentrated test conditions that result, are sufficiently similar to the smaller SA/V tests despite differences in Si concentration, which aligns with the observation in Section 3.3.1. Much larger deviations upon dilution would be expected if the common ion effect were controlling the dissolution mechanism of the IWF at these conditions. Therefore, it is suggested to use a SA/V ratio of 1:10 cm^2/mL where possible and where sample geometry allows to increase the likelihood of measurable dissolved constituents being present in the leachate.

3.4 Microstructure Analysis

3.4.1 SEM of "After" Samples

One of the advantages of the leach test using monolithic samples is that the sample can be analyzed following leach intervals or at the conclusion of the test to observe any microstructural changes. It is important to couple this microstructural information with the measured dissolution rates to understand the controlling mechanism of the IWF corrosion and ensure that mechanism is sufficiently represented in a long-term dissolution model.

SEM images were collected both before and after dynamic leach tests to observe any evolution of the sample microstructure (Figure 3-21 to Figure 3-28). The SEM imaging was performed on different areas of the sample surface, and therefore interpretation is subjective.

Ag-mordenite – The AgI (bright white spots) seen in the pre-leach HIP18-3 image seem to decrease in the post-leach HIP18-3 image, but the opposite is seen in HIP18-2. In the large-format HIP samples, the bright spots represent AgI isolations. The increase in exposed AgI in HIP18-2 could be a result of the dissolution of the Si matrix, which was ~2× higher compared to HIP18-4 (a duplicate of HIP18-3), while iodine dissolution was relatively lower.

HIP iodosodalite – In H1C5, there are fewer bright white spots associated with Ag or I (the larger white spots tend to represent Ag while the smaller, more distributed spots tend to be I; see EDS images in Appendix A) post-leach compared to the pre-leach image.

Tellurite glass – The tellurite glass sample shows striations in the post-leach SEM image; these striations could be caused by the polishing process induced preferred corrosion morphology. It confirms that matrix corrosion does occur, despite the low IDR measured.

Sintered iodosodalite, glass bonded sodalite ceramics, and glass composite material – The before and after leach SEM images for the sintered iodosodalites (WSU52 and WSU8), the glass-bonded sodalite ceramic (NaIBR) and the Ag-mordenite in GCM show little or no change. This implies a congruent dissolution of the matrix and AgI in these samples.

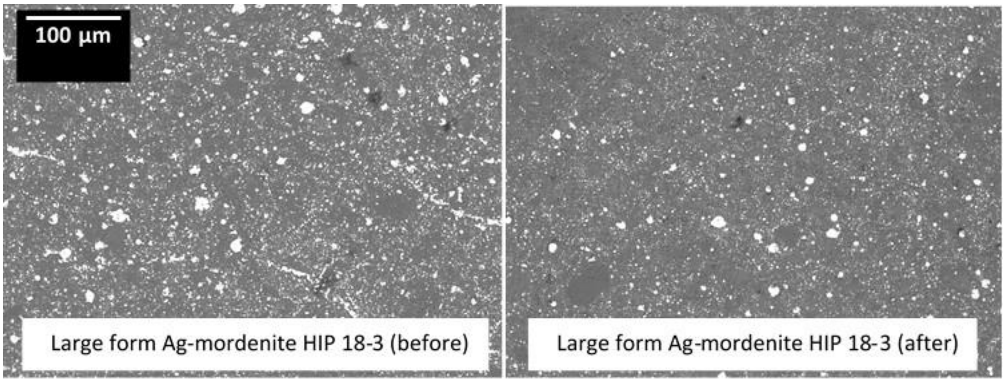

Figure 3-21. Before and after SEM images of the HIP18-3 large-form Ag-mordenite (left: pre-leach SEM; right: post-leach SEM). The scale bar in the top right applies to both images.

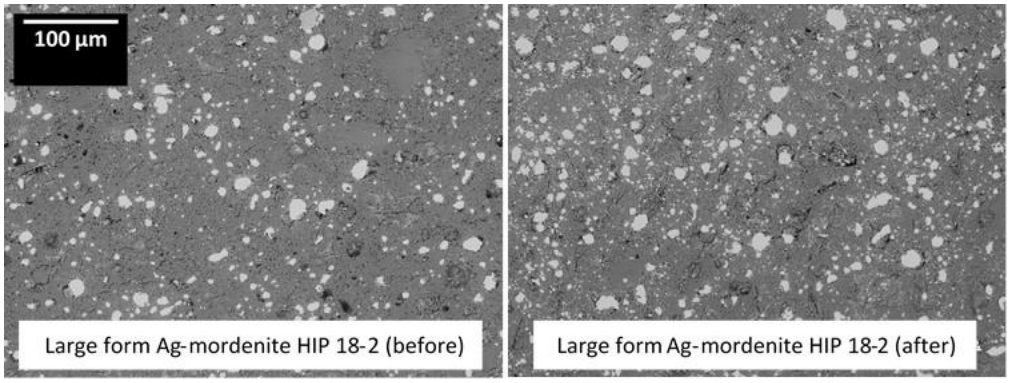

Figure 3-22. Before and after SEM images of the HIP18-2 large-form Ag-mordenite (left: pre-leach SEM; right: post-leach SEM). The scale bar in the top right applies to both images.

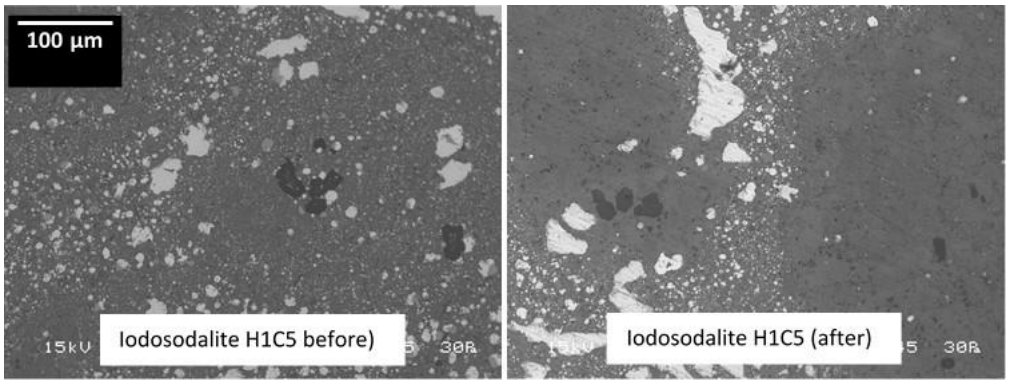

Figure 3-23. Before and after SEM images of iodosodalite H1C5 (left: pre-leach SEM; right: post-leach SEM). The scale bar in the top right applies to both images.

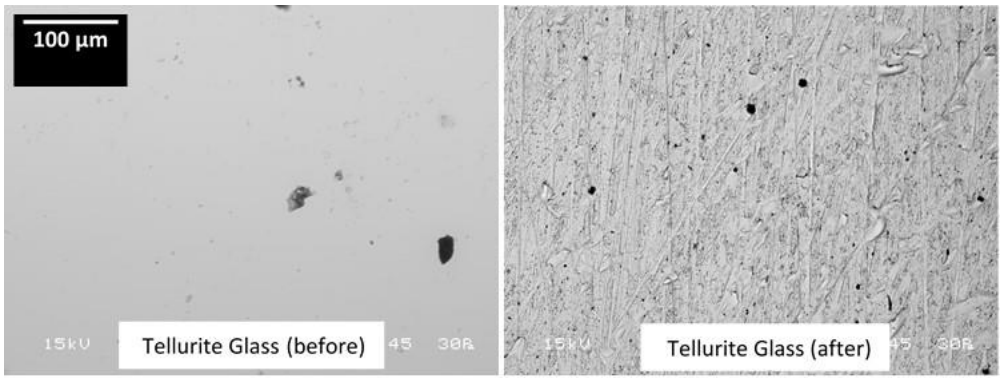

Figure 3-24. Before and after SEM images of the tellurite glass (left: pre-leach SEM; right: post-leach SEM). The scale bar in the top right applies to both images.

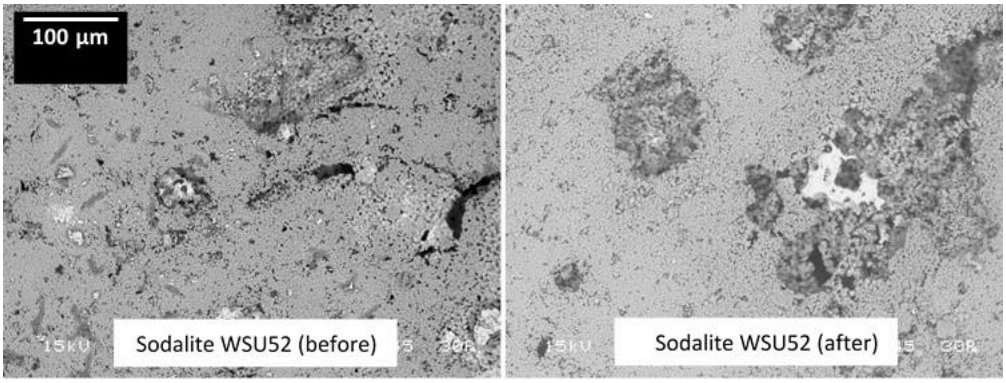

Figure 3-25. Before and after SEM images of the sintered sodalite WSU52 (left: pre-leach SEM; right: post-leach SEM). The scale bar in the top right applies to both images.

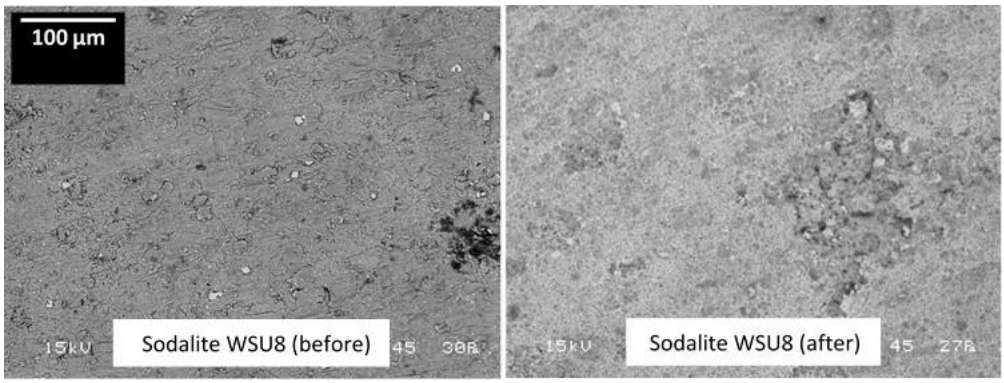

Figure 3-26. Before and after SEM images of the sintered sodalite WSU8 (left: pre-leach SEM; right: post-leach SEM). The scale bar in the top right applies to both images.

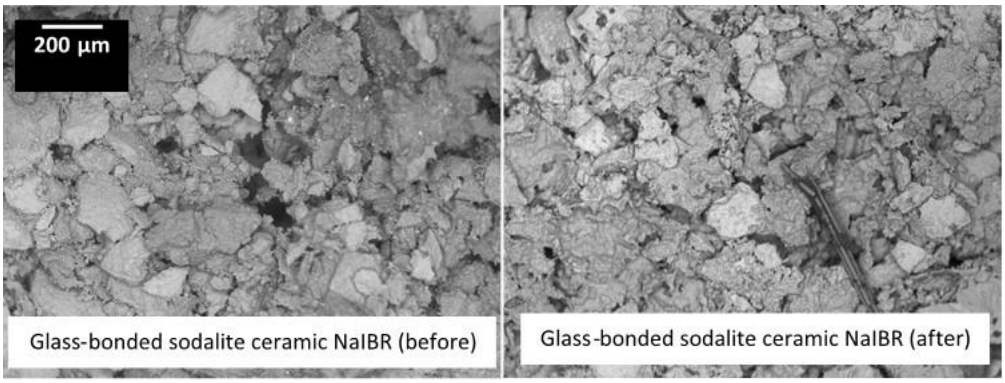

Figure 3-27. Before and after SEM images of the glass-bonded ceramic NaIBR (left: pre-leach SEM; right: post-leach SEM). The scale bar in the top right applies to both images.

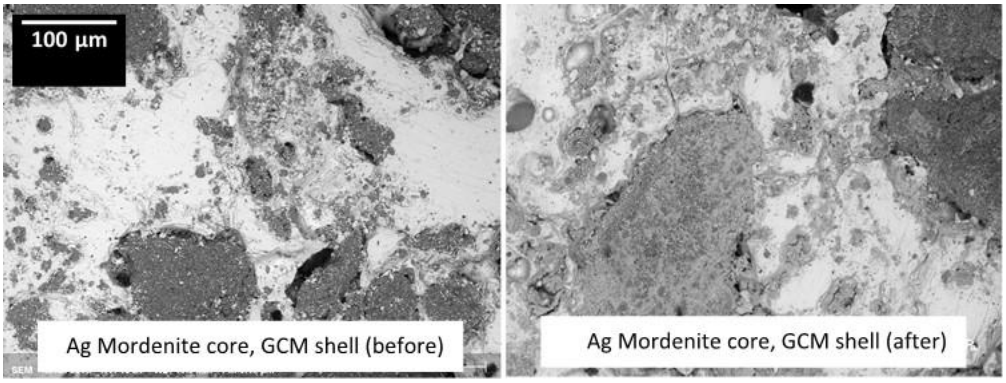

Figure 3-28. Before and after SEM images of the Ag-mordenite GCM (left: pre-leach SEM; right: post-leach SEM). The scale bar in the top right applies to both images.

3.4.2 Optical Profilometry

While SEM and EDS analysis can give an indication of microstructure changes, coupling these images with optical profilometry can give insight into topographical changes resulting from the leach test. This approach was used previously in SPFT testing of IWF (Asmussen et al. 2019). Representative images of each material class following the dynamic leach test are presented in Figure 3-29 and additional profilometry results can be found in Appendix B.

The tellurite glass has little surface feature change following the test, as the polishing lines are still visible, Figure 3-29a. The high porosity of the NaI glass bonded sodalite ceramic is apparent in Figure 3-29b, highlighting the need to consider true surface area measurements. Topographical features are observed on the two SFA samples, HIP in Figure 3-29c and SPS in Figure 3-29d. Based on prior SPFT testing, high Si containing phases are more resistant to corrosion and would represent the high points on the sample surface. The small-form Ag-mordenite samples, HIP 17-17 and 17-22 in Figure 3-29e and Figure 3-29f, respectively, show similar features to those observed following SPFT testing. The receded areas on the sample surface correspond to areas that are higher in Al and alkalis, but lower in iodine. The HIPed iodosodalite samples, Figure 3-29g and Figure 3-29h, show large corroded regions running between areas where less corrosion was observed. The regions of corrosion appear to correlate in size to the isolations of Ag observed in the microstructure prior to testing.

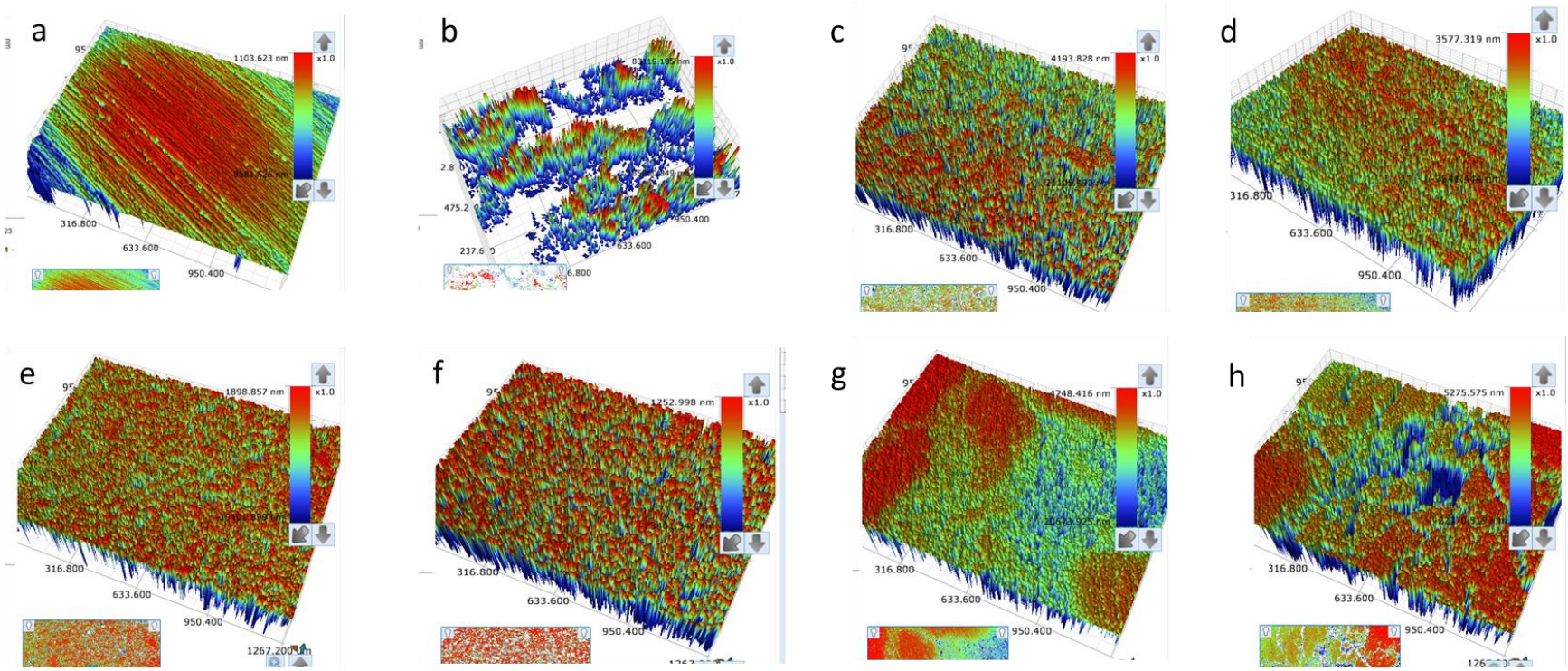

Figure 3-29. Post-leach optical profilometry images for a) Te glass, b) NaI, c) Aero HIP 2, d) SPS-2, e) HIP 17-17, f) HIP 17-22. g) H1C5, and h) H1C8.

4. SUMMARY AND CONCLUSIONS

This report was prepared in support of the effort to define a test suite to evaluate the corrosion of IWFs with the goal of defining and parameterizing a conceptual long-term corrosion model. Previous efforts have used a range of corrosion test methods (e.g., PCT, SPFT, ANSI/ANS 16.1) on IWFs. A review was presented highlighting the vast variability between IWF corrosion data that is available in the literature and the need for a standardized test suite. The targeted test suite is composed of a single-interval screening test, a dynamic leach test, and solid characterization of the monolithic IWF samples used in the tests. The data presented serves two purposes: (1) to expand the range of IWF evaluated with the test suite to assess method variability and (2) to further understand the corrosion of IWF to best inform conceptual long-term corrosion model development.

Test Suite Refinement

The IWF samples were evaluated using the 3-day screening test. Replicate tests showed that trends in durability can be identified between samples of the same material class. However, some variability was present in duplicate measurements and thus it is suggested that multiple runs be performed on samples. Because of the unique nature of many IWFs, only a single sample may be available during development efforts and replicate runs would be challenging. However, no trend was observed with the IDRs or SDRs increasing/decreasing on repeat runs after re-polishing samples. This observation justifies re-polishing samples to re-use in replicate tests.

An expansion of the dataset from the dynamic leach tests was also presented. Similar to the screening test, consistency in the SDRs and IDRs was observed between samples across multiple runs. The average SDRs and IDRs were also relatively constant during the dynamic leach test, except for both the HIPed and sintered iodosodalite samples. Again, replicate runs are recommended to ensure experimental error is captured.

Tests were also carried out at differing SA/V ratios to assess if the proposed ratio of 1:10 cm^2/mL attains dilute conditions where the common ion effect would be minimized and if cases where the calculated volume does not fully cover the sample and extra leachant is needed give differing results. It was confirmed that the SA/V ratios used did not induce large fluctuations in measured SDR and IDR, however the systems may already be at a saturated state with respect to the common ion effect.

Conceptual Model Development

The common ion effect, which can slow the corrosion of silicon-based materials, was observed for the IWF samples. In conditions where the dissolved matrix components increased or Si was added to the leachant, the dissolution of the IWF was slowed. This solution feedback mechanism should be captured in a conceptual model, possibly in similar fashion to the transition state theory used to model glass corrosion.

Changing the test temperature led to decreases in IDR and SDR, with SDR values measured in room temperature tests as well. For the small-form Ag-mordenite samples where tests at three temperatures were available, a strong linear correlation between the SDR and inverse temperature was observed, suggesting an Arrhenius relationship. To represent the temperature dependence on rate, an activation energy component for the matrix phase can be included in a conceptual model.

IWF Specific Information

- HIP Ag-mordenite: The HIPed Ag-mordenite measured similar SDRs in both the large- and small-form samples. The small-form samples measured lower IDRs compared with the large-form samples. The iodine loading variance of the large-form samples affected the iodine retention as higher iodine loading samples measured higher IDRs. Observing the surface of the Ag-mordenite samples after corrosion once again showed that the Al- and alkali-rich phases that run between the Si-rich, iodine containing phases demonstrate a higher degree of corrosion. Analysis of the surface using site-specific μXRD showed little difference in the mineralogy before and after leach testing.

Higher resolution spectroscopic techniques, or in situ microscopy, will be needed to observe individual AgI isolation dissolution.

- HIP iodosodalites: Five HIPed iodosodalite samples were tested. The samples made with an Ionex™ zeolite at 100% iodine loading and a hydrothermally generated iodosodalite had the lowest IDRs. The SDRs for the samples were near identical. Selective corrosion was observed within the sample micro-structure with Ag-rich isolations appearing to be attacked.
- Sintered and pressed iodosodalites: Four sintered iodosodalites, fabricated using two different glass binders, were evaluated. The samples measured much higher IDRs and SDRs compared with the other waste form types. Similar samples produced via pressing gave much lower SDRs and IDRs.
- Glass bonded sodalite ceramics: Two forms of the glass-bonded sodalite ceramics were evaluated: an NaI form and an AgI form. The samples are porous and require true surface area measurements to correct for, instead of geometric. However, the NaI form measured a lower IDRs than the AgI form and the cause of this unexpected response is unknown.
- Tellurite glass: The tellurite glass had the lowest IDR measured in the test effort. The unique nature of this waste form type is intriguing and should be evaluated further for applicability or other similar waste form types that can impart similar corrosion resistance.
- Iodoapatite ceramic: The Pb-V iodoapatite ceramic had similar IDR to the other waste form classes. The IDR for the iodoapatite ceramic decreased with time.
- Silver-functionalized silica-based aerogels: The SPSed SFA had a lower IDR compared with the HIP SFA; however, the samples had similar SDRs. This observation indicates that SPS improves iodine retention likely through the higher density of the SPSed samples.
- Comparison to nuclear waste glass: The SDR of the IWFs evaluated were within an order of magnitude of the SDR of a representative nuclear waste glass, SON68. However, the IDRs of several of the IWF types (e.g., tellurite glass, HIP iodosodalite, SFA) were orders of magnitude lower than the matrix SDR, indicating that the waste form microstructures have properties that can increase iodine retention. Upon defining an initial conceptual model, the data available to date should be assessed against long-term performance in a repository to identify promising IWF types. The controlling mechanisms giving sufficient iodine retention in promising samples can be elucidated with focused studies.

In conclusion, the information provided in this report can be used to define a standardized test method for IWF corrosion testing and inform the development of a conceptual model. An initial discussion on the conceptual long-term dissolution model will be presented in a forthcoming report. An effort to parameterize and evaluate the model should be performed to identify promising IWFs that can significantly improve slowed radioiodine release within a repository. Further mechanistic understanding of IWF corrosion is also required to support model efforts, and initial efforts to monitor these processes in real time were planned for FY20 but not executed due to funding constraints and the pandemic restrictions.

5. References

40 CFR 61, "National Emission Standards for Hazardous Air Pollutants," Subpart H, "National Emission Standards for Emissions of Radionuclides Other than Radon from Department of Energy Facilities." U.S. Code of Federal Regulations..

ANSI/ANS-16.1, *Measurement of the Leachability of Solidified Low-Level Radioactive Wastes by a Short-Term Test Procedure*. American Nuclear Society, Washington, D.C.

Asmussen R, C Pearce, A Lawter, J Neeway, B Miller, B Lee, N Washton, J Stephenson, R Clayton, and M Bowden. 2016. *Getter Incorporation into Cast Stone and Solid State Characterizations*. PNNL-25577, Pacific Northwest National Laboratory: Richland, WA.

Asmussen RM, AR Lawter, J Bonnett, NC Canfield, JT Reiser, N Doi, and N Avalos. 2018a. *Completion of Milestone M4FT-19PN030105111: Experimental Suite for AgI Waste Forms – Submit Short Report to ANL*. PNNL-28326, Pacific Northwest National Laboratory, Richland, WA.

Asmussen RM, J Matyáš, NP Qafoku, and AA Kruger. 2018b. "Silver-functionalized silica aerogels and their application in the removal of iodine from aqueous environments." *Journal of Hazardous Materials*. https://doi.org/10.1016/j.jhazmat.2018.04.081

Asmussen RM, JV Ryan, J Matyáš, JV Crum, JT Reiser, N Avalos, EM McElroy, AR Lawter, and NC Canfield. 2019. "Investigating the Durability of Iodine Waste Forms in Dilute Conditions." *Materials* 12:686.

ASTM C1220-17, *Standard Test Method for Static Leaching of Monolithic Waste Forms for Disposal of Radioactive Waste*. ASTM International, West Conshohocken, PA.

ASTM C1285-14, *Standard Test Methods for Determining Chemical Durability of Nuclear, Hazardous, and Mixed Waste Glasses and Multiphase Glass Ceramics: The Product Consistency Test (PCT)*. ASTM International, West Conshohocken, PA.

Audubert F and J Lartigue. 2000. "Iodine immobilization in apatites." *Atalante Conference*. 4(4), 4-13

Babad, Harry, and Denis M. Strachan. "Method for immobilizing radioactive iodine." U.S. Patent 4,229,317, issued October 21, 1980.

Bruffey SH and RT Jubin. 2015. *Milestone Report-M3FT-15OR03120215-Recommend HIP Conditions for AgZ*. ORNL/SPR-2015/503, Oak Ridge National Laboratory, Oak Ridge, TN.

Bruffey SH and RT Jubin. 2018. *Preparation of Four Large Format Hot Isostatically Pressed I-AgZ Waste Form Samples for Performance Testing*. NTRD-MRWFD-2018-000198; ORNL/SPR-2018/1026, prepared by Oak Ridge National Laboratory for the U.S. Department of Energy, Washington, D.C.

Bruffey SH, JA Jordan, RT Jubin, ML Parks, and TR Watkins. 2017. *Hot Isostatic Pressing of Engineered Forms of I-AgZ*. NTRD-MRWFD-2017-000412, Oak Ridge National Laboratory, Oak Ridge, TN.

Campayo L, A Grandjean, A Coulon, R Delorme, D Vantelon, and D Laurencin. 2011. "Incorporation of iodates into hydroxyapatites: a new approach for the confinement of radioactive iodine." *Journal of Materials Chemistry* 21(44):17609-17611.

Chong S, BJ Riley, RM Asmussen, AR Lawter, SH Bruffey, J Nam, JS McCloy, and JV Crum. 2020. "Iodosodalite synthesis with hot isostatic pressing of precursors produced from aqueous and hydrothermal processes." *Journal of Nuclear Materials* 538:152222.

Chong S, JA Peterson, BJ Riley, D Tabada, D Wall, CL Corkhill, and JS McCloy. 2018. "Glass-bonded iodosodalite waste form for immobilization of ^{129}I." *Journal of Nuclear Materials* 504:109-121.

Coulon A, A Grandjean, D Laurencin, P Jollivet, S Rossignol, and L Campayo. 2017. "Durability testing of an iodate-substituted hydroxyapatite designed for the conditioning of I-129." *Journal of Nuclear Materials* 484:324-331.

Ebert, WL, TA Cruse, X Chem, VK Gattu, JL Jerden Jr. 2017. Status Report on Electrochemical Tests with AgI. NTRD-MRWFD-2017-000196. Argonne National Laboratory, Lemont, IL

Ebert WL. 2018. Test Method for Assessing the Quality of Iodide Waste Forms. M4NT-18AN030105008. Argonne National Laboratory, Lemont, IL.

Ebert WL, VK Gattu, and JA Fortner. 2019. Iodide Waste Form Degradation Tests: FY19 Status Report. ACL/CFCT-19/24, Argonne National Laboratory, Lemont, IL.

Ebert WL. 2019 *Test Method for Iodide Waste Form Process Development*. ANL/CFCT-18/7, prepared by Argonne National Laboratory for the U.S. Department of Energy, Washington, D.C.

Guy C, F Audubert, J-E Lartigue, C Latrille, T Advocat and C Fillet. 2002. "New conditionings for separated long-lived radionuclides." *Comptes Rendus Physique* 3(7-8):827-837.

Hassan M, S Venkatesan, and HJ Ryu. 2020. "Non-volatile immobilization of iodine by the cold-sintering of iodosodalite." *Journal of Hazardous Materials* 386:121646.

Hassan Mu and HJ Ryu. 2019. "Cold sintering and durability of iodate-substituted calcium hydroxyapatite (IO-HAp) for the immobilization of radioiodine." *Journal of Nuclear Materials* 514:84-89.

Jubin RT, SH Bruffey, and KK Patton. 2014. *Expanded Analysis of Hot Isostatic Pressed Iodine-Loaded Silver-Exchanged Mordenite*. FCRD-SWF-2014-000278; ORNL/LTR-2014/476, prepared by Oak Ridge National Laboratory for the U.S. Department of Energy, Washington, D.C.

Kaplan DI, KA Price, C Xu, D Li, P Lin, W Xing, R Nichols, K Schwehr, JC Seaman, T Ohnuki, N Chen, and PH Santschi. 2019. "Iodine speciation in a silver-amended cementitious system." *Environment International* 126:576-584

Lawter AR, J Bonnett, N Avalos, NC Canfield, and RM Asmussen. 2019. *Method Sensitivity Analysis for Iodine Waste Form Durability*. PNNL-29098 Rev.0, Pacific Northwest National Laboratory, Richland, WA.

Lee C-W, J-Y Pyo, J Heo, H-S Park, and J-H Yang. 2016. "Vitrification of the ^{129}I generated from Reprocessing using Silver Tellurite Glass." In *Proceedings of the KNS 2016 Autumn Meeting*, Korean Nuclear Society, Republic of Korea.

Maddrell E and P Abraitis. 2003. "A Comparison of Wasteforms and Processes for the Immobilisation of Iodine-129." *MRS Online Proceedings Library Archive* 807.

Maddrell E, A Gandy, and M Stennett. 2014. "The durability of iodide sodalite." *Journal of Nuclear Materials* 449(1-3):168-172.

Maddrell ER, ER Vance, C Grant, Z Aly, A Stopic, T Palmer, J Harrison, and DJ Gregg. 2019. "Silver iodide sodalite - Wasteform / Hip canister interactions and aqueous durability." *Journal of Nuclear Materials* 517:71-79.

Matyáš J and RK Engler. 2013. *Assessment of Methods to Consolidate Iodine-Loaded Silver-Functionalized Silica Aerogel*. FCRD-SWF-2013-000589; PNNL-22874, prepared by Pacific Northwest National Laboratory for the U.S. Department of Energy, Washington, D.C.

Matyáš J, ES Ilton, and L Kovařík. 2018. "Silver-functionalized silica aerogel: Towards an understanding of aging on iodine sorption performance." *RSC Advances* 8:31843-31852.

Matyáš J, N Canfield, S Silaiman, and M Zumhoff. 2016. "Silica-based waste form for immobilization of iodine from reprocessing plant off-gas streams." *Journal of Nuclear Materials* 476:255-261.

Mowry CD, PV Brady, TJ Garino, and TM Nenoff. 2015. "Development and Durability Testing of a Low-Temperature Sintering Bi–Si–Zn Oxide Glass Composite Material (GCM) ^{129}I Waste Form." *Journal of the American Ceramic Society* 98(10):3094-3104.

Nam J, S Chong, BJ Riley, and JS McCloy. 2018. "Iodosodalite Waste Forms from Low-Temperature Aqueous Process." *MRS Advances* 3:1093-1103.

Neeway JJ, NP Qafoku, BD Williams, MMV Snyder, CF Brown, and EM Pierce. 2016. "Evidence of technetium and iodine release from a sodalite-bearing ceramic waste form." *Applied Geochemistry* 66(C):210-218.

Nenoff TM, TJ Garino, and K Croes. 2015. *Complete Initial Scoping Tests on the Incorporation of Novel Loaded Iodine Getters into GCM*. No. SAND-2015-7179R, Sandia National Laboratories, Albuquerque, NM.

Pierce EM, EA Rodriguez, LJ Calligan, WJ Shaw, and BP McGrail. 2008. "An experimental study of the dissolution rates of simulated aluminoborosilicate waste glasses as a function of pH and temperature under dilute conditions." *Applied Geochemistry* 23(9):2559-2573.

Riley BJ, JD Vienna, DM Strachan, JS McCloy, and JL Jerden. 2016. "Materials and processes for the effective capture and immobilization of radioiodine: A review." *Journal of Nuclear Materials* 470:307-326.

Riley, B.J., J.A. Peterson, N.L. Canfield, S.M. Frank. September 2019. *Ceramic waste form process for immobilizing iodine in glass-bonded iodosodalite*, PNNL-SA-145969, Pacific Northwest National Laboratory, Richland, WA.

Saslow S, W Um, R Russell, B Williams, R Assmussen, T Varga, O Qafoku, B Riley, A Lawter, and M Snyder. 2018. *Effluent Management Facility Evaporator Bottoms: Waste Streams Formulation and Waste Form Qualification Testing*. PNNL-26570, Pacific Northwest National Laboratory, Richland, WA.

Saslow SA, M Snyder, BD Williams, RM Asmussen, SR Baum, II Leavy, and T Varga. 2019. *Leach Testing of Laboratory-Scale Melter Evaporator Condensate Cementitious Waste Forms*. PNNL-28197, Pacific Northwest National Laboratory, Richland, WA.

Saslow SA, W Um, RL Russell, G Wang, RM Asmussen, and R Sahajpal. 2017. *Updated Liquid Secondary Waste Grout Formulation and Preliminary Waste Form Qualification*. PNNL-26443, Pacific Northwest National Laboratory, Richland, WA.

Sava DF, TJ Garino, and TM Nenoff. 2012. "Iodine Confinement into Metal–Organic Frameworks (MOFs): Low-Temperature Sintering Glasses To Form Novel Glass Composite Material (GCM) Alternative Waste Forms." *Industrial & Engineering Chemistry Research* 51(2):614-620.

Schneider CA, WS Rasband, and KW Eliceiri. 2012. "NIH Image to ImageJ: 25 years of image analysis." *Nature Methods* 9:671.

Serne RJ, DC Lanigan, JH Westsik, BD Williams, H Jung, and G Wang. 2016. *Extended Leach Testing of Simulated LAW Cast Stone Monoliths*. PNNL-24297, Pacific Northwest National Laboratory, Richland, WA.

Sheppard GP, JA Hriljac, ER Maddrell, and NC Hyatt. 2006. "Silver Zeolites: Iodide Occlusion and conversion to Sodalite–a potential 129 I waste form?" *MRS Online Proceedings Library Archive* 932.

Sheppard GP. 2009. *Immobilisation of Iodine in Condensed Zeolite Systems*. Doctor of Philosophy, School of Chemistry, University of Birmingham, Birmingham, United Kingdom.

Suetsugu Y. 2014. "Synthesis of lead vanadate iodoapatite utilizing dry mechanochemical process." *Journal of Nuclear Materials* 454(1-3):223-229.

Szántó Z, E Svingor, M Molnar, L Palcsu, I Futó and Z Szűcs. 2002. "Diffusion of 3H, 99Tc, 125I, 36Cl and 85Sr in granite, concrete and bentonite." *Journal of Radioanalytical and Nuclear Chemistry* 252(1):133-138.

Tanabe H, T Sakuragi, K Yamaguchi, T Sato, and H Owada. 2010. "Development of new waste forms to immobilize iodine-129 released from a spent fuel reprocessing plant." *Advances in Science and Technology* 73:158-170.

Uno M, M Shinohara, K Kurosaki, and S Yamanaka. 2001. "Some properties of a lead vanado-iodoapatite Pb_{10} (VO_4) $_6I_2$." *Journal of Nuclear Materials* 294(1-2):119-122.

Vance ER, C Grant, I Karatchevtseva, Z Aly, A Stopic, J Harrison, G Thorogood, HR Wong, and DJ Gregg. 2018. "Immobilization of iodine via copper iodide." *Journal of Nuclear Materials* 505:43-148.

Vinokurov S, YM Kulyako, O Slyunchev, S Rovnyi, A Wagh, M Maloney, and B Myasoedov. 2009. "Magnesium potassium phosphate matrices for immobilization of high-level liquid wastes." *Radiochemistry* 51(1): 65-72.

Yang JH, HS Park, DH Ahn, and MS Yim. 2016. "Glass composite waste forms for iodine confined in bismuth embedded SBA-15." *Journal of Nuclear Materials* 480:150-158.

Yang K, W Zhu, S Scott, Y Wang, J Wang, BJ Riley, J Vienn and J Lian. 2020. "Immobilization of Cesium and Iodine into $Cs_3Bi_2I_9$ Perovskite-silica Composites and Core-shell Waste Forms with High Waste Loadings and Chemical Durability." *Journal of Hazardous Materials* 401:123279.

Yao T, F Lu, H Sun, J Wang, RC Ewing, and J Lian. 2014. "Bulk iodoapatite ceramic densified by spark plasma sintering with exceptional thermal stability." *Journal of the American Ceramic Society* 97:2409-2412.

Zhang Z, A Heath, K Valsaraj, W Ebert, T Yao, J Lian, and J Wang. 2018. "Mechanism of iodine release from iodoapatite in aqueous solution." *RSC Advances* 8:3951-3957.

Zhang ZL, L Gustin, WW Xie, J Lian, KT Valsaraj, and JW Wang. 2019. "Effect of solution chemistry on the iodine release from iodoapatite in aqueous environments." *Journal of Nuclear Materials* 525:161-170.

Appendix A

Sample Characterization

A-1. SEM Images and EDS Maps

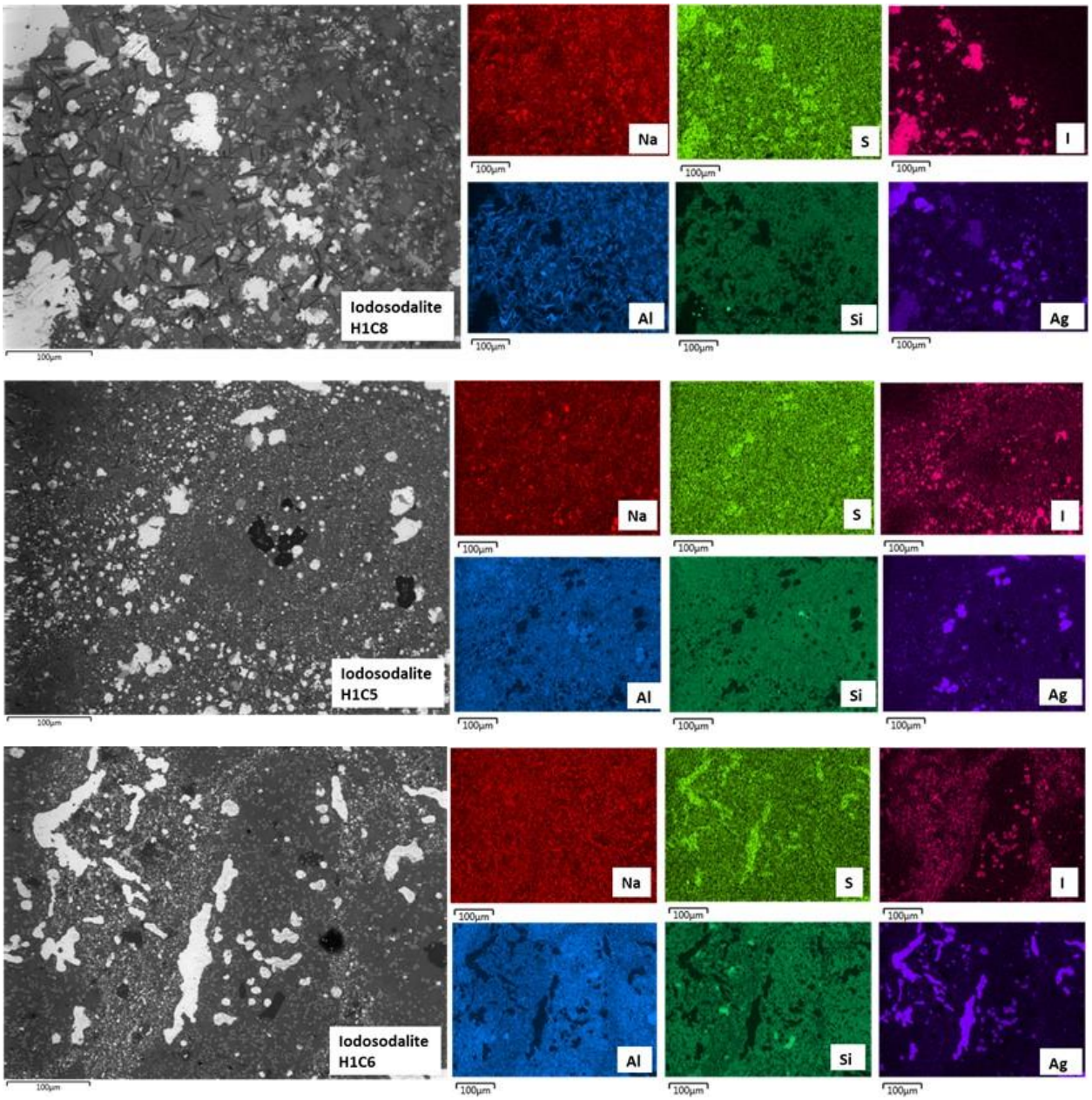

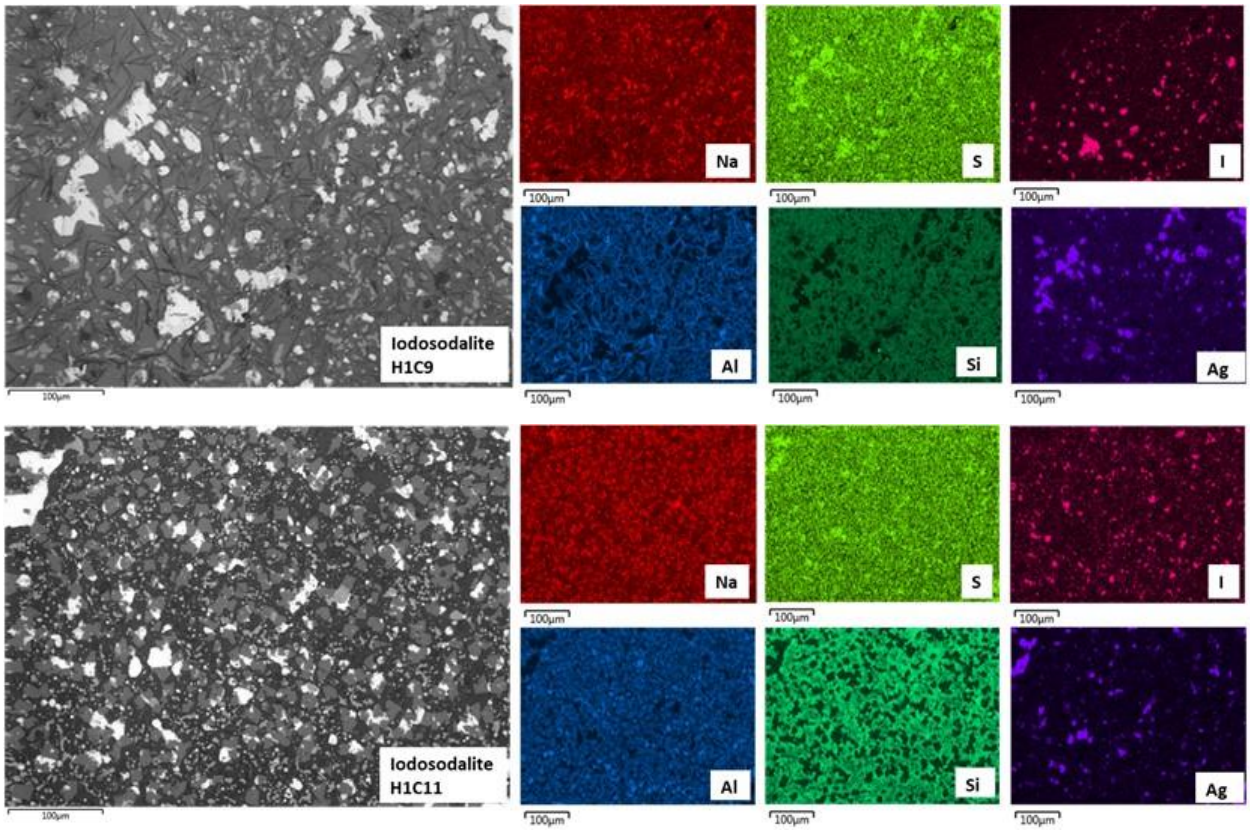

Figure A.1. SEM micrograph and the corresponding EDS maps of the HIPed Iodosodalite samples.

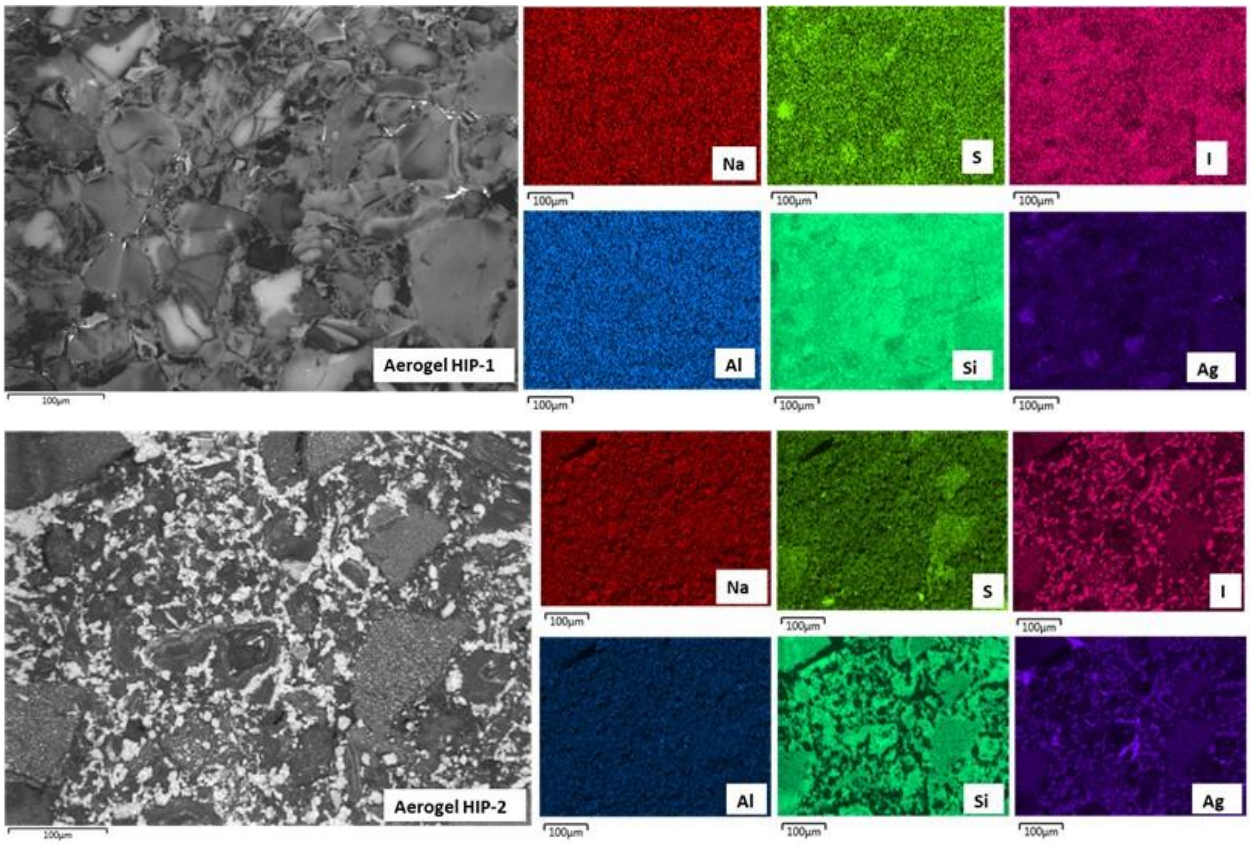

Figure A.2. SEM micrograph and the corresponding EDS maps of an example HIPed SFA samples.

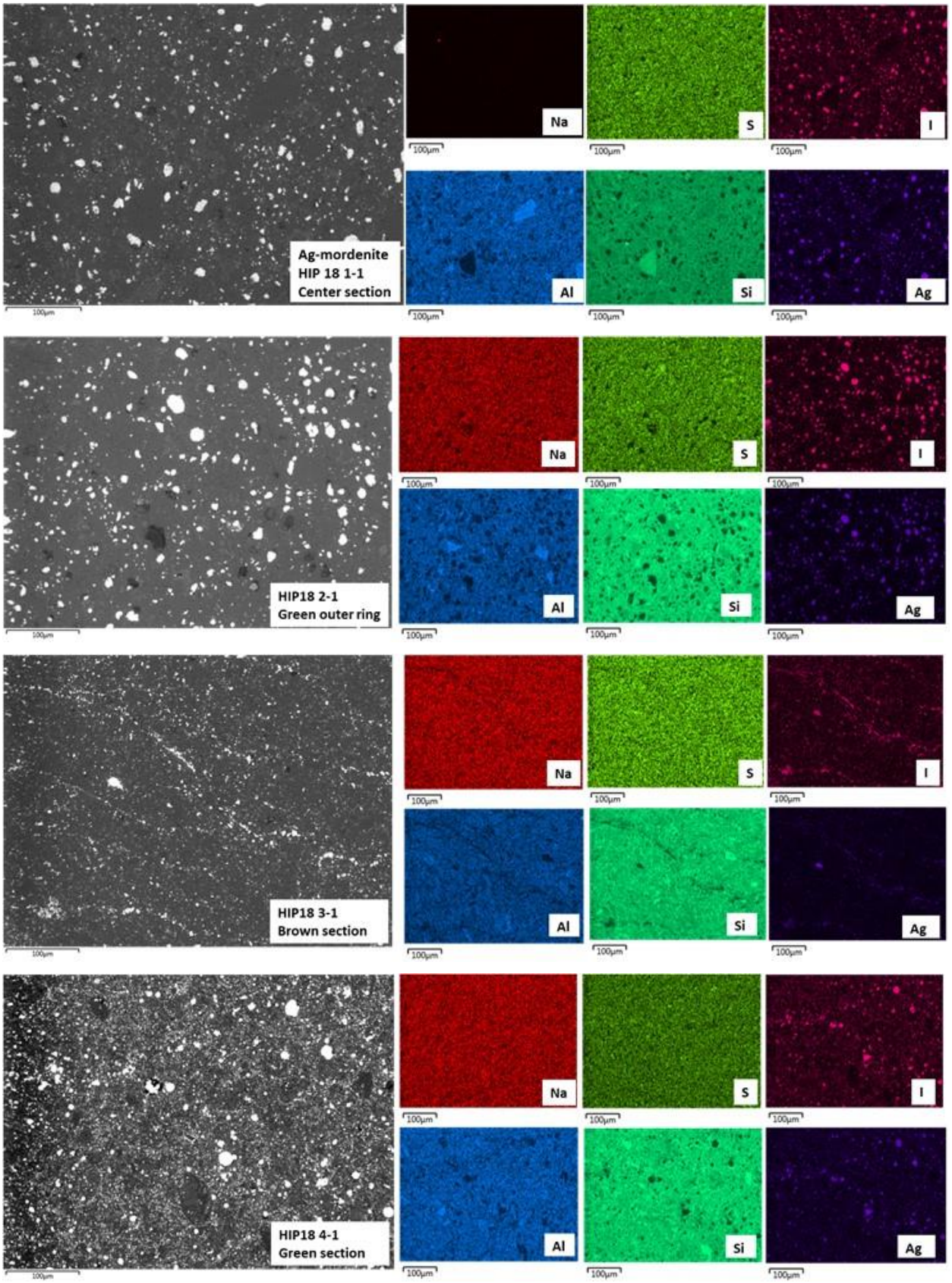
Ag-mordenite
HIP 18 1-1
Center section
Na
S
I
Al
Si
Ag
HIP18 2-1
Green outer ring
Na
S
I
Al
Si
Ag
HIP18 3-1
Brown section
Na
S
I
Al
Si
Ag
HIP18 4-1
Green section
Na
S
I
Al
Si
Ag

Figure A.3. SEM micrograph and the corresponding EDS maps of the HIPed Ag-mordenite large-form samples.

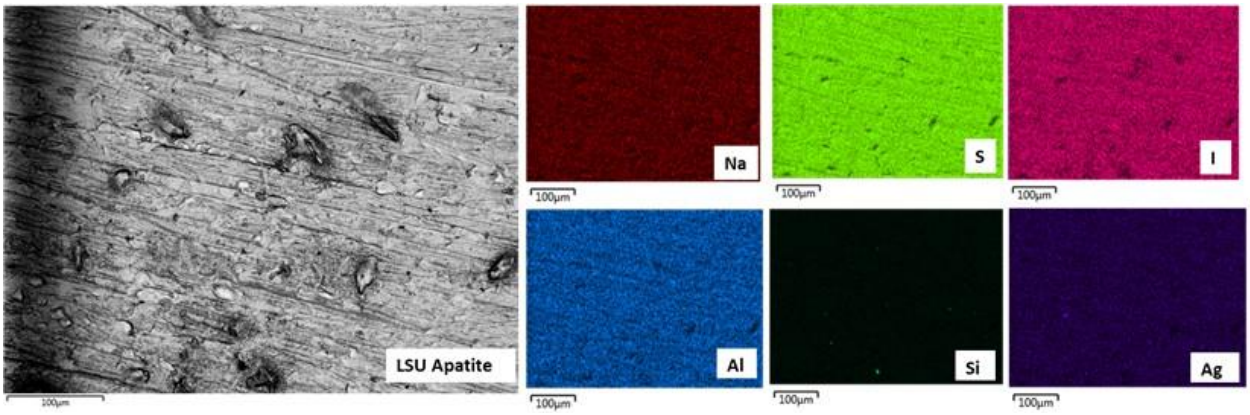

Figure A.4. SEM micrograph and the corresponding EDS maps of the iodoapatite ceramic

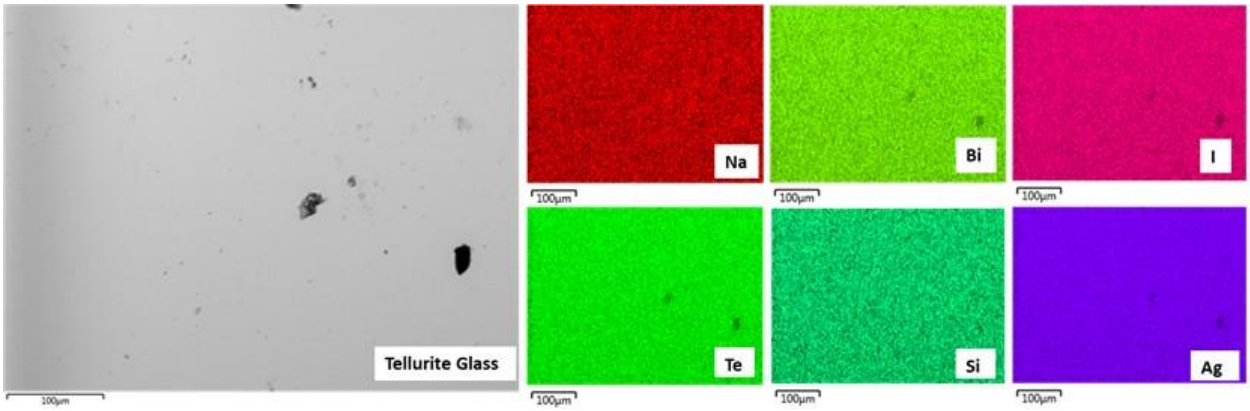

Figure A.5. SEM micrograph and the corresponding EDS maps of the tellurite glass

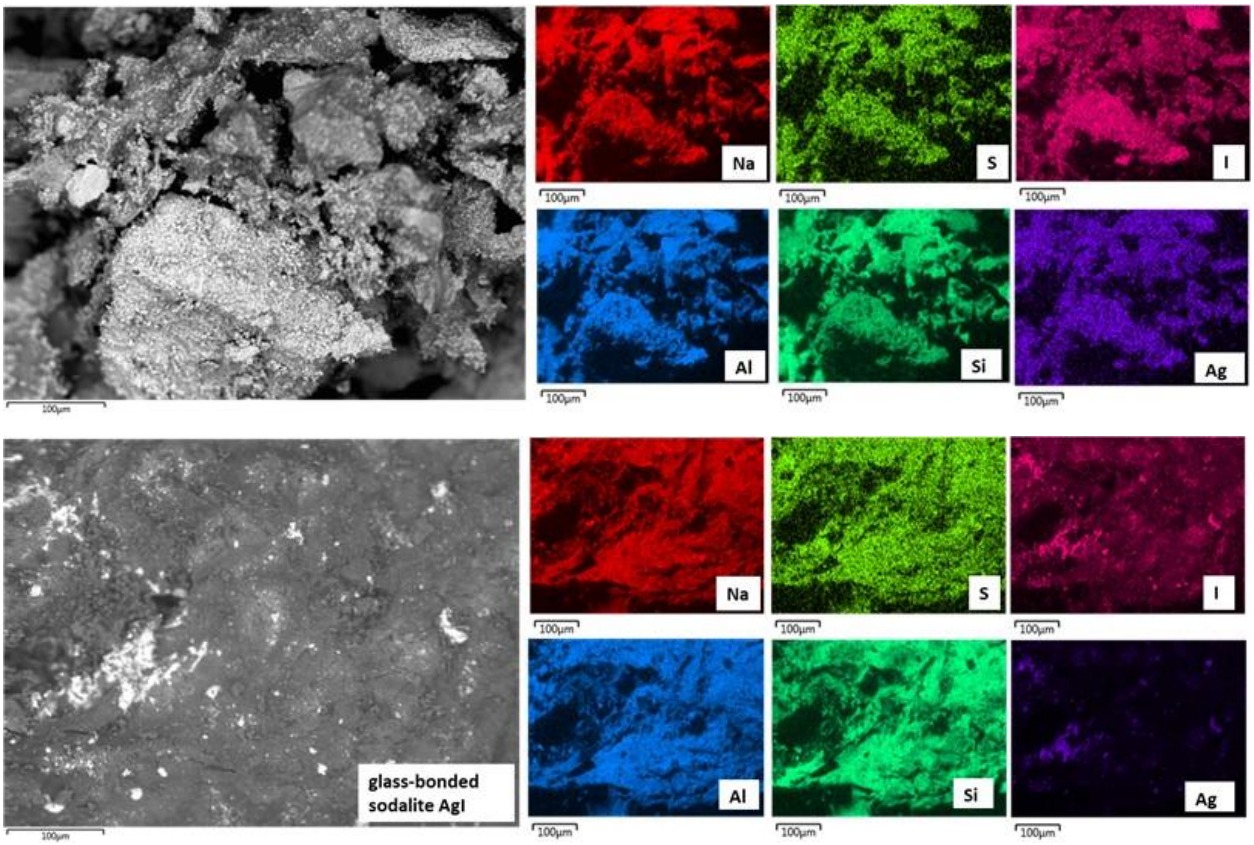

Figure A.6. SEM micrograph and the corresponding EDS maps of the glass bonded sodalite samples.

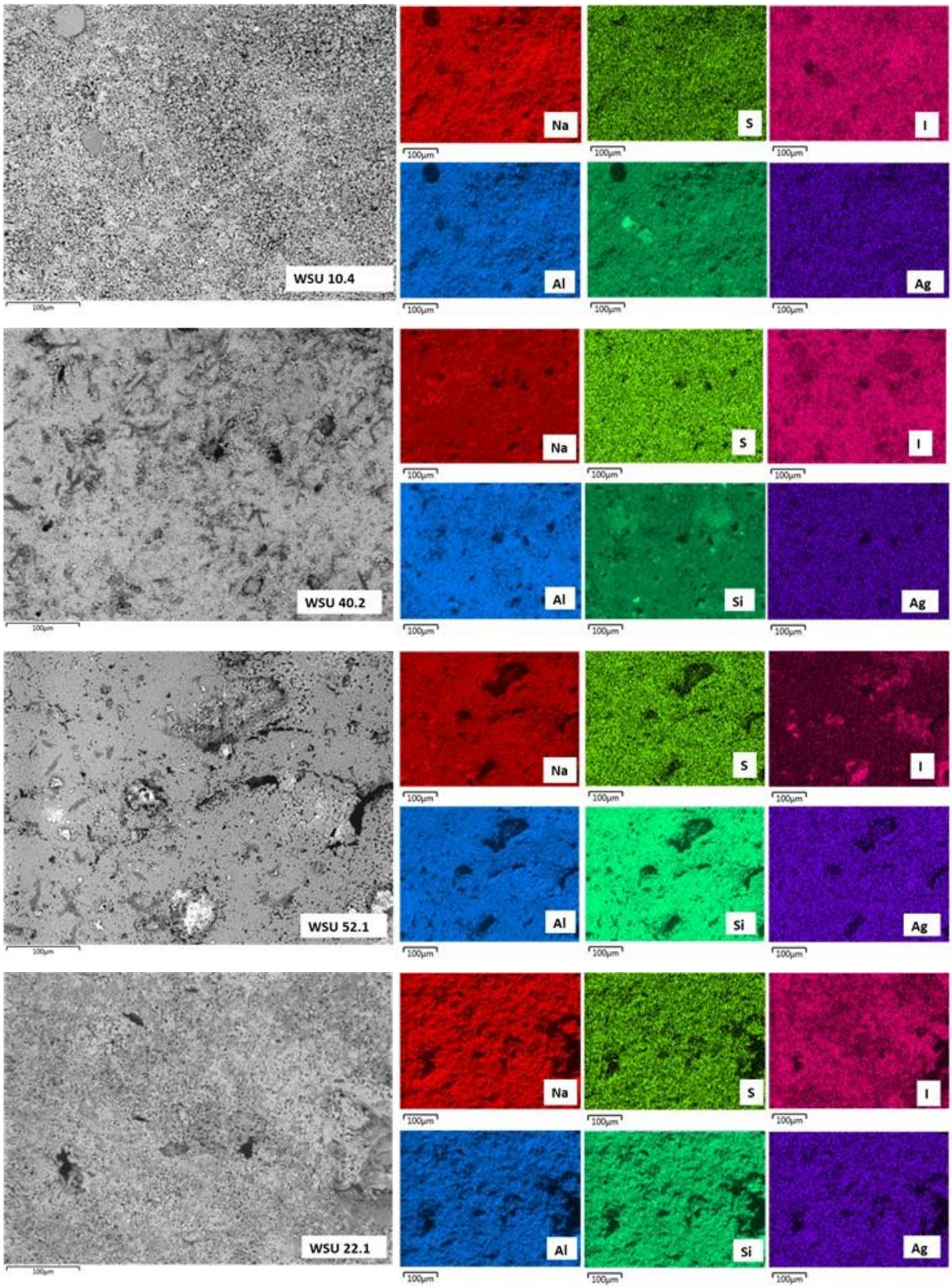

Figure A.7. SEM micrograph and the corresponding EDS maps of the WSU sodalite samples.

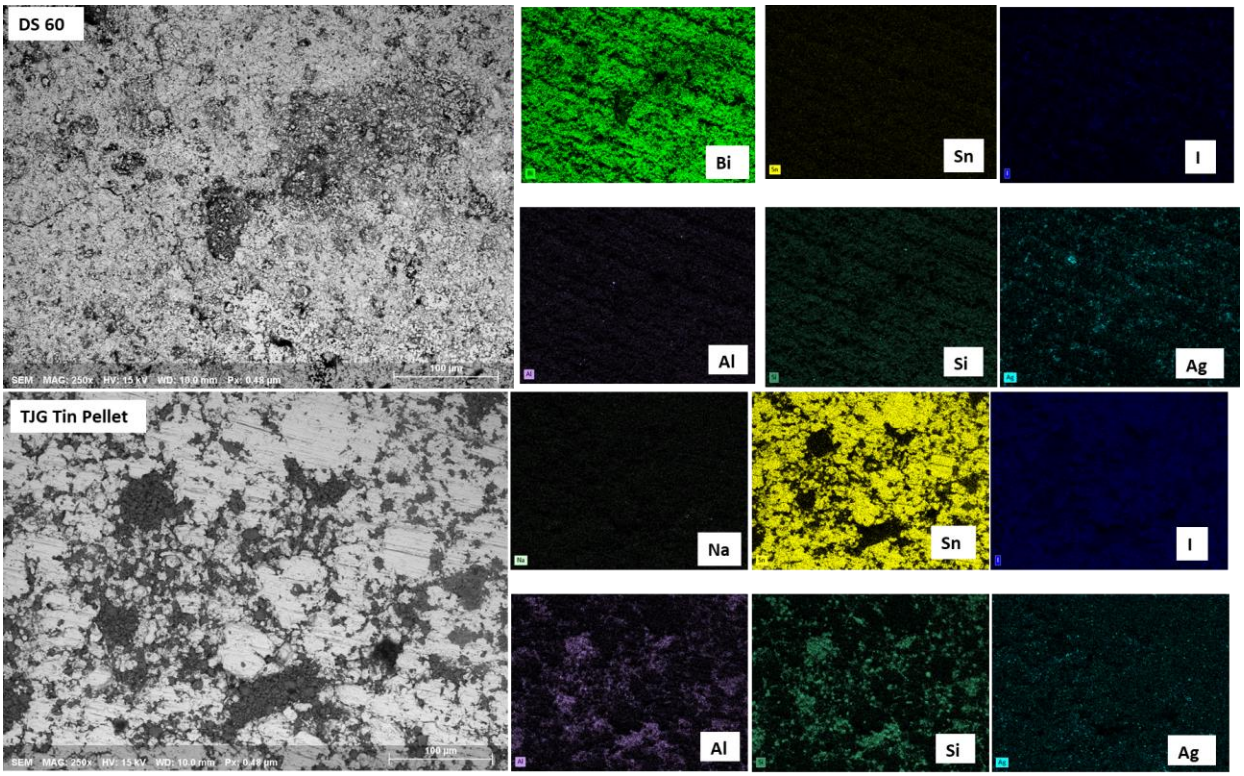

Figure A.8. SEM micrographs and the corresponding EDS maps of the DS 60 Ag mordenite and the Tin Pellet samples.

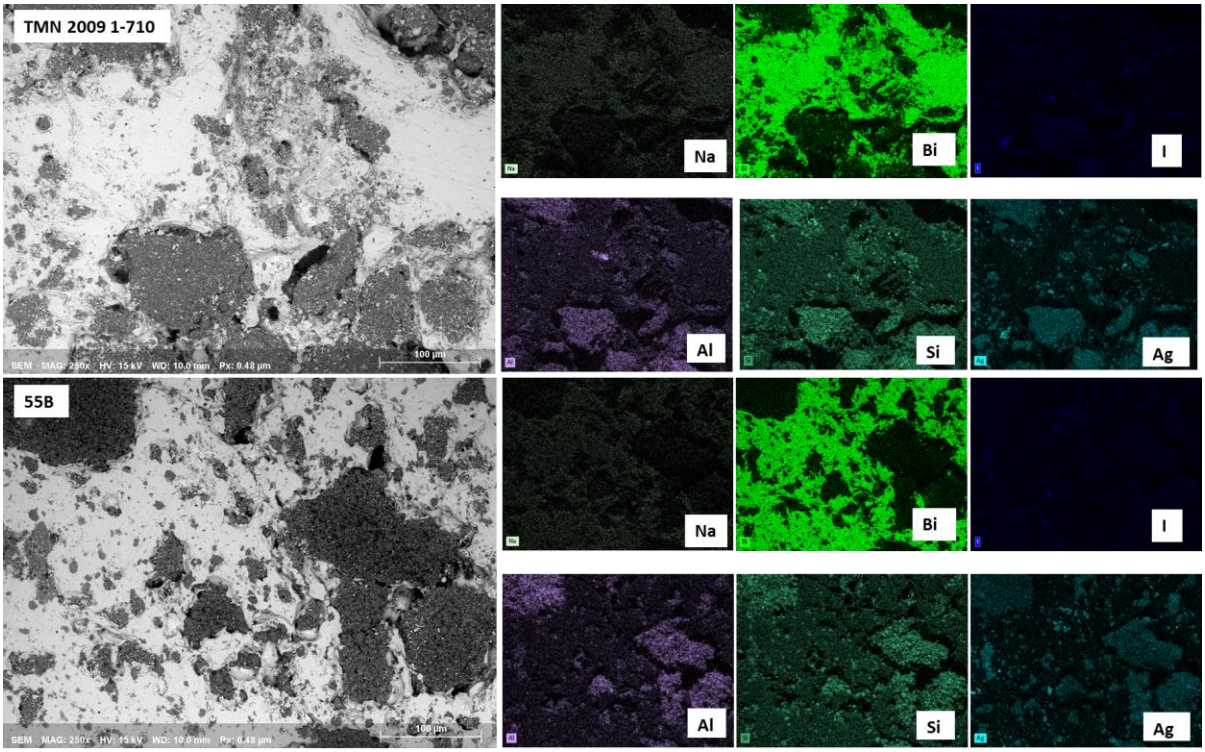

Figure A.9. SEM micrographs and the corresponding EDS maps of the 71D and 55B Ag mordenite in GCM samples.

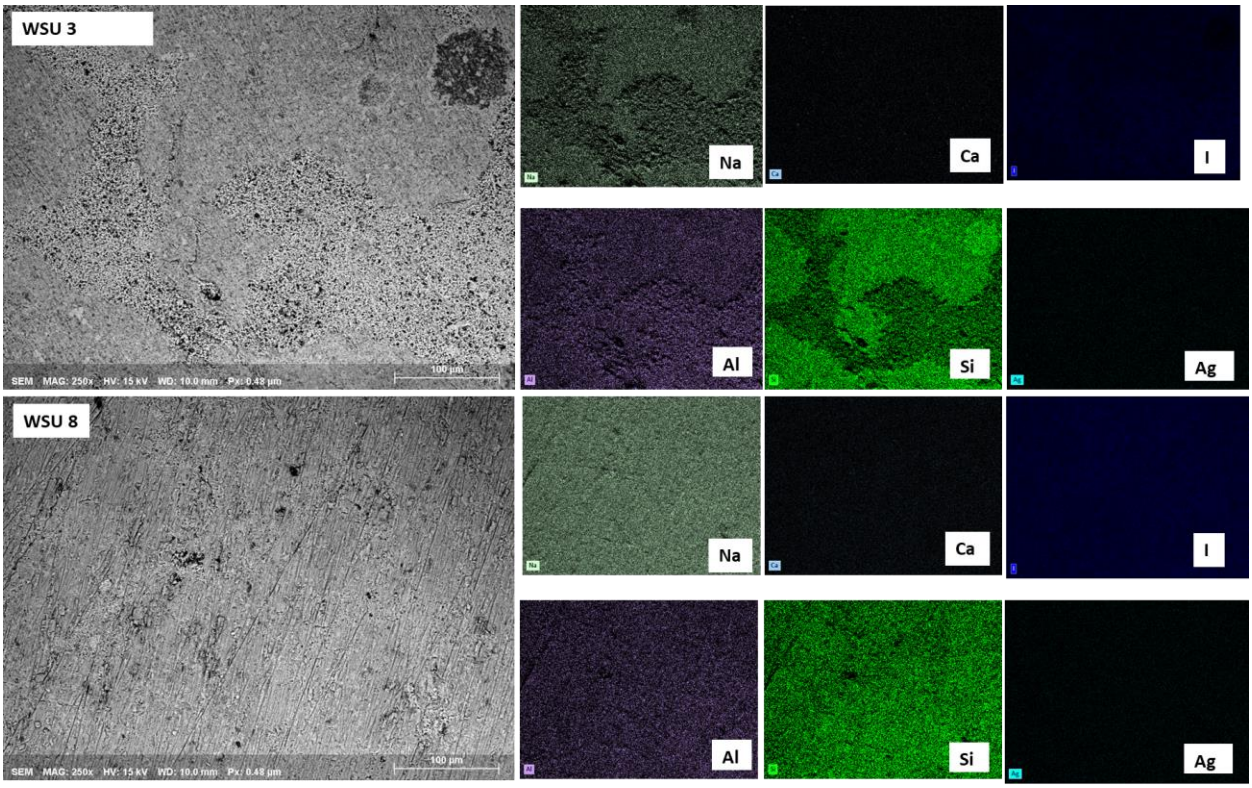

Figure A.10. SEM micrographs and the corresponding EDS maps of the sodalite WSU3 and WSU8 samples.

A-2. Post-leach SEM Images and EDS Maps

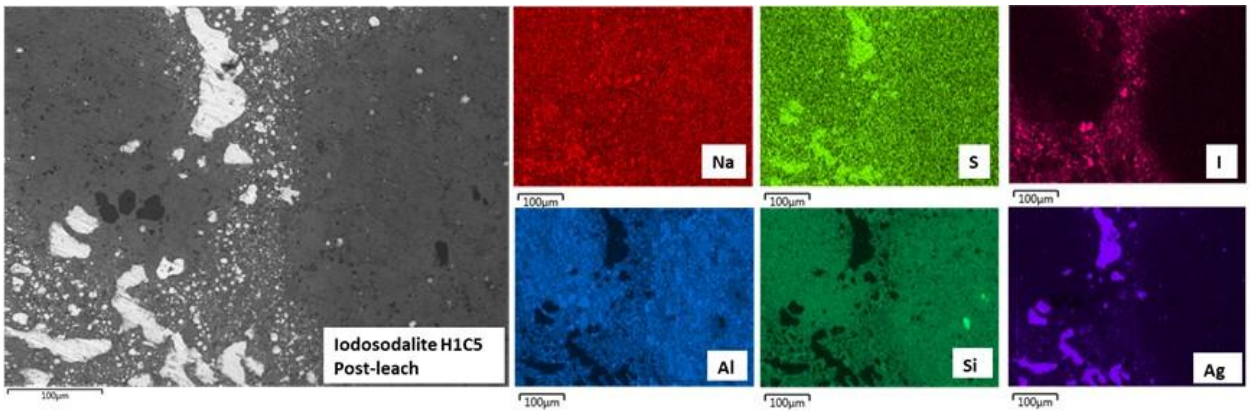

Figure A.11. Post-leach SEM micrograph and the corresponding EDS maps of HIPed iodosodalite sample H1C5.

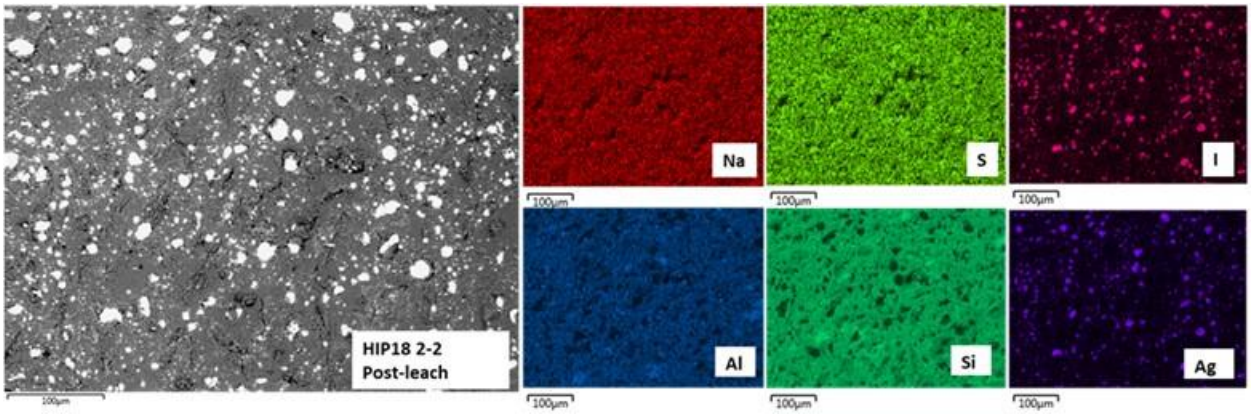

Figure A.12. Post-leach SEM micrograph and the corresponding EDS maps of large-form Ag-mordenite sample HIP182-2.

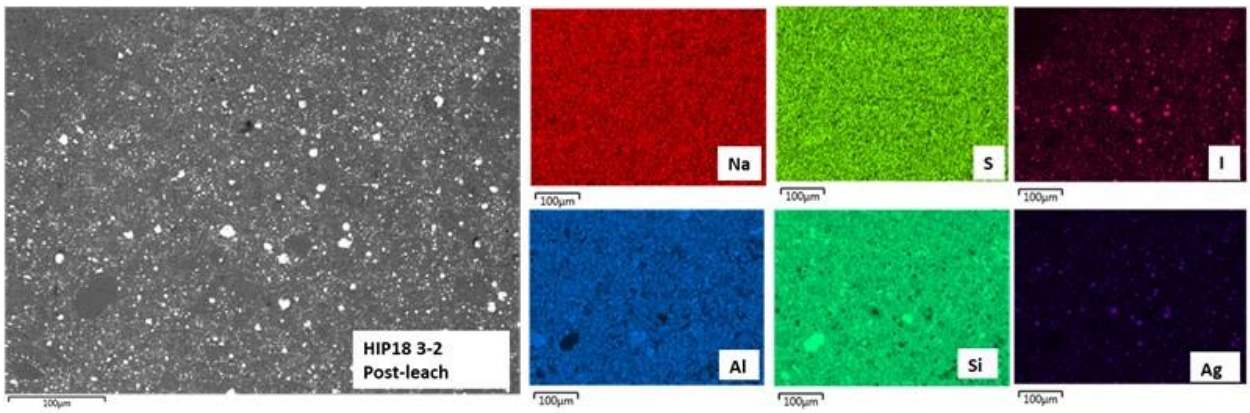

Figure A.13. Post-leach SEM micrograph and the corresponding EDS maps of large-form Ag-mordenite sample HIP18 3-2.

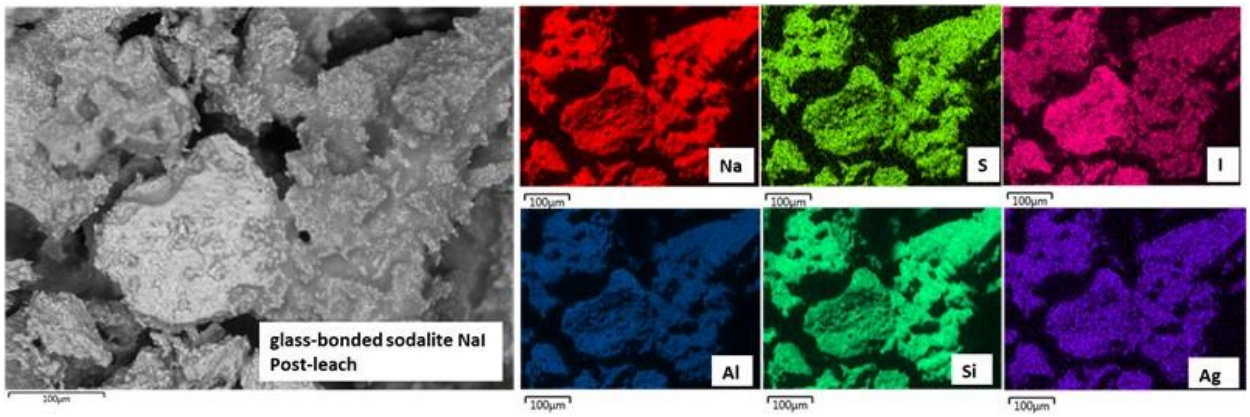

Figure A.14. Post-leach SEM micrograph and the corresponding EDS maps of glass-bonded sodalite sample NaIBR.

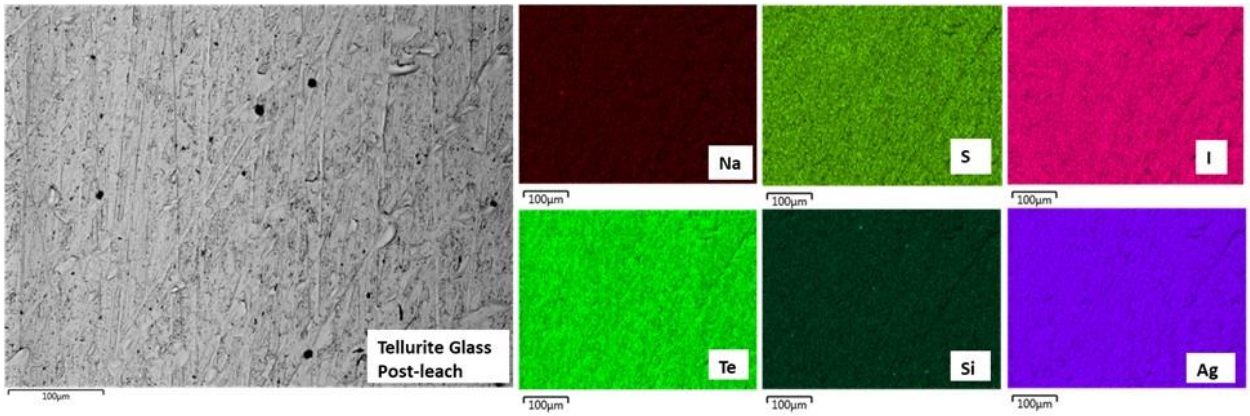

Figure A.15. Post-leach SEM micrograph and the corresponding EDS maps of glass-bonded sodalite sample NaIBR.

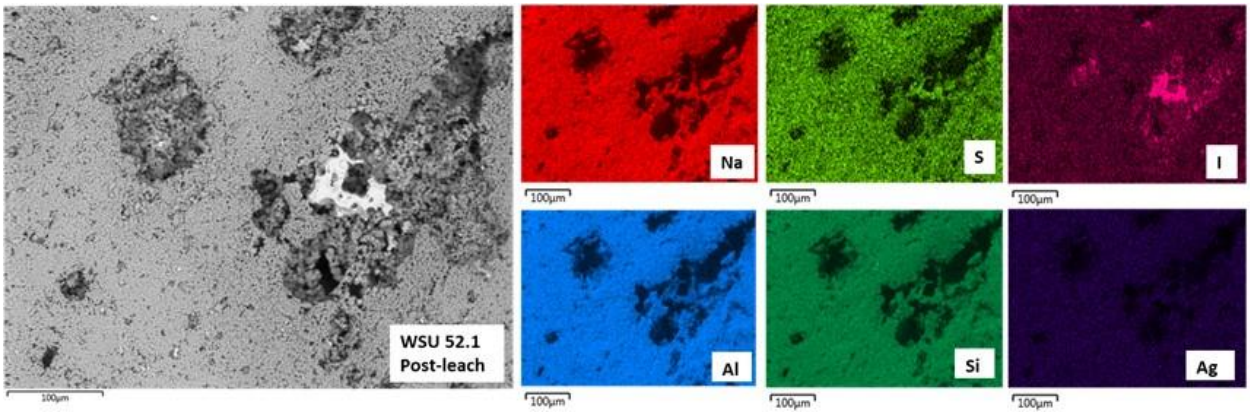

Figure A.16. Post-leach SEM micrograph and the corresponding EDS maps of sodalite sample WSU 52.1.

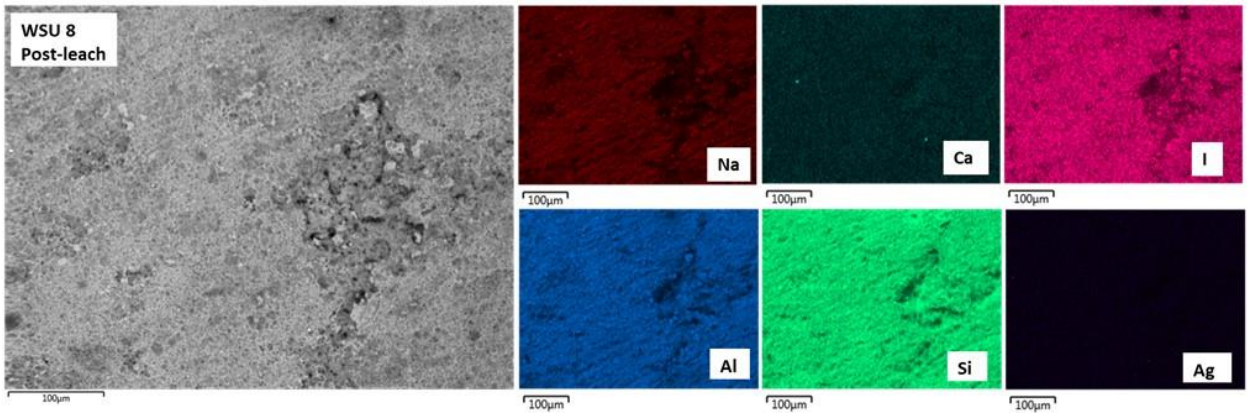

Figure A.17. Post-leach SEM micrograph and the corresponding EDS maps of sodalite sample WSU 8.

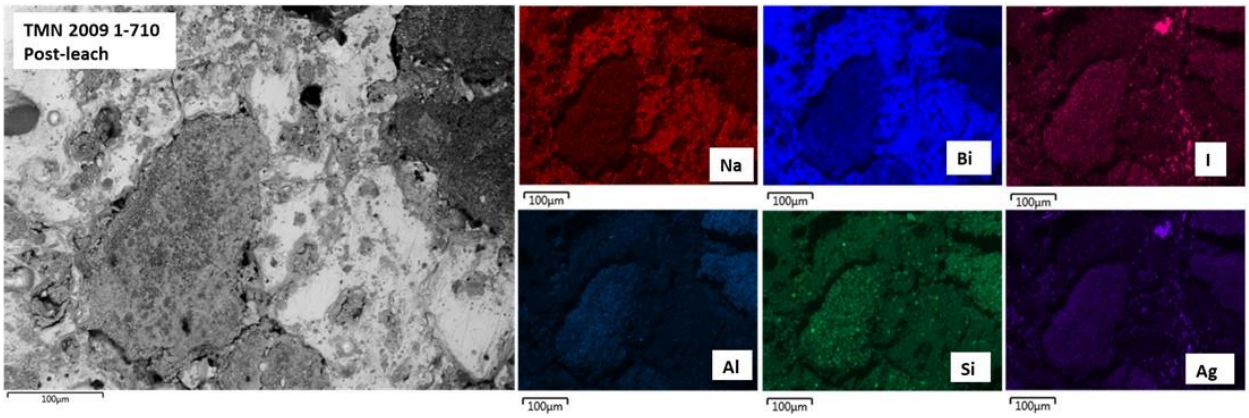

Figure A.18. Post-leach SEM micrograph and the corresponding EDS maps of Ag-mordenite and GCM sample TMN 2009 1-71D.

A-3. Compositions from EDS

The following tables provide the compositions of the samples measured with EDS from multiple maps.

Table A-1. Composition of the glass bonded sodalite samples measured by EDS.

Sample Type	**Glass Bonded Sodalite**	
Sample Name	**NaI Form**	**AgI Form**
Element	**%wt**	**%wt**
O	38.00	37.09
Na	15.57	13.43
Al	10.75	9.98
Si	18.58	16.27
S	0.04	0.08
K	0.07	0.08
Ca	1.00	0.95
Ti	0.27	0.17
Fe	0.13	0.08
Ag	0.00	6.87
I	15.06	14.60
Tb	0.00	0.00
Zr	0.52	0.39

Table A.2. Composition of the small-form Ag-mordenite samples measured by EDS

Sample Type	**Small-Form Ag-Mordenite**								
Sample Name	**HIP 17-17**	**HIP 17-18**	**HIP 17-2**	**HIP 17-22**	**HIP 17-6**	**HIP 17-8**	**ORNL 1-3**	**ORNL 1-7**	**ORNL 1-8**
Element	**%wt**	**%wt**	**%wt**	**%wt**	**%wt**	**%wt**	**%wt**	**%wt**	**%wt**
O	47.10	49.33	46.99	47.37	45.51	44.87	59.10	54.60	54.60
Na	0.52	0.31	0.32	0.36	0.39	0.32	0.00	0.00	-
Mg	0.82	0.40	0.71	0.65	0.72	0.72	0.00	0.00	-
Al	5.91	4.17	6.02	5.66	5.73	5.83	3.40	0.30	0.32
Si	31.70	32.89	31.25	30.15	30.19	31.38	13.60	12.50	12.50
S	0.00	0.00	0.00	0.00	0.00	0.00	0.00	0.00	-
K	1.02	0.65	1.08	1.00	1.06	0.90	0.00	0.00	-
Ca	1.18	1.01	1.27	1.24	1.17	1.37	1.80	1.60	1.60
Mn	0.08	0.05	0.08	0.10	0.06	0.07	0.00	0.00	-
Fe	0.67	0.48	0.66	0.74	0.61	0.68	0.00	0.00	-
Ag	6.03	6.06	7.93	9.51	7.74	7.77	9.00	9.00	9.00
I	4.98	4.63	6.30	3.12	5.04	6.09	0.00	7.00	7.00

Table A.3. Composition of the large-form Ag-mordenite samples measured by EDS

Sample Type	**Ag-mordenite Large Form**							
Sample Name	**HIP18 1-1**	**HIP18 1-2**	**HIP18 2-1**	**HIP18 2-2**	**HIP18 3-1**	**HIP18 3-2**	**HIP18 4-1**	**HIP18 4-2**
Element	**%wt**	**%wt**	**%wt**	**%wt**	**%wt**	**%wt**	**%wt**	**%wt**
C	0.00	0.00	0.00	0.00	0.00	0.00	0.00	0.00
O	42.22	40.29	43.23	43.02	45.83	45.80	46.30	46.58
Na	0.09	0.13	0.09	0.09	0.08	0.10	0.19	0.17
Mg	0.44	0.40	0.44	0.43	0.48	0.48	0.54	0.52
Al	5.34	5.03	5.25	5.38	5.38	5.45	5.70	5.79
Si	31.23	29.63	30.01	30.27	31.58	31.39	31.63	32.10
S	0.00	0.00	0.00	0.00	0.00	0.00	0.00	0.00
K	0.37	0.35	0.36	0.37	0.50	0.50	0.51	0.55
Ca	0.58	0.50	0.56	0.59	0.70	0.67	0.78	0.73
Ti	0.11	0.13	0.11	0.12	0.10	0.10	0.09	0.09
Cr	0.00	0.02	0.00	0.02	0.02	0.04	0.00	0.00
Mn	0.05	0.06	0.06	0.06	0.06	0.05	0.06	0.06
Fe	1.38	3.18	1.01	1.21	1.20	1.52	1.01	0.83
Ni	0.20	0.49	0.21	0.16	0.00	0.10	0.00	0.08
Nb	0.00	0.00	0.00	0.00	0.00	0.00	0.00	0.00
Ag	4.49	6.31	5.16	4.79	7.66	7.39	6.79	6.11
I	13.50	13.50	13.50	13.50	6.40	6.40	6.40	6.40

Table A.4. Composition of the Ag-functionalized silica-based aerogels from EDS.

Sample Type	**Ag-functionalized Silica-based Aerogel**					
Sample Name	**SFA HIP-1**	**SFA HIP-2**	**SFA HIP-3**	**SFA SPS-1**	**SFA SPS-2**	**SFA SPS-3**
Element	**%wt**	**%wt**	**%wt**	**%wt**	**%wt**	**%wt**
C	0.00	0.00	0.00	0.00	0.00	0.00
O	26.63	26.63	0.00	30.14	30.27	33.48
Na	0.00	0.00	0.00	0.00	0.00	0.00
Mg	0.00	0.00	0.00	0.00	0.00	0.00
Al	0.04	0.04	0.06	0.03	0.03	0.02
Si	21.90	21.90	29.84	26.37	26.45	29.64
S	0.00	0.00	0.00	0.93	0.82	0.28
K	0.00	0.00	0.00	0.00	0.00	0.00
Ca	0.00	0.00	0.00	0.00	0.00	0.00
Ti	0.00	0.00	0.00	-	-	-
Cr	0.00	0.00	0.00	0.00	0.00	0.00
Mn	0.00	0.00	0.00	0.00	0.00	0.00
Fe	0.00	0.00	0.00	0.00	0.00	0.00
Ni	0.00	0.00	0.00	-	-	-
Nb	0.00	0.00	0.00	0.00	0.00	0.00
Ag	17.41	17.41	18.29	12.52	12.43	6.56
I	30.00	30.00	15.21	30.00	30.00	30.00

Table A.5. Composition of the iodoapatite ceramic, HIPed sodalites and tellurite glass measured by EDS.

Sample Type	**Iodoapatite Ceramic**	**HIPed Sodalite - U Birmingham**				**Tellurite**
Sample Name	**LSU**	**H1C11**	**H1C5**	**H1C8**	**H1C9**	**Te glass**
Element	**%wt**	**%wt**	**%wt**	**%wt**	**%wt**	**%wt**
C	0.00	-	-	-	-	-
O	8.62	29.28	29.24	27.53	30.12	8.66
Na	0.00	0.20	0.13	0.84	0.77	0.07
Mg	0.00	0.05	0.66	0.02	0.03	-
Al	0.08	10.37	8.20	11.46	12.61	0.55
Si	0.14	16.15	15.58	13.52	13.63	0.06
S	0.00	0.03	0.01	0.02	0.01	-
K	0.00	-	-	-	-	-
Ca	0.00	-	0.13	-	-	-
Ti	0.00	-	-	-	-	-
Cr	0.00	-	-	-	-	-
Mn	0.00	-	-	-	-	-
Fe	0.00	0.01	0.44	0.02	-	-
Ag	0.00	6.40	21.86	17.26	19.43	35.80
I	6.63	5.23	7.12	8.67	3.19	11.66
Tb	0.00	-	-	-	-	-
Zr	0.00	-	-	-	-	-
P	0.00	-	0.07	-	-	-
Cu	0.00	32.27	16.55	20.67	20.22	-
Mo	0.00	-	-	-	-	0.43
Te	0.00	-	-	-	-	32.74
Bi	0.00	-	-	-	-	10.03
V	10.57	-	-	-	-	-
Pb	73.96	-	-	-	-	-

Table A.6. Composition of the Sintered iodosodalite from WSU measured with EDS

Sample Type	Sintered Iodosodalite					
Sample Name	**WSU10**	**WSU22**	**WSU3**	**WSU40**	**WSU52**	**WSU8**
Element	**%wt**	**%wt**	**%wt**	**%wt**	**%wt**	**%wt**
C	-	-	-	-	-	-
O	35.30	35.58	33.85	35.30	35.58	35.30
Na	16.09	17.03	16.22	16.09	17.03	16.09
Mg	-	-	-	-	-	-
Al	13.17	12.85	14.28	13.17	12.85	13.17
Si	14.70	13.93	13.27	14.70	13.93	14.70
Ca	0.29	-	-	0.29	-	0.29
I	20.15	20.15	22.39	20.15	20.15	20.15
Zr	0.15	-	-	0.15	-	0.15
B	0.17	0.45	-	0.17	0.45	0.17

Table A.7. Composition of the Ag mordenite in GCM and Tin Pellet measured by EDS.

Sample Type	Ag Mordenite in GCM			Tin Pellet
Sample Name	**DS-60**	**TJG2010B-55B**	**TMN2019-1-710**	**Tin Pellet**
Element	**%wt**	**%wt**	**%wt**	**%wt**
O	4.15	16.97	17.87	10.33
Na	-	5.92	-	0.14
Al	1.54	12.30	5.06	3.26
Si	6.07	-	11.77	5.48
K	-	-	-	-
Ca	-	0.21	-	-
Zr	-	-	-	-
Zn	7.97	4.41	4.36	-
Rh	2.12	-	-	-
Ag	7.96	8.23	7.98	4.38
Sn	0.00	0	0	72.08
I	8.86	4.25	5.22	4.33
Re	0.15	-	-	-
Bi	61.18	47.35	47.44	-
S	-	0.36	0.30	-

Appendix B

Aqueous Analysis- Raw data

B-1. Raw data

Sample	Surface Area (cm^2)	Solution (mL)	I (µg/L)	Al (µg/L)	Si (µg/L)	Ag (µg/L)
ANS-ORNL17-17-90C-0d	0.89	9.03	ND	ND	ND	ND
ANS-ORNL17-17-90C-1d	0.89	9.04	7210	27.8	4030	24.4
ANS-ORNL17-17-90C-2d	0.89	9.03	76100	ND	2040	ND
ANS-ORNL17-17-90C-3d	0.89	9.04	3840	ND	3180	ND
ANS-ORNL17-17-90C-7d	0.89	9.85	4770	ND	6820	ND
ANS-ORNL17-17-90C-11d	0.89	9.04	2920	ND	2410	ND
ANS-ORNL17-17-90C-15d	0.89	9.04	716	ND	2140	ND
ANS-ORNL17-17-90C-21d	0.89	9.15	158	ND	2860	19.1
ANS-ORNL17-22-90C-0d	1.08	10.97	ND	ND	ND	ND
ANS-ORNL17-22-90C-1d	1.08	10.97	385	ND	1760	ND
ANS-ORNL17-22-90C-2d	1.08	10.98	84.0	ND	1240	19.3
ANS-ORNL17-22-90C-3d	1.08	10.98	23.7	ND	606	79.5
ANS-ORNL17-22-90C-7d	1.08	13.60	17.2	ND	3050	61.1
ANS-ORNL17-22-90C-11d	1.08	10.97	9.11	19.9	2750	53.4
ANS-ORNL17-22-90C-15d	1.08	10.98	16.3	ND	3180	60.3
ANS-ORNL17-22-90C-21d	1.08	11.35	14.3	20.3	4580	121
ANS-SON68-90C-0d	1.00	10.00	ND	ND	ND	ND
ANS-SON68-90C-1d	1.00	10.00	338	ND	691	44.3
ANS-SON68-90C-2d	1.00	9.98	24.8	ND	458	ND
ANS-SON68-90C-3d	1.00	10.00	3.78	ND	233	ND
ANS-SON68-90C-7d	1.00	9.99	ND	ND	1720	26.0
ANS-SON68-90C-11d	1.00	9.99	ND	ND	1640	28.4
ANS-SON68-90C-15d	1.00	10.00	ND	ND	1840	ND
ANS-SON68-90C-21d	1.00	9.99	ND	ND	3240	41.6
ANS-Aero.HIP 1-90C-0d	4.77	47.73	ND	ND	ND	ND
ANS-Aero.HIP 1-90C-1d	4.77	47.73	2030	ND	409	ND
ANS-Aero.HIP 1-90C-2d	4.77	47.73	1510	ND	249	ND
ANS-Aero.HIP 1-90C-3d	4.77	47.73	1600	ND	234	91.6
ANS-Aero.HIP 1-90C-4d	4.77	47.73	1680	ND	196	33.2
ANS-Aero.HIP 1-90C-7d	4.77	47.73	3170	ND	740	21.6
ANS-Aero.HIP 1-90C-15d	4.77	47.73	3220	ND	805	73.0
ANS-Aero.HIP 1-90C-21d	4.77	47.73	673	ND	1030	151
ANS-Aero.HIP 2-90C-0d	2.71	27.08	14.4	ND	ND	ND
ANS-Aero.HIP 2-90C-1d	2.71	27.08	2080	ND	1920	ND
ANS-Aero.HIP 2-90C-2d	2.71	27.08	1880	ND	1410	ND
ANS-Aero.HIP 2-90C-3d	2.71	27.08	1870	ND	1180	19.5
ANS-Aero.HIP 2-90C-4d	2.71	27.08	2060	ND	1070	30.2
ANS-Aero.HIP 2-90C-7d	2.71	27.08	1870	ND	3760	32.5
ANS-Aero.HIP 2-90C-15d	2.71	27.08	1430	ND	5740	62.1
ANS-Aero.HIP 2-90C-21d	2.71	27.08	1080	ND	7610	91.5
ANS-Aero.SPS-1 New No Si-90C-0d	2.51	25.12	ND	ND	ND	ND
ANS-Aero.SPS-1 New No Si-90C-1d	2.51	25.12	1340	ND	1130	ND

Sample	Surface Area (cm^2)	Solution (mL)	I (µg/L)	Al (µg/L)	Si (µg/L)	Ag (µg/L)
ANS-Aero.SPS-1 New No Si-90C-2d	2.51	25.12	406	ND	533	30.2
ANS-Aero.SPS-1 New No Si-90C-3d	2.51	25.12	122	ND	465	ND
ANS-Aero.SPS-1 New No Si-90C-4d	2.51	25.12	44.5	ND	338	19.9
ANS-Aero.SPS-1 New No Si-90C-7d	2.51	25.12	59.9	ND	997	ND
ANS-Aero.SPS-1 New No Si-90C-15d	2.51	25.12	26.2	ND	3510	54.2
ANS-Aero.SPS-1 New No Si-90C-21d	2.51	25.12	25.9	ND	7060	41.5
ANS-Aero.SPS-2 New-90C-0d	1.73	17.27	1.39	ND	ND	ND
ANS-Aero.SPS-2 New-90C-1d	1.73	17.27	2050	ND	263	23.5
ANS-Aero.SPS-2 New-90C-2d	1.73	17.27	265	ND	204	33.6
ANS-Aero.SPS-2 New-90C-3d	1.73	17.27	145	ND	176	ND
ANS-Aero.SPS-2 New-90C-4d	1.73	17.27	60.5	ND	162	ND
ANS-Aero.SPS-2 New-90C-7d	1.73	17.27	87.0	ND	1090	26.3
ANS-Aero.SPS-2 New-90C-15d	1.73	17.27	34.0	ND	7670	51.8
ANS-Aero.SPS-2 New-90C-21d	1.73	17.27	17.9	ND	13300	51.6
ANS-ORNL1-8-90C-1d	0.83	8.32	36.1	16.7	1540	77.7
ANS-ORNL1-8-90C-2d	0.83	8.32	1.55	ND	1230	54.1
ANS-ORNL1-8-90C-3d	0.83	8.32	0.396	ND	822	224
ANS-ORNL1-8-90C-7d	0.83	8.32	0.886	23.1	3190	80.5
ANS-ORNL1-7-90C-1d	0.87	8.71	1.21	30.2	1850	169
ANS-ORNL1-7-90C-2d	0.87	8.71	ND	ND	1200	367
ANS-ORNL1-7-90C-3d	0.87	8.71	ND	ND	965	24.1
ANS-ORNL1-7-90C-7d	0.87	8.71	ND	ND	3650	121
ANS-ORNL1-3-90C-1d	0.92	9.23	30.5	20.8	1510	43.1
ANS-ORNL1-3-90C-2d	0.92	9.23	2.79	ND	609	21.6
ANS-ORNL1-3-90C-3d	0.92	9.23	2.73	ND	440	19.3
ANS-ORNL1-3-90C-7d	0.92	9.23	1.82	ND	2230	23.5
ANS-ORNL17-2-90C No Si-3d	0.96	9.55	17.6	39.8	3710	63.7
ANS-ORNL17-2-90C No Si-4d	0.96	9.55	2.67	19.0	992	25.9
ANS-ORNL17-2-90C No Si-7d	0.96	9.55	3.79	18.9	2970	29.4
ANS-ORNL17-2-90C No Si-15d	0.96	9.55	2.81	ND	3620	20.1
ANS-ORNL17-2-90C No Si-21d	0.96	9.55	4.57	ND	4530	39.4
HIP18 1-1-600g-0d	5.20	515.42	ND	ND	ND	ND
HIP18 1-1-600g-1d	5.20	519.59	20600	ND	282	ND
HIP18 1-1-600g-3d	5.20	519.53	1570	ND	174	ND
HIP18 1-1-600g-7d	5.20	519.50	173	ND	145	ND
HIP18 1-1-600g-11d	5.20	519.48	265	ND	351	ND
HIP18 1-1-600g-15d	5.20	519.40	257	ND	571	ND
HIP18 1-1-600g-21d	5.20	518.82	400	ND	715	ND
HIP18 1-2-1200g-0d	4.79	478.60	ND	63.4	ND	ND
HIP18 1-2-1200g-1d	4.79	478.65	27400	ND	286	ND
HIP18 1-2-1200g-3d	4.79	478.55	2190	211	186	ND
HIP18 1-2-1200g-7d	4.79	478.54	572	ND	155	ND
HIP18 1-2-1200g-15d	4.79	478.69	815	16.6	607	ND
HIP18 1-2-1200g-21d	4.79	478.61	1100	ND	835	ND
HIP18 2-1-2400g-0d	4.45	444.81	ND	115	ND	ND
HIP18 2-1-2400g-1d	4.45	444.81	24100	32.7	197	ND
HIP18 2-1-2400g-3d	4.45	444.80	2120	ND	144	ND
HIP18 2-1-2400g-7d	4.45	444.80	182	ND	117	ND
HIP18 2-1-2400g-11d	4.45	444.81	222	ND	340	ND

Sample	Surface Area (cm^2)	Solution (mL)	I (µg/L)	Al (µg/L)	Si (µg/L)	Ag (µg/L)
HIP18 2-1-2400g-15d	4.45	444.89	183	66.0	530	ND
HIP18 2-1-2400g-21d	4.45	444.89	332	ND	738	ND
HIP18 2-2-AlColl-0d	4.54	453.52	ND	ND	ND	ND
HIP18 2-2-AlColl-1d	4.54	453.31	20000	20.3	294	ND
HIP18 2-2-AlColl-3d	4.54	453.50	1100	ND	164	ND
HIP18 2-2-AlColl-7d	4.54	453.50	139	ND	145	ND
HIP18 2-2-AlColl-11d	4.54	453.55	221	23.8	429	ND
HIP18 2-2-AlColl-15d	4.54	453.51	172	ND	611	ND
HIP18 2-2-AlColl-21d	4.54	453.51	388	ND	823	ND
HIP18 3-1-600g-0d	4.74	473.96	ND	34.3	ND	ND
HIP18 3-1-600g-1d	4.74	473.91	1710	53.7	133	ND
HIP18 3-1-600g-3d	4.74	474.00	569	228	86.5	ND
HIP18 3-1-600g-7d	4.74	474.00	465	ND	67.8	ND
HIP18 3-1-600g-11d	4.74	473.93	974	ND	173	ND
HIP18 3-1-600g-15d	4.74	473.93	961	ND	258	ND
HIP18 3-1-600g-21d	4.74	473.93	1460	ND	343	ND
HIP18 3-2-1200g-0d	4.82	481.68	ND	ND	ND	ND
HIP18 3-2-1200g-1d	4.82	481.68	2250	ND	159	ND
HIP18 3-2-1200g-3d	4.82	481.75	562	ND	97.9	ND
HIP18 3-2-1200g-7d	4.82	481.59	554	ND	79.6	ND
HIP18 3-2-1200g-11d	4.82	481.60	981	52.8	195	ND
HIP18 3-2-1200g-15d	4.82	481.49	1040	ND	246	ND
HIP18 3-2-1200g-21d	4.82	481.63	1360	ND	343	ND
HIP18 4-1-2400g-0d	3.93	392.94	ND	20.4	ND	ND
HIP18 4-1-2400g-1d	3.93	392.91	281	20.1	155	ND
HIP18 4-1-2400g-3d	3.93	393.00	243	ND	143	ND
HIP18 4-1-2400g-7d	3.93	392.92	162	ND	98.5	ND
HIP18 4-1-2400g-11d	3.93	391.53	311	ND	303	ND
HIP18 4-1-2400g-15d	3.93	392.96	285	ND	432	ND
HIP18 4-1-2400g-21d	3.93	392.71	393	ND	564	ND
HIP18 4-2-AlColl-0d	4.07	407.33	ND	ND	ND	ND
HIP18 4-2-AlColl-1d	4.07	407.30	1360	ND	167	ND
HIP18 4-2-AlColl-3d	4.07	407.10	187	87.9	124	ND
HIP18 4-2-AlColl-7d	4.07	407.42	107	ND	97.0	ND
HIP18 4-2-AlColl-11d	4.07	407.33	164	ND	250	ND
HIP18 4-2-AlColl-15d	4.07	408.00	433	ND	386	ND
HIP18 4-2-AlColl-21d	4.07	407.41	320	ND	517	ND
HIP18 1-1 NoRef-1d	5.20	519.53	110	ND	184	ND
HIP18 1-1 NoRef-2d	5.20	519.53	198	ND	533	ND
HIP18 1-1 NoRef-3d	5.20	519.53	247	ND	806	ND
HIP18 1-1 NoRef-7d	5.20	519.53	381	ND	1750	ND
HIP18 1-1 NoRef-11d	5.20	519.53	478	ND	2400	ND
HIP18 1-1 NoRef-15d	5.20	519.53	657	ND	3880	ND
HIP18 1-1 NoRef-21d	5.20	519.53	774	ND	4890	ND
HIP18 1-2 NoRef-1d	4.79	478.57	105	ND	177	ND
HIP18 1-2 NoRef-2d	4.79	478.57	152	ND	451	ND
HIP18 1-2 NoRef-3d	4.79	478.57	216	ND	711	ND
HIP18 1-2 NoRef-7d	4.79	478.57	363	ND	1670	ND
HIP18 1-2 NoRef-11d	4.79	478.57	469	ND	2330	ND
HIP18 1-2 NoRef-15d	4.79	478.57	650	ND	3760	ND

Sample	Surface Area (cm^2)	Solution (mL)	I (µg/L)	Al (µg/L)	Si (µg/L)	Ag (µg/L)
HIP18 1-2 NoRef-21d	4.79	478.57	802	ND	4950	ND
HIP18 3-1 NoRef-1d	4.74	473.91	27.8	ND	ND	ND
HIP18 3-1 NoRef-2d	4.74	473.91	78.3	ND	ND	ND
HIP18 3-1 NoRef-3d	4.74	473.91	121	ND	211	ND
HIP18 3-1 NoRef-7d	4.74	473.91	245	ND	483	ND
HIP18 3-1 NoRef-11d	4.74	473.91	303	ND	655	ND
HIP18 3-1 NoRef-15d	4.74	473.91	324	ND	1000	ND
HIP18 3-1 NoRef-21d	4.74	473.91	305	ND	1360	ND
HIP18 3-2 NoRef-1d	4.82	481.68	9	ND	ND	ND
HIP18 3-2 NoRef-2d	4.82	481.68	34.5	ND	173	ND
HIP18 3-2 NoRef-3d	4.82	481.68	54.4	ND	248	ND
HIP18 3-2 NoRef-7d	4.82	481.68	104	ND	585	ND
HIP18 3-2 NoRef-11d	4.82	481.68	130	ND	813	ND
HIP18 3-2 NoRef-15d	4.82	481.68	175	ND	1250	ND
HIP18 3-2 NoRef-21d	4.82	481.68	186	ND	1660	ND
C1220-HIP17-17-3d	0.96	9.00	21.3	ND	1710	134
C1220-HIP17-17-6d	0.96	9.00	21.6	21.5	3360	109
C1220-HIP17-17-9d	0.96	9.00	20.5	40.8	5720	158
C1220-HIP17-17-13d	0.96	9.00	14.4	16.6	4420	84.2
C1220-HIP17-17-16d	0.96	9.00	3.83	ND	2930	60.6
C1220-HIP17-22-3d	1.23	10.88	74.4	ND	1070	ND
C1220-HIP17-22-6d	1.23	10.88	78.7	18.0	2040	ND
C1220-HIP17-22-9d	1.23	10.88	6.99	ND	2160	67.1
C1220-HIP17-22-13d	1.23	10.88	15.7	ND	2240	84.9
C1220-HIP17-22-16d	1.23	10.88	20.0	ND	1420	105
C1220-HIP17-8-3d	0.98	9.80	33.0	17.7	616	75.8
C1220-HIP17-8-6d	0.98	9.80	11.9	ND	1150	ND
C1220-HIP17-8-9d	0.98	9.80	2.93	ND	1250	ND
C1220-HIP17-8-13d	0.98	9.80	48.6	21.4	1710	ND
C1220-HIP17-8-16d	0.98	9.80	2020	ND	1340	ND
C1220-Sodalite-H1C6-3d	2.01	18.62	3.07	2480	298	192
C1220-Sodalite-H1C6-6d	2.01	18.62	2.97	554	488	194
C1220-Sodalite-H1C6-9d	2.01	18.62	4.61	43.5	528	315
C1220-Sodalite-H1C6-13d	2.01	18.62	4.05	ND	587	287
C1220-Sodalite-H1C6-16d	2.01	18.62	3.56	ND	548	224
C1220-SON68-3d	1.50	15.20	ND	17.4	2720	ND
C1220-SON68-6d	1.50	15.04	ND	728	6820	ND
C1220-SON68-9d	1.50	15.04	ND	145	7240	ND
C1220-SON68-13d	1.50	15.09	3.72	652	8990	ND
C1220-SON68-16d	1.50	15.08	ND	125	6700	ND
C1220-HIP 18 2-1-3d	4.45	444.81	217	ND	706	ND
C1220-HIP 18 2-1-6d	4.45	444.81	108	ND	635	ND
C1220-HIP 18 2-1-9d	4.45	444.81	98.4	ND	545	ND
C1220-HIP 18 2-1-13d	4.45	444.81	127	ND	753	ND
C1220-HIP 18 2-1-16d	4.45	444.81	109	ND	583	ND
C1220-HIP 18 2-1-21d	4.45	444.81	156	ND	740	ND
C1220-HIP 18 2-2-3d	5.33	453.51	192	ND	514	ND
C1220-HIP 18 2-2-6d	5.33	453.51	127	ND	587	ND

Sample	Surface Area (cm^2)	Solution (mL)	I (µg/L)	Al (µg/L)	Si (µg/L)	Ag (µg/L)
C1220-HIP 18 2-2-13d	5.33	453.51	153	ND	700	ND
C1220-HIP 18 2-2-16d	5.33	453.51	109	ND	493	ND
C1220-HIP 18 2-2-21d	5.33	453.51	184	ND	693	ND
C1220-HIP 18 4-1-3d	3.93	392.95	36.1	ND	246	ND
C1220-HIP 18 4-1-6d	3.93	392.95	56.8	ND	209	ND
C1220-HIP 18 4-1-9d	3.93	392.95	40.5	ND	225	ND
C1220-HIP 18 4-1-13d	3.93	392.95	30.0	ND	347	ND
C1220-HIP 18 4-1-16d	3.93	392.95	23.4	ND	243	ND
C1220-HIP 18 4-1-21d	3.93	392.95	42.6	ND	360	ND
C1220-HIP 18 4-2-3d	4.70	407.32	14.5	ND	254	ND
C1220-HIP 18 4-2-6d	4.70	407.32	14.2	ND	248	ND
C1220-HIP 18 4-2-9d	4.70	407.32	17.4	ND	203	ND
C1220-HIP 18 4-2-13d	4.70	407.32	29.4	ND	332	ND
C1220-HIP 18 4-2-16d	4.70	407.32	28.6	58.8	247	ND
C1220-HIP 18 4-2-21d	4.70	407.32	40.7	ND	320	ND
C1220-Aero HIP 2-3d	4.00	27.08	1890	147	2870	ND
C1220-Aero HIP 2-6d	4.00	27.08	1490	ND	1020	ND
C1220-Aero HIP 2-9d	4.00	27.08	930	53.7	1120	65.0
C1220-Aero HIP 2-13d	4.00	27.08	1010	ND	1160	65.0
C1220-Aero HIP 2-16d	4.00	27.08	925	ND	2500	58.1
C1220-Aero HIP 2-21d	4.00	27.08	727	ND	1380	83.9
C1220-SPS-1-3d	2.51	25.12	6.09	171	1050	390
C1220-SPS-1-6d	2.51	25.12	4.21	59.8	1180	458
C1220-SPS-1-9d	2.51	25.12	14.0	ND	3450	349
C1220-SPS-1-13d	2.51	25.12	18.1	ND	2970	299
C1220-SPS-1-16d	2.51	25.12	18.0	ND	2890	241
C1220-SPS-1-21d	2.51	25.12	17.0	ND	5670	319
C1220-SPS-2-3d	2.04	17.27	6.46	ND	788	336
C1220-SPS-2-6d	2.04	17.27	2.82	163	577	427
C1220-SPS-2-9d	2.04	17.27	14.8	175	1120	253
C1220-SPS-2-13d	2.04	17.27	22.1	ND	819	197
C1220-SPS-2-16d	2.04	17.27	24.7	ND	819	177
C1220-SPS-2-21d	2.04	17.27	20.0	ND	2370	249
C1220-LSU-3d	0.05	4.50	633	71.6	ND	ND
C1220-LSU-6d	0.05	4.50	842	ND	ND	ND
C1220-LSU-9d	0.05	4.50	0	0	0	0
C1220-LSU-13d	0.05	4.50	401	ND	ND	ND
C1220-LSU-16d	0.05	4.50	40.3	ND	ND	ND
C1220-LSU-21d	0.05	4.50	60.3	ND	ND	ND
C1220-WSU10.4-3d	0.01	9.00	13000	17100	33100	ND
C1220-WSU10.4-6d	0.01	9.00	15400	17700	26500	ND
C1220-WSU10.4-9d	0.01	9.00	15600	18100	26400	ND
C1220-WSU10.4-13d	0.01	9.00	17800	21000	29500	ND
C1220-WSU10.4-16d	0.01	9.00	15800	15200	21800	ND
C1220-WSU22.1-3d	0.05	8.83	365	4030	81800	ND
C1220-WSU22.1-6d	0.05	8.83	14700	11800	24200	ND
C1220-WSU22.1-9d	0.05	8.83	17200	10500	16400	ND
C1220-WSU40.1-3d	0.03	9.00	50900	11600	621000	ND

Sample	Surface Area (cm^2)	Solution (mL)	I (µg/L)	Al (µg/L)	Si (µg/L)	Ag (µg/L)
C1220-WSU40.1-6d	0.03	9.00	1970	21800	118000	ND
C1220-WSU40.1-13d	0.03	9.00	13800	16800	142000	ND
C1220-WSU40.2-3d	0.03	9.00	18700	14700	251000	ND
C1220-WSU40.2-6d	0.03	9.00	2800	24000	117000	ND
C1220-WSU40.2-9d	0.03	9.00	6560	17800	66500	ND
C1220-WSU40.2-13d	0.03	9.00		16300	68000	ND
C1220-WSU52-3d	0.01	9.00	1530	6830	551000	ND
C1220-WSU52-6d	0.01	9.00	437	17700	82600	ND
C1220-WSU52.1-3d	0.02	9.00	1620	8420	593000	ND
C1220-WSU52.1-6d	0.02	9.00	288	22100	92500	ND
C1220-WSU52.1-13d	0.02	9.00	15700	15700	79400	ND
C1220-AgIBR-3d	0.08	18.86	126000	26600	43100	342
C1220-AgIBR-6d	0.08	18.86	145000	16600	22200	123
C1220-AgIBR-9d	0.08	18.86	117000	13800	19200	49.4
C1220-NaIBR-3d	0.15	23.31	9260	10900	33100	ND
C1220-NaIBR-6d	0.15	23.31	9360	10300	25500	ND
C1220-NaIBR-9d	0.15	23.31	9350	8030	20600	ND
C1220-NaIBR-13d	0.15	23.31	10600	22100	26100	ND
C1220-Sodalite H1C5-3d	2.36	10.00	6.55	ND	1950	92.2
C1220-Sodalite H1C5-6d	2.36	10.00	4.50	ND	1290	221
C1220-Sodalite H1C5-9d	2.36	10.00	7.68	ND	1210	133
C1220-Sodalite H1C5-13d	2.36	10.00	5.65	ND	1150	272
C1220-Sodalite H1C8-3d	1.78	10.00	197	51.5	2150	ND
C1220-Sodalite H1C8-6d	1.78	10.00	17.4	ND	1450	34.7
C1220-Sodalite H1C8-9d	1.78	10.00	45.8	78.8	1460	ND
C1220-Sodalite H1C9-3d	2.28	10.00	801	811	8460	241
C1220-Sodalite H1C9-6d	2.28	10.00	28.9	73.1	1920	259
C1220-Sodalite H1C9-9d	2.28	10.00	10.8	58.5	1950	167
C1220-Sodalite H1C9-16d	2.28	10.00	17.2	51.0	1350	154
C1220-Sodalite H1C11-3d	2.19	10.00	2.96	ND	2530	263
C1220-Sodalite H1C11-6d	2.19	10.00	2.98	ND	1160	337
C1220-Sodalite H1C11-9d	2.19	10.00	9.29	ND	1090	186
C1220-Sodalite H1C11-13d	2.19	10.00	10.4	ND	879	338
C1220-Sodalite H1C5-DUP-0d	2.36	7.52	8.72	ND	ND	ND
C1220-Sodalite H1C5-DUP-3d	2.36	7.52	1.35	ND	1140	ND
C1220-Sodalite H1C5-DUP-6d	2.36	7.52	3.35	ND	1320	229
C1220-Sodalite H1C5-DUP-9d	2.36	7.59	7.20	ND	1250	185
C1220-Sodalite H1C5-DUP-13d	2.36	7.52	2.89	ND	946	297
C1220-Sodalite H1C5-DUP-16d	2.36	7.54	3.34	ND	2200	211
C1220-Sodalite H1C5-DUP-21d	2.36	7.54	2.79	45.6	2270	103
C1220-Sodalite H1C6-DUP-0d	2.01	7.00	1.32	ND	ND	ND
C1220-Sodalite H1C6-DUP-3d	2.01	7.01	0.544	ND	827	30.3
C1220-Sodalite H1C6-DUP-6d	2.01	7.00	1.85	ND	1120	344
C1220-Sodalite H1C6-DUP-9d	2.01	7.03	2.44	ND	1030	347
C1220-Sodalite H1C6-DUP-13d	2.01	7.01	1.89	ND	1530	410
C1220-Sodalite H1C6-DUP-16d	2.01	7.00	4.06	ND	1280	292

Sample	Surface Area (cm^2)	Solution (mL)	I (µg/L)	Al (µg/L)	Si (µg/L)	Ag (µg/L)
C1220-Sodalite H1C6-DUP-21d	2.01	7.01	4.28	55.0	2480	310
C1220-Sodalite H1C8-DUP-0d	1.78	7.50	0.0860	ND	ND	ND
C1220-Sodalite H1C8-DUP-3d	1.78	7.50	6.33	ND	1330	ND
C1220-Sodalite H1C8-DUP-6d	1.78	7.49	43.0	ND	1850	ND
C1220-Sodalite H1C8-DUP-9d	1.78	7.50	39.3	47.7	1830	ND
C1220-Sodalite H1C8-DUP-13d	1.78	7.49	20.0	47.3	2410	ND
C1220-Sodalite H1C8-DUP-16d	1.78	7.50	34.7	65.6	1950	ND
C1220-Sodalite H1C8-DUP-21d	1.78	7.50	30.7	130	3730	ND
C1220-Sodalite H1C9-DUP-0d	2.28	8.00	ND	ND	ND	28.8
C1220-Sodalite H1C9-DUP-3d	2.28	8.01	1.16	ND	1050	ND
C1220-Sodalite H1C9-DUP-6d	2.28	8.01	2.55	50.9	1420	153
C1220-Sodalite H1C9-DUP-9d	2.28	8.01	7.86	55.4	1990	193
C1220-Sodalite H1C9-DUP-13d	2.28	8.07	7.00	48.0	2290	113
C1220-Sodalite H1C9-DUP-16d	2.28	8.05	5.91	93.8	2330	140
C1220-Sodalite H1C9-DUP-21d	2.28	8.03	5.24	103	3460	51.9
C1220-Sodalite H1C11-DUP-0d	2.19	7.50	0.733	ND	ND	ND
C1220-Sodalite H1C11-DUP-3d	2.19	7.49	0.868	ND	661	27.8
C1220-Sodalite H1C11-DUP-6d	2.19	7.50	2.89	ND	740	272
C1220-Sodalite H1C11-DUP-9d	2.19	7.50	3.76	ND	701	260
C1220-Sodalite H1C11-DUP-13d	2.19	7.50	2.83	ND	ND	ND
C1220-Sodalite H1C11-DUP-16d	2.19	7.49	1.83	52.6	775	236
C1220-Sodalite H1C11-DUP-21d	2.19	7.50	2.99	ND	1390	230

Sample	Surface Area (cm^2)	Solution (mL)	I (µg/L)	Al (µg/L)	Si (µg/L)	Ag (µg/L)
C1220-AgIBR-DUP-0d	0.08	12.70	129	332	432	ND
C1220-AgIBR-DUP-3d	0.08	12.71	93700	13200	18500	42.8
C1220-AgIBR-DUP-6d	0.08	12.73	105000	15700	22300	87.7
C1220-AgIBR-DUP-9d	0.08	12.70	104000	16000	23100	133
C1220-AgIBR-DUP-13d	0.08	12.70	110000	17700	26000	183
C1220-AgIBR-DUP-16d	0.08	12.73	92200	15600	22900	79.6
C1220-AgIBR-DUP-21d	0.08	12.71	112000	17500	25900	112
C1220-NaIBR-DUP-0d	0.15	12.70	132	120	134	ND
C1220-NaIBR-DUP-3d	0.15	12.70	5730	7700	22300	ND
C1220-NaIBR-DUP-6d	0.15	12.70	7310	8380	22400	ND
C1220-NaIBR-DUP-9d	0.15	12.72	11000	9730	21600	ND
C1220-NaIBR-DUP-13d	0.15	12.77	10500	9270	22300	ND
C1220-NaIBR-DUP-16d	0.15	12.73	10300	9030	20900	ND
C1220-NaIBR-DUP-21d	0.15	12.72	9300	9560	22500	ND
C1220-WSU22.1-DUP-0d	0.05	5.00	479	179	601	ND
C1220-WSU22.1-DUP-3d	0.05	5.00	17000	10600	16700	ND
C1220-WSU22.1-DUP-6d	0.05	5.03	20700	13000	18900	ND
C1220-WSU22.1-DUP-9d	0.05	5.01	16700	11100	16600	ND
C1220-WSU22.1-DUP-13d	0.05	5.01	19500	13300	19800	ND
C1220-WSU22.1-DUP-16d	0.05	5.00	19100	11900	17700	ND
C1220-WSU22.1-DUP-21d	0.05	5.01	23300	15600	21200	ND

Sample	Surface Area (cm^2)	Solution (mL)	I (µg/L)	Al (µg/L)	Si (µg/L)	Ag (µg/L)
C1220-Aero HIP 2-DUP-0d	4.00	5.00	45.1	ND	ND	ND
C1220-Aero HIP 2-DUP-3d	4.00	5.02	130	116	6570	582
C1220-Aero HIP 2-DUP-6d	4.00	4.99	385	68.3	6680	811
C1220-Aero HIP 2-DUP-9d	4.00	5.02	309	47.1	6460	459
C1220-Aero HIP 2-DUP-13d	4.00	5.07	195	ND	9730	407
C1220-Aero HIP 2-DUP-16d	4.00	5.04	124	ND	8520	458
C1220-Aero HIP 2-DUP-21d	4.00	5.02	231	ND	18000	806
C1220-SPS-1-DUP-0d	2.51	7.00	0	ND	ND	ND
C1220-SPS-1-DUP-3d	2.51	7.00	40.6	0	0	0
C1220-SPS-1-DUP-6d	2.51	7.05	13.7	0	0	0
C1220-SPS-1-DUP-9d	2.51	7.00	0	0	0	0
C1220-SPS-1-DUP-13d	2.51	7.03	0	ND	30700	453
C1220-SPS-1-DUP-16d	2.51	7.05	0	ND	32600	305
C1220-SPS-1-DUP-21d	2.51	7.02	47.6	ND	66000	463
C1220-SPS-2-DUP-0d	2.04	7.00	1.82	ND	ND	ND
C1220-SPS-2-DUP-3d	2.04	6.99	27.3	ND	5150	77.3
C1220-SPS-2-DUP-6d	2.04	7.03	7.32	ND	9190	663
C1220-SPS-2-DUP-9d	2.04	7.03	0	ND	9530	950
C1220-SPS-2-DUP-13d	2.04	7.05	13.7	ND	32000	1170
C1220-SPS-2-DUP-16d	2.04	7.08	20.4	ND	15300	919
C1220-SPS-2-DUP-21d	2.04	7.03	0	ND	34600	1620
C1220-LSU-DUP-0d	0.05	5.00	2.67	ND	ND	ND
C1220-LSU-DUP-3d	0.05	5.00	112	ND	ND	ND
C1220-LSU-DUP-6d	0.05	5.04	61.7	ND	ND	ND
C1220-LSU-DUP-9d	0.05	5.03	52.0	ND	ND	ND
C1220-LSU-DUP-13d	0.05	5.06	49.5	ND	ND	ND
C1220-LSU-DUP-16d	0.05	5.05	36.0	ND	ND	ND
C1220-LSU-DUP-21d	0.05	5.03	68.5	ND	ND	ND
C1220-HIP17-17 DUP-0d	0.96	5.00	1.49	ND	ND	ND
C1220-HIP17-17 DUP-3d	0.96	5.00	3.20	ND	4020	103
C1220-HIP17-17 DUP-6d	0.96	5.01	12.9	69.4	4810	174
C1220-HIP17-17 DUP-9d	0.96	5.01	15.8	76.2	4900	135
C1220-HIP17-17 DUP-13d	0.96	5.01	18.1	93.5	6490	114
C1220-HIP17-17 DUP-16d	0.96	4.97	3.46	82.2	4570	71.8
C1220-HIP17-17 DUP-21d	0.96	5.00	4.27	72.0	7970	80.0
C1220-HIP17-22 DUP-0d	1.23	5.00	ND	ND	ND	ND
C1220-HIP17-22 DUP-3d	1.23	5.02	2.42	ND	3150	ND
C1220-HIP17-22 DUP-6d	1.23	5.06	23.8	49.2	3060	129
C1220-HIP17-22 DUP-9d	1.23	0.00	0	0	0	0
C1220-HIP17-22 DUP-13d	1.23	5.06	12.3	48.6	3720	187
C1220-HIP17-22 DUP-16d	1.23	5.00	6.30	51.1	2850	130
C1220-HIP17-22 DUP-21d	1.23	5.03	134	ND	5820	ND
C1220-SON68-DUP-0d	1.50	5.00	0.779	ND	ND	ND
C1220-SON68-DUP-3d	1.50	5.01	7.97	301	9500	ND

Sample	Surface Area (cm^2)	Solution (mL)	I (µg/L)	Al (µg/L)	Si (µg/L)	Ag (µg/L)
C1220-SON68-DUP-6d	1.50	5.00	1.86	376	10000	ND
C1220-SON68-DUP-9d	1.50	5.00	2.06	438	10300	ND
C1220-SON68-DUP-13d	1.50	5.04	3.47	803	12400	ND
C1220-SON68-DUP-16d	1.50	4.99	48.5	855	10900	ND
C1220-SON68-DUP-21d	1.50	5.01	45.3	996	13500	ND
C1220-Te glass-DUP-0d	2.62	7.00	0.879	ND	ND	66.7
C1220-Te glass-DUP-3d	2.62	6.99	1.40	ND	ND	5620
C1220-Te glass-DUP-6d	2.62	6.99	0.862	ND	ND	7130
C1220-Te glass-DUP-9d	2.62	7.01	0	48.8	ND	7020
C1220-Te glass-DUP-13d	2.62	7.04	5.23	50.7	ND	7620
C1220-Te glass-DUP-16d	2.62	7.02	1.65	ND	ND	5510
C1220-Te glass-DUP-21d	2.62	7.01	2.82	ND	ND	7070
C1220-WSU17 8-DUP-0d	2.32	7.50	1540	57.1	ND	ND
C1220-WSU17 8-DUP-3d	2.32	7.51	17700	6840	12100	ND
C1220-WSU17 8-DUP-6d	2.32	7.59	19500	7870	13900	ND
C1220-WSU17 8-DUP-9d	2.32	7.53	17700	7570	13500	ND
C1220-WSU17 8-DUP-13d	2.32	7.54	19900	8300	15600	ND
C1220-WSU17 8-DUP-16d	2.32	7.55	17800	8050	14600	ND
C1220-WSU17 8-DUP-21d	2.32	7.54	53700	7640	22500	ND
C1220-WSU17 3-DUP-0d	0.75	5.00	5720	55.8	ND	ND
C1220-WSU17 3-DUP-3d	0.75	5.03	67700	4280	15400	ND
C1220-WSU17 3-DUP-6d	0.75	5.00	60800	4760	19100	ND
C1220-WSU17 3-DUP-9d	0.75	5.01	53000	5490	19200	ND
C1220-WSU17 3-DUP-13d	0.75	5.03	49400	5710	19400	ND
C1220-WSU17 3-DUP-16d	0.75	5.01	34300	7210	17300	ND
C1220-WSU17 3-DUP-21d	0.75	5.01	20500	8760	16700	ND

Sample	Surface Area (cm^2)	Solution (mL)	I (µg/L)	Al (µg/L)	Si (µg/L)	Ag (µg/L)
ANS-ORNL 17-8-23C-1d	0.871	8.71	---	ND	72.7	ND
ANS-ORNL 17-17-23C-1d	0.892	8.92	---	ND	277	ND
ANS-ORNL 17-22-23C-1d	1.152	11.52	---	ND	127	ND
ANS-SON68-23C-1d	1.51	15.1	---	ND	ND	ND
ANS-BLK16-Soln-23C-1d	---	---	---	ND	ND	ND
ANS-BLK 18 I-23C-1d	---	---	---	ND	ND	ND
ANS-BLK17 Silicon-23C-1d	---	---	---	ND	571	ND
ANS-ORNL17-6-40C-1d	0.974	9.74	117	ND	708	ND
ANS-ORNL17-8-40C-1d	0.977	9.77	191	ND	540	ND
ANS-ORNL17-17-40C-1d	0.892	8.92	26.8	ND	745	ND
ANS-ORNL17-22-40C-1d	1.019	10.19	32.0	ND	946	ND
ANS-SON68-40C-1d	1.51	15.1	ND	ND	322	ND
ANS-BLK13 Soln-40C-1d	---	---	---	ND	ND	ND
ANS-BLK14 Silicon-40C-1d	---	---	---	ND	1650	ND
ANS-BLK 15 I-40C-1d	---	---	---	ND	ND	ND
ANS-ORNL17-2-70C-1d	0.964	9.64	3.66	ND	1860	28.3
ANS-ORNL17-18-70C-1d	1.347	13.47	5.14	ND	10800	123
ANS-Aero.SPS-3.New-70C-NoSi-1d	---	---	306	ND	333	ND
ANS-Aero.HIP-3-70C-NoSi-1d	---	---	ND	ND	4420	280
ANS-BLK7 Soln-70C-1d	---	---	---	ND	ND	ND
ANS-BLK 9 I-70C-1d	---	---	---	ND	ND	ND
ANS-Aero.SPS-1 New No Si-90C-1d	---	---	1340	ND	1130	ND
ANS-Aero.SPS-2 New-90C-1d	---	---	2050	ND	263	23.5
ANS-ORNL1-3-90C-1d	---	---	30.5	20.8	1510	43.1
ANS-ORNL1-7-90C-1d	---	---	1.21	30.2	1850	169
ANS-ORNL1-8-90C-1d	---	---	36.1	16.7	1540	77.7
ANS-ORNL17-2-90C-1d	0.964	9.64	366	51.1	1800	150
ANS-ORNL17-6-90C-1d	0.974	9.74	20400	ND	1140	ND
ANS-ORNL17-8-90C-1d	0.977	9.77	326	33.3	2540	46.2
ANS-ORNL17-17-90C-1d	0.892	8.92	7210	27.8	4030	24.4
ANS-ORNL17-18-90C-1d	1.347	13.47	131	122	13200	144
ANS-ORNL17-22-90C-1d	1.151	11.51	385	ND	1760	ND
ANS-SON68-90C-1d	1.51	15.1	338	ND	691	44.3